EXPERIMENTAL STUDY ON THE EFFECTS OF DENSITY, MACH NUMBER AND GEOMETRY ON THE LARGE SCALE STRUCTURE IN A TURBULENT JET AND ITS RADIATED NOISE

by

LEE HOCK SENG, B.E. (HONS)

THE UNIVERSITY OF ADELAIDE

DEPARTMENT OF MECHANICAL ENGINEERING

Awarded 8-8-84

THESIS SUMITTED FOR THE DEGREE OF DOCTOR OF PHILOSOPHY

THE UNIVERSITY OF ADELAIDE

DATA SUPPLEMENT

A Supplement to this thesie containing tabulations of all acoustic data is available from the Department of Mechanical Engineering, University of Adelaide, G.P.O. Box 498, Adelaide, South Australia, 5001.

Abstract

The aim of this investigation has been the experimental evaluation of the effects of Mach number, density and geometry on the flow structures in a turbulent jet and its radiated noise. An extensive experimental programme is described in which the range of flow conditions tested, with the density ratio ρ_J/ρ_o varying from 0.2 to 4.0 and Mach number U_J/a_o in the range of 0.2 to 2.4, is wider than any previous studies, especially in the density range spanned.

The flows in the required density range are shown to be achievable simply by using mixtures of gases of different molecular weights such as helium, sulphur hexaflouride, carbon dioxide and air as working fluids. With the short running time blow-down facility, tests can be carried out economically as modest amounts of gas are used in each run. The novelty of this set up is that it is a simple matter to vary the density and velocity independently of each other.

A range of nozzles with different geometries are examined to find the effect of jet geometry on the noise radiated. In addition to the convergent nozzles, three convergent-divergent nozzles of design Mach numbers 1.3, 1.54 and 1.75 are used to study supersonic flow effects.

The acoustic measurements described are conducted in an anechoic chamber which has a cut-off frequency of 25 Hz. Flow and acoustic data are sampled digitally by a high speed data acquisition system which has a 16 K memory and is capable of sampling at a rate of 100,000 Hz over up to 16 channels simultaneously at full capacity. The acquired data are analysed in a computer.

Flow visualization in this study has confirmed the existence of large scale structures in the initial mixing region of both subsonic and supersonic jets from which a large proportion of jet noise is shown to originate.

These structures are shown to dominate and control the development of the mixing layer. The amalgamation processes of the large scale structures are accompanied by large entrainment of irrotational fluid in the mixing layer and they dominate the near field pressure and velocity fluctuations. This observation encourages the belief that these large scale transient motions are efficient sources of noise.

The average convection speed of the flow and the spreading rate of the jet mixing layer are found to be very much density dependent. While the measured convection speed varies with radial position across the layer, the average speed, which is taken as the mean of the values in the non-entrained regions of the jet, varies from (0.38 - 0.72) U_J for ρ_J/ρ_o in the range between 0.17 to 4.0, as opposed to the normally accepted value of 0.63 - 0.67 U_J regardless of density. The observed lower convection speed in a lighter jet and the observed higher spreading rate of the mixing layer $\Delta\delta/\Delta x$ is consistent with Brown's mixing layer model (A2) where the total entrainment depends only on jet velocity and is independent of density. At high Mach number significant thinning of the layer, brought about by compressibility effects, is observed and when the local flow speed is supersonic, Mach waves are seen to radiate in the forward arc direction.

Jet velocity and density have a profound influence on the noise radiated. The overall intensities of the sound measured at $\Theta = 90°$, when normalised by $(\rho_m/\rho_o)^2$ in accordance with Lighthill's scaling law in equation (1.1), show that non-uniform density jets are noisier at low velocity. At high Mach number, compressibility, which affects the development of the transverse scale of the motion, produces a significant thinning of the layer which results in a reduction in noise intensity from the $(U_J/a_o)^{8.0}$ scaling law. The noise intensities of non-uniform jets at low Mach number, which scale to about a sixth power of velocity, suggest that the excess noise source is

dipole in character.

In spectral scaling, the dimensionless frequency $f_s D/U_c$ is chosen since the major effect of density is to change the convection speed and hence the characteristic time D/U_c for the life of the large eddies. A better collapse of the spectra is obtained using the frequency parameter $f_s D/U_c$ than using $f_s D/U_J$, which indirectly suggests the close relationship of these large scale structures to the noise.

The acoustic measurements are also compared to the published data of Tanna (D2) on hot jets and Lassiter & Hubbard's results (D9) for freon and helium jets. The close agreement between the present results and the hot jet results suggests that for jet noise the effect of density is the same whether it be brought about by a change in temperature or by a change in composition. The validity of Morfey's jet noise prediction scheme for non-uniform density jets is also verified by the present results.

In an amalgamation process, the rotational flow field of the large structures and the large entrainment of fluids from the ambient and potential core regions resemble the flow field of a dipole pair. Thus a model of the noise source is proposed where the strengths of an opposing dipole pair are approximated by the entrainment velocities. Although the model does not represent the real flow exactly, it is physically realistic and experimentally compatible and it offers an interpretation of the role of dipole and quadrupole sources in jet noise. In a uniform density jet the dipoles are of equal strengths and the dipole-pair degenerates into a quadrupole. In a non-uniform density jet, the unequal entrainment velocities of the irrotational fluids represent dipoles of unequal strengths. They do not cancel exactly and the uncancelled part of the dipoles radiates like a dipole in the far field.

TABLE OF CONTENTS

STATEMENT OF ORIGINALITY

THE MATERIAL IN THIS THESIS IS THE ORIGINAL WORK OF THE AUTHOR AND CONTAINS NO MATERIAL PREVIOUSLY PUBLISHED OR WRITTEN BY ANOTHER PERSON EXCEPT WHERE DUE REFERENCE IS MADE IN THE TEXT. THE THESIS DOES NOT CONTAIN WORK THAT HAS BEEN ACCEPTED FOR THE AWARD OF A DEGREE OR A DIPLOMA AT ANY UNIVERSITY.

LEE HOCK SENG

ACKNOWLEDGEMENTS

The author would like to express his sincere appreciation to the following individuals for their assistance towards the completion of this thesis.

To Professor G.L. Brown for his initiation of this project, his supervision, advice, discussions and suggestions in the first thirty months of this work before he left for California Institute of Technology in United States. Also, for his valuable discussions and comments in the preparation of this thesis.

The author is most grateful to the head of the department, Professor R.E. Luxton for his constant support, encouragement and provision of the necessary stimulus to bring this work to a conclusion; his supervision in the later half of this research; his many helpful comments and discussion on the preparation of this thesis.

To the Laboratory Manager, Mr. D. Kerr and the technicians, Mr. D. Morrison and Mr. G. Price for their excellent workmanship and co-operation.

To Mr. H. Bode and Mr. P. Walker for their maintenance and servicing of the optical, sound and electronic equipments used in this experiment. And to the many laboratory technicians who had assisted in the course of this experiment.

The work was made possible by the funding of the Australian Research Grant Council and the University Research Grant.

LIST OF SYMBOLS

a_o	Ambient speed of sound.
a_J	Local speed of sound in the jet.
a_m	Local speed of sound in the mixing region of the jet.
C_p	Specific heat at constant pressure.
D	Nozzle diameter.
f	Measured frequence.
f_N	Frequency parameter $f_s D/U_c$.
f_s	Source frequency or doppler corrected frequency.
g	'excess' density $(p - a_o^2\rho)$.
H	Nozzle width (2-D nozzle).
$I, I(\underset{\sim}{x})$	Far field sound intensity.
L	Lighthill's scaling parameter.
ℓ_c	Local characteristic turbulence length scale.
M	Flow Mach number U/a_o.
M_J	Jet exit Mach number U_J/a_o.
M_c	Eddy convection Mach number U_c/a_o.
p_o, p	Ambient pressure and local hydrodynamic pressure.
p_{ij}	compressive stress tensor.
q	Source distribution function in Lighthill's inhomogeneous wave equation.
R	Distance of far field observer.
r	Velocity ratio of the free streams in 2-D mixing layer.
$R_{x_1 x_2}(\tau)$	General normalised covariance stationary cross correlation function.
$R_{x_1 x_2}(\xi,\tau)$	Longitudinal normalised cross correlation coefficient.

S	Strouhal number fD/U_c.
s	Density ratio of the free stream in 2-D mixing layer.
s'	Entropy fluctuation.
t	Real time.
T	Characteristic period in the flow velocity fluctuation.
T_{ij}	Lighhill's applied stress tensor.
U_J, U_c	Jet exit velocity, eddies convection velocity.
$\overline{V}_{e_i}$	Mean entrainment velocity in mixing layer.
x_i	Axial jet coordinate.
α	Ribner's fluctuation parameter.
γ	Ratio of specific heats.
δ	Shear layer thickness.
δ_{vis}	Visual shear layer thickness and
δ'_{vis}	Visual shear layer growth rate $(\Delta\delta_{vis}/\Delta x)$.
λ	Acoustic wavelength.
$\overline{\lambda}_J, \overline{\lambda}_o$	Ratios of entrainment velocity in the potential core and the entrainment region to the jet velocity. $((\overline{V}_{e_J})/U_J, (\overline{V}_{e_o})/U_J)$
ν	Kinematic viscosity.
ξ_x	Axial separation of the probes.
ρ_J, ρ_o	Jet and ambient density.
ρ_l, ρ_m	Local and mean density in the flow.
τ	General time delay.
τ_{ij}	Viscous stress.
ϕ	Angular position in jet exit plane.
θ	Emission angle from the jet axis.

1. INTRODUCTION

Although Lighthill's classical theory of aerodynamic noise, formulated in 1952, has provided a mathematical foundation, predictions have depended upon dimensional arguments for the source terms and description of the physical nature of the noise sources has not been clarified. Quantitative prediction of the sound output depends on a knowledge of the turbulence in the flow region. The turbulent flow model available to Lighthill at the time, for which there existed a theoretical description adequate enough to allow calculation of noise radiation in the far field, was that of homogeneous isotropic turbulence. In his idealised model the flow is divided into a large number of compact subregions ($\ell/x<<1.0$, where ℓ is the characteristic length scale of the flow) which fluctuate and radiate in an uncorrelated manner such that their intensities can be added in the far field to give the total intensity.

Lighthill (B1, B2) chose the R.M.S. velocity as the characteristic velocity fluctuation and the integral scale of the turbulent flow as the length scale and on these dimensional grounds arrived at his U^8 dependence for the overall intensity. From the mathematical foundation he concluded that the turbulent flow was equivalent to an array of convecting quadrupole sources radiating into a medium at rest.

While Lighthill's result is able to predict many of the features of jet noise, the actual flow in the mixing region of a turbulent jet, from which a large proportion of the jet noise is known to originate, is far from being isotropic. The correlation measurements of the flow in this region (A1 - A19) have indicated the correlation length scale is at least in the order of the mixing layer thickness. More recently, sophisticated techniques

employed in the study of turbulence have revealed the existence of quasi-orderly structures in large scale vortex like motions, in two dimensional mixing layers and similarly convecting large structures in axisymetric jets. These organised large scale motions are identified as the rolling up of the shed vorticity in the shear layer, due to the initial instability, into concentrations of vorticity as observed in many experiments (A1 - A20). Brown and Roshko (A1), Winant and Browand (A3) showed that in two-dimensional mixing layers it is the interaction between these structures as they convect downstream that controls the entrainment, mixing and spreading of the layer. These observations have led to a much better understanding of the flow and the dominant role played by the large structures has led to the belief that they are also efficient sources of noise.

This belief is enhanced by the work of other authors. Mollo-Christensen (A10) showed that the pressure fluctuations outside a turbulent jet were composed of well defined wave packets in which dominant frequency components preserved their phase relationship over large distances.

From the supersonic jet experiments of Bishop, Williams and Smith (C7), it was concluded that the noise sources in a supersonic jet have a scale which is the order of the shear layer thickness. The large structure are the obvious features in the flow to possess such a scale.

While the direct connection between the structures and the flow is unknown, their intimate relationship is demonstrated by Crow and Champagne (A5) and C.J. Moore (D3). Periodic surging at a specific frequency and amplitude upstream from the nozzle, as in the experiment of Crow and Champagne, can interact strongly with the structures. Forcing is found to amplify the corresponding

wave which grows in the initial stage of the jet flow development until a saturation limit is reached. This limit is dependent on the surging frequency and it is the largest for Strouhal number $fD/U_J=0.3$ where f is the forcing frequency, D the nozzle diameter and U_J the jet velocity. A disturbance of a small magnitude is sufficient to cause the growth to decay to take place earlier in the shear layer.

The effect of flow modification, as a result of forcing, on the radiated noise is evident in the work of Moore (D3) who reported that the far field noise is increased when the jet is excited by a fluctuating pressure as low as 0.08% of the total dynamic head over the whole subsonic range.

With these new insights into the nature of shear flow turbulence and the effect of its development on radiated noise, one of the objectives of this work was to study the behaviour of the large scale structure, its influence in the near field pressure and velocity fluctuations and the possible connection between the structures and the radiated noise, the latter was explored particularly by varying over a wide range both the density ratio of the jet to ambient fluid and Mach number of the jet.

This work was motivated in part by the fact that in turbulent mixing layers, two parameters which are found to have significant effects on the shear layer developments are the density and velocity ratio across the layer. Brown (A2) concluded from his entrainment rate measurement in two-dimensional mixing layers that;

(1) The total rate at which fluids enter the layer is dependent on velocity ratio and weakly dependent on density ratio,

(2) The proportion of the total entrainment contributed by each fluid is determined only by its relative density regardless of whether it is on the high speed or low speed side of the

layer.

Reconciling these observations with a simple model of the flow, Brown (A2) concluded that the convection speed of the structure in the flow, U_c was density dependent and the predictions were consistent with the convection speeds obtained from pictures of the mixing layer as described in Brown and Roshko (A1). This result is contrary to the bulk of published jet noise work where U_c is taken to be roughly 0.63 to 0.67 U_J regardless of jet density.

In further developments in the theory of jet noise (eg. Lush, Ffowcs Williams, Lilley etc) this convection speed is shown to be a significant component in the predictions of jet noise. An incorrect assumption for the convection velocity could result in a poor estimation of convection amplification and incorrect Doppler shifting of the measured frequency to the source frequency.

The subsequent evaluation of the convection speed in these experiments takes advantage of the simple model proposed by Brown. The essential features of the model are described in Appendix A.

From Brown's model (see Appendix A) the flow structures' convection speed can be deduced and also the average density in the layer can be obtained by the entrainment rate and using the conservation of mass. Both of these parameters are important in the theoretical model for jet noise.

Jet noise radiation is frequently examined in terms of Lighthill's model analysis which yields for the intensity I the expression

$$I = \frac{\rho_m^2 U_J^8 D^2}{\rho_o a_o^5 R^2 (1 - M_c \cos\theta)^5} \qquad (1.1)$$

where ρ_m is the average density in the mixing region, U_J is the jet

exit velocity, D is the nozzle diameter, ρ_o and a_o are the ambient density and speed of sound respectively, R is the distance of the observer from the source and $M_c = U_c/a_o$ where U_c is the source convection velocity. At low velocities, hot jet data of Hoch et. al. (D6) and Tanna (D2) showed that the noise intensity can not be scaled by the source density ρ_m alone where ρ_m was assumed to have any value between the jet and ambient fluid density.

Thus the 'excess' noise observed in the hot jet at low mach number is at the moment an issue of controversy. While some attribute this noise to additional sources, others believe the increase to be due to the acoustic-mean flow interaction.

Mani (D11) puts forward the idea of the mean flow shrouding the radiation of the convective quadrupole as an explanation of the excess noise problem. His analysis shows that shrouding can increase the radiation efficiency of a quadrupole to that of a monopole and he supports his arguement by showing the consistency of his model with the hot jet result of Hoch et. al (D6). However, Kempton (C12) shows that Mani's results were in fact in error and goes on to demonstrate that the acoustic scattering by a density gradient can only enhance the efficiency of a quadrupole to that of a dipole at best.

Following the approach of Mani, Dowling (C4) suggested a model of a particle attached quadrupole positioned near an initially unstable free vortex sheet combined with additional source generated by the flow as it grows into turbulence. Her model predicts that when the jet density is very much lower than its surrounding the mean flow-acoustic interaction results in a considerable amplification of the quadrupole field to the extent that the intensity can scale on a lower power of velocity. She claims a fourth or even a second power of velocity is possible if the jet density is low

enough.

For those who favour the additional source argument, a few theoretical models have been presented recently. To follow their arguments, it is convenient to express Lighthill's acoustic analogy equation for sound generation in an arbitrary fluid flow (with viscous stresses neglected) in terms of pressure. In the absence of body forces and fluctuating mass addition, it is expressed as

$$\frac{\partial^2 p}{\partial t^2} + a_o^2 \nabla^2 p = a_o^2 \frac{\partial^2}{\partial x_i \partial x_j} (\rho U_i U_j) + \frac{\partial^2}{\partial t^2} (p - a_o^2 \rho), \qquad (1.2)$$

which can be expressed as

$$L(p) = q_1 + q_2 \qquad (1.3)$$

where L = wave operator $= (\frac{\partial^2}{\partial t^2} + \nabla^2 a_o^2)$ and $\nabla^2 = \frac{\partial^2}{\partial x_i^2}$,

i.e. $$q_1 = a_o^2 \frac{\partial^2}{\partial x_i \partial x_j} (\rho U_i U_j), \qquad (1.4)$$

and $$q_2 = \frac{\partial^2}{\partial t^2} (p - a_o^2 \rho). \qquad (1.5)$$

The source term q_1 is the familiar Reynolds stress tensor whose far field radiation intensity is given in equation (1.1). In the second source term q_2 Lush and Fisher (D7) in their approach divided the density fluctuation into 2 parts; one part is isentropically related to the pressure and the other to entropy fluctuation at constant pressure. They wrote

$$\rho = \frac{p}{a^2} - \frac{\bar{\rho} s'}{C_p}$$

so that

$$q_2 = \left(1 - \frac{a_o^2}{a^2}\right) \frac{\partial^2 p}{\partial t^2} + \frac{\bar{\rho} a_o^2}{C_p} \frac{\partial^2 s'}{\partial t^2} \quad (1.6)$$

For the hot jet they argued that the middle term in equation (1.6) was small compared to the first (i.e. $a > a_o$) and that the entropy fluctuations were proportional to the difference in entropy values across the layer i.e. $s' \sim s_J - s_o = C_P \ell n \ (T_J/T_o)$, the resulting scaling law for the intensity arising from q_1 and q_2 in this model is

$$I \sim K_1 \left(\frac{U_J}{a_o}\right)^8 + K_2 \left(\frac{U_J}{a_o}\right)^4 \quad (1.7)$$

where

$$K_1 \propto \left(\frac{T_J}{T_o}\right)^{-1} \text{ and } K_2 \propto \left(\frac{T_J}{T_o}\right)^{-1} \left(\ell n \frac{T_J}{T_o}\right)^2 \quad (1.8)$$

They claimed that the scaling law in equation (1.7) and equation (1.8) agreed with the experimental results for overall intensity at 90^o to within 1 - 2 dB over $a_o U_J/a_o$ range of 0.3 - 1.0.

Morfey (C10) in his analysis on the noise from inhomogenous flows claims that if the effects of viscosity and heat conduction are neglected, then the entropy change following a particle, DS/Dt, is zero. Hence the density and pressure inside the flow are related by

$$\frac{Dp}{Dt} = a^2 \frac{D\rho}{Dt} \quad (1.9)$$

From his mathematical analysis, he concludes that in jet flow where temperature or density inhomogeneities exist, only two source terms

are important ie.

$$q_T = a_o \frac{\partial^2}{\partial x_i \partial x_j} (\rho_o U_i U_j) + a_o^2 \frac{\partial^2}{\partial x_j} \left(\frac{\rho-\rho_o}{\rho} \frac{\partial p}{\partial x_j}\right) \quad (1.10)$$

The Reynolds shear stress term, $\rho_o U_i U_j$, in this case is evaluated at ambient density ρ_o and not the source density ρ. It appears that Morfey's model is unable to predict the observed decrease in jet noise with decreasing density at high velocities. However, he argued that at high velocities the wave length of the sound radiated becomes small compared to the shear layer thickness and the radiation due to Reynolds shear stress must be evaluated at the source density. The resulting scaling law becomes

$$I \sim K_3 \left(\frac{U_J}{a_o}\right)^8 + K_4 \left(\frac{U_J}{a_o}\right)^6 \quad (1.11)$$

where $K_3 \propto \rho^2$ and $K_4 \propto \left(\frac{\rho-\rho_o}{\rho}\right)^2$.

A third approach is due to Lilley (B9) who used the method of matched asymtotic expansions in which the pressure fluctuation in the flow is matched to the far field radiation. By using the mass, momentum and energy equation, the pressure term in equation (1.2) is replaced by a density and enthalpy term which results in a scaling law for the total far field intensity I in the form

$$I \sim C_1 \left(\frac{U_J}{a_o}\right)^8 + C_2 \left(\frac{U_J}{a_o}\right)^6 + C_3 \left(\frac{U_J}{a_o}\right)^4 . \quad (1.12)$$

For the constants in equation (1.12), C_1 scales as $(\rho/\rho_o)^2$, the ratio of C_2/C_1 is of the order unity and the ratio C_3/C_1 is proportional to $\left(\frac{h_{sJ}}{h_o} - 1\right)$ where h_{sJ} and h_o are the stagnation enthalpy

of the jet and the ambient static specific enthalpy respectively. Lilley showed that the ratio of C_3/C_1 is similar to the ratio of the forth to the eighth power velocity term in (1.7) as

$$\left(\frac{h_{sJ} - h_o}{h_o}\right) = \frac{C_p T_J - C_p T_o}{C_p T_o} = \frac{T_J - T_o}{T_o} \qquad (1.13)$$

Although the theoretical models discussed above are apparently contradictory, each model claims to be in good agreement with the available hot jet data. A further objective of this experiment is therefore to shed some light to the 'excess' noise in inhomogeneous jets through acoustic measurements over a wide range of density ratio and Mach number conditions. In this experiment, the jet density range covered is wider than any previous work where only jets of density lighter than air were studied. By using gases of various compositions (i.e. helium, carbon dioxide, sulphur hexafluoride and air), jets in the density range ρ_J/ρ_o from 0.2 to 4.0 were studied. With the short running time blow-down rig and the designed nozzles (one convergent plus three convergent nozzles of nominal Mach number 1.3, 1.54 and 1.75), the velocity range covered is $0.2 < U_J/a_o < 2.4$.

In this work the density and Mach number effects on the flow convection speed and spreading rate of the shear layer have been determined experimentally and compared with Brown's mixing layer model. The usefulness of the convection speed and average mixing layer density, as parameters to describe jet noise, were also evaluated.

A physical model of jet noise generation is suggested where a dipole-pair whose strengths are proportional to the entrainment velocities of ambient fluids in the turbulent mixing layer is modelled as the source. Although the model cannot be theore-

tically justified, it does offer a simple and physical mechanism of jet noise generation which at least intuitively, is able to offer an explanation for the excess noise observed in non uniform density jets. It arises, in this model, from the unequal entrainment velocities on either side of the layer and hence unequal dipole strengths.

CHAPTER 2

2. EXPERIMENTAL FACILITIES

The experimental facilities used were designed specifically to study the flow structures and the radiated noise from a laboratory scale jet over a large range of density, Mach number and nozzle exit geometry.

Direct simulation of commercial jets in the laboratory by heating the air to achieve the right density ratio would require experimental facilities of a scale not normally found in universities. Apart from the complexities and expense of heating air, the problems of maintaining constant ambient temperature within the confined anechoic chamber and measuring flow parameters at high temperatures are extremely difficult.

In the present experiments the jet density was controlled by the composition of the flowing gas. In all cases the ambient fluid into which the jet discharged was air. The range of density ratio studied varied from $\rho_J/\rho_o = 0.2$ through to $\rho_J/\rho_o = 4.0$ by making use of gases such as Helium, Carbondioxide, air and sulphur hexaflouride.

To avoid the need for large quantities of working gases, some of which are expensive, a short running time blow-down facility, which allows constant stagnation conditions to be established in less than 500 ms, was built. Running times are typically in the order of a few seconds depending on flow conditions.

Such short running times necessitate instruments of very fast response and high speed data handling facilities. These are discussed in the following sections. The data acquisition system used for the majority of the measurements reported here can sample at any rate up to 100 kHz on five of the sixteen input channels.

The data is written onto a magnetic tape which can be processed by a computer.

Jet noise measurements were carried out in the reflection free environment in an anechoic chamber in which the background noise was negligible.

2.1 Jet and acoustic facilities

The joint flow and acoustic measurements of the jets described were carried out in the existing anechoic chamber of the Acoustics Laboratory of the Mechanical Engineering Department in the University of Adelaide.

The overall layout of the jet and acoustic facilities in the anechoic room are shown in Fig. 2.1. The reservoir of 5.5 m^3 capacity, which can be charged to a pressure of seven atmospheres, is linked to a steel pressure vessel, of 0.2 m^3, of the blow down rig situated just outside the anechoic chamber, by a 102 mm (4") diameter pipe, which was designed and installed for this experiment. The gas from the high pressure vessel is discharged to the plenum chamber via a 32 mm (1¼") diameter high pressure flexible hose by activating the solenoid operated valve. At the entrance to the plenum chamber a metering valve is installed to regulate the flow rate before the gas finally issues into the ambient field through the nozzle.

A microphone boom placed at a radius of 1.7 m from the nozzle exit allows the angular position of microphones to be varied between 20^{o} to 90^{o} from the jet axis.

The flow and the sound instrumentation are set up in the control room nearby from which the experiments may be operated and measurements monitored and recorded.

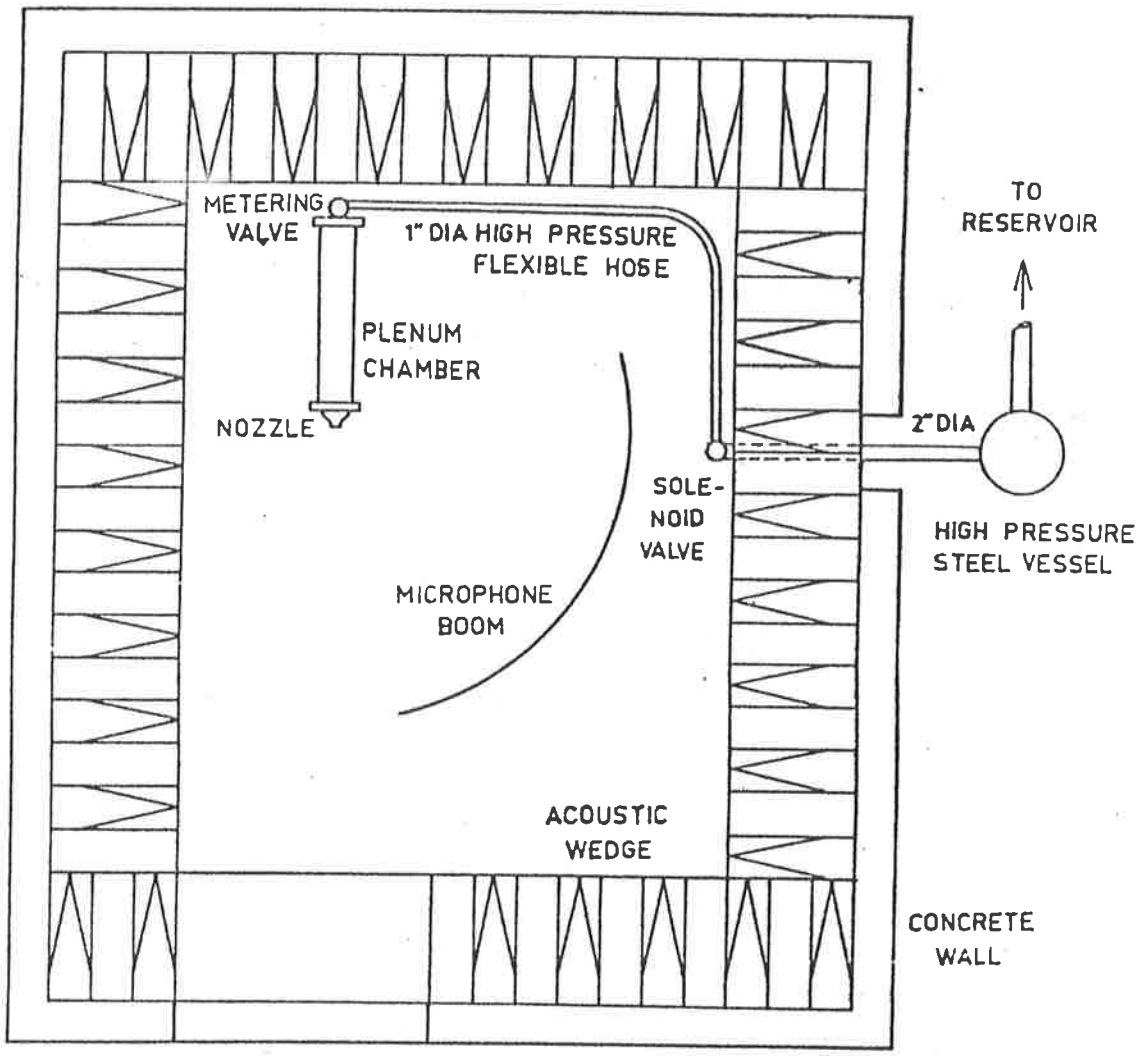

Fig. 2.1 Jet and Acoustic Facilities

2.1.1 Blow down rig

The blow down rig used throughout this experiment was designed and built in the Mechanical Engineering workshop in the University of Adelaide. It is designed for short running time jet and mixing layer experiments. With this rig, a jet within a nominal Mach number limit of 1.75 may be achieved using the convergent (for $M<1$) or convergent-divergent (for $M>1$) nozzles. The novelty of this rig is that jet flow in the density ratio range of 0.2 to 4.0 can be economically achieved by using gases of different composition such as helium, carbon dioxide, sulphur hexafluoride and air.

The rig shown in Fig. 2.2 consists of a steel vessel of 0.2 m^3 capacity which is linked to the air reservoir. Inside the vessel an airtight polystyrene bag is securely attached to the outlet end of the vessel. Gases of the desired composition can be introduced into the bag through the feedline and held in there to be discharged when the solenoid operated valve is electrically activated. This arrangement can provide a flow typically for the order of a few seconds (for example 5 seconds for U_J/a_o = 1.0 at a reservoir pressure of 6 atmosphere and a nozzle area of 6.5 x $10^{-4}m^2$ or 1 in^2). The pressure drop during the run is insignificant due to the small volume of gas discharged relative to the driving reservoir volume. (At the worst a 3.6% stagnation pressure drop can occur when the bag is collapsed completely.)

It must be pointed out that the blow down rig was designed for turbulent mixing layer and jet experiments in the department of Mechanical Engineering. Although the major components, namely the pressure vessel and the plenum chamber, were in the final stage of fabrication when this study commenced, considerable effort and time were spent on the design of the other components and in the commissioning of the system before it was operational. Not shown in Fig. 2.2 is the operational console where all the piping and fittings, for charging the working gases into the plastic bag inside the pressure vessel, are mounted together with the solenoid valve switch and the pressure gauges (for reading the reservoir and vessel pressure). A pressure switch, which essentially is a piece of rubber membrane with a conductor on one side, is clamped in between the flanges of the pipeline linking the bag to the reservoir. This switch senses the pressure difference between the bag and the reservoir and sets off a buzzer when the bag is full. The other safety feature installed in this set up is a fast purging valve for

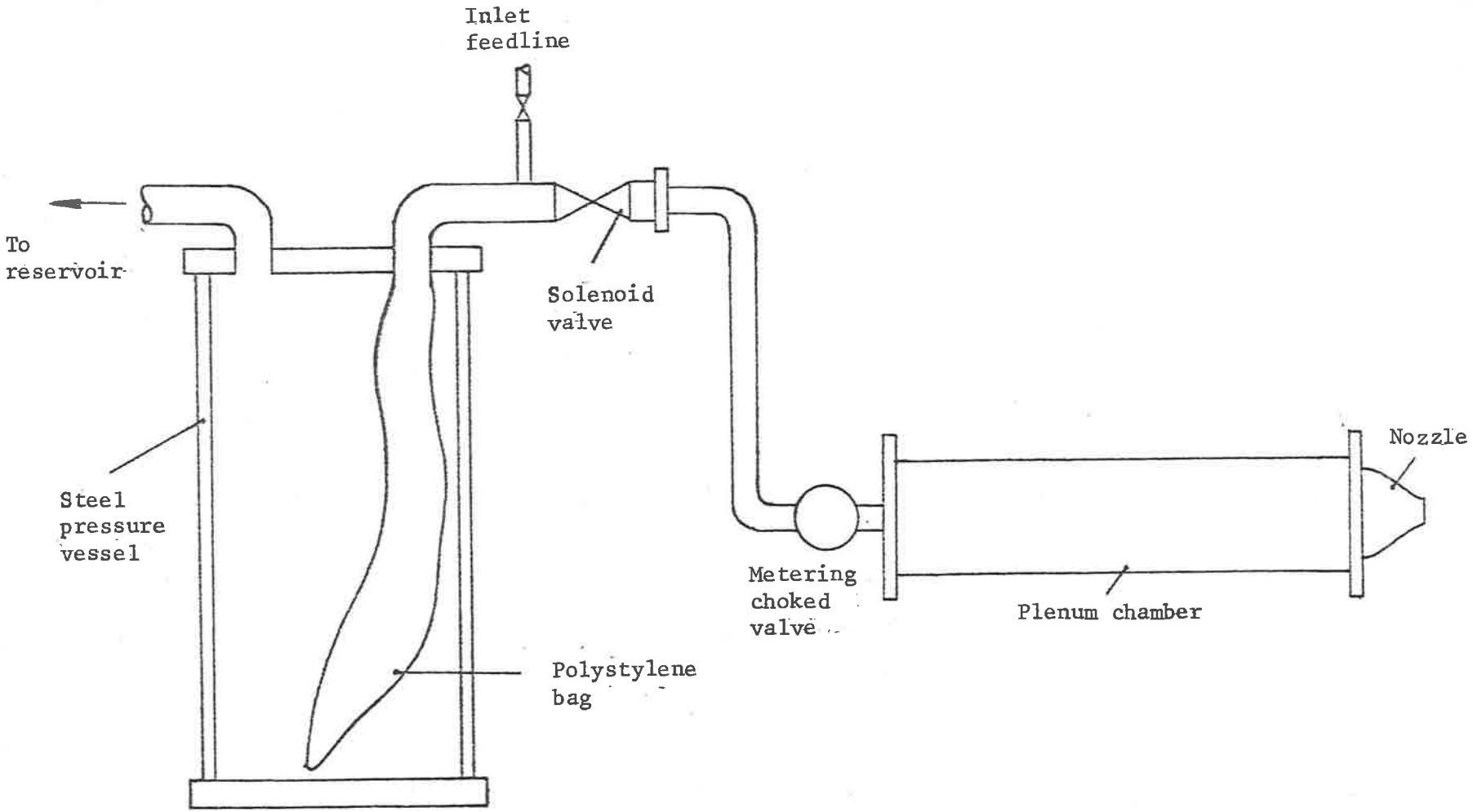

Fig. 2.2 The short running time blow-down facility

quick release of the gas from the bag to save the bag from bursting.

The jet velocity is regulated by the metering valve at the plenum inlet. Basically the metering valve has a moveable piston in a blanked cylinder which has an array of 150 holes, each of 1.25 mm diameter, in the wall. During each run, the pressure ratio across the holes is kept above the critical value so that sonic flow is established at the throat of each hole. The total volume flow rate is hence dependent on the number of open holes (or the total throat area) which is determined by the position of the piston.

For the supersonic jets, the metering valve is not used and the sonic flow occurs at the throat of the nozzle at the correct operating pressure.

2.1.2 Plenum chamber

The plenum chamber shown in Fig. 2.3 is a steel cylinder 0.2 m in diameter and 1.2 m long with a wall thickness of 2.0 cm. Before acoustic treatment, the flow noise generated from the metering valve was found to be too high for low velocity flow. Thus great care was taken to minimise this noise to an acceptable level.

The full length of the chamber is lined with a layer of sound absorbing fibre glass wool 3.0 cm thick. A series of punched-plate baffles with open area of 50% to 20% are installed along the chamber between the metering valve and the nozzle. A partial acoustic cover with lead and fibreglass lining is put over the valve such that there is no direct sound path for the valve noise. This arrangement is found to eliminate the valve and other internal noise. The result of the acoustic treatment is shown in Fig. 2.4 where curves (i) & (ii) are the 1/3 octave spectra of the valve noise (plus other internal noise) before and after the acoustic treatment mentioned above.

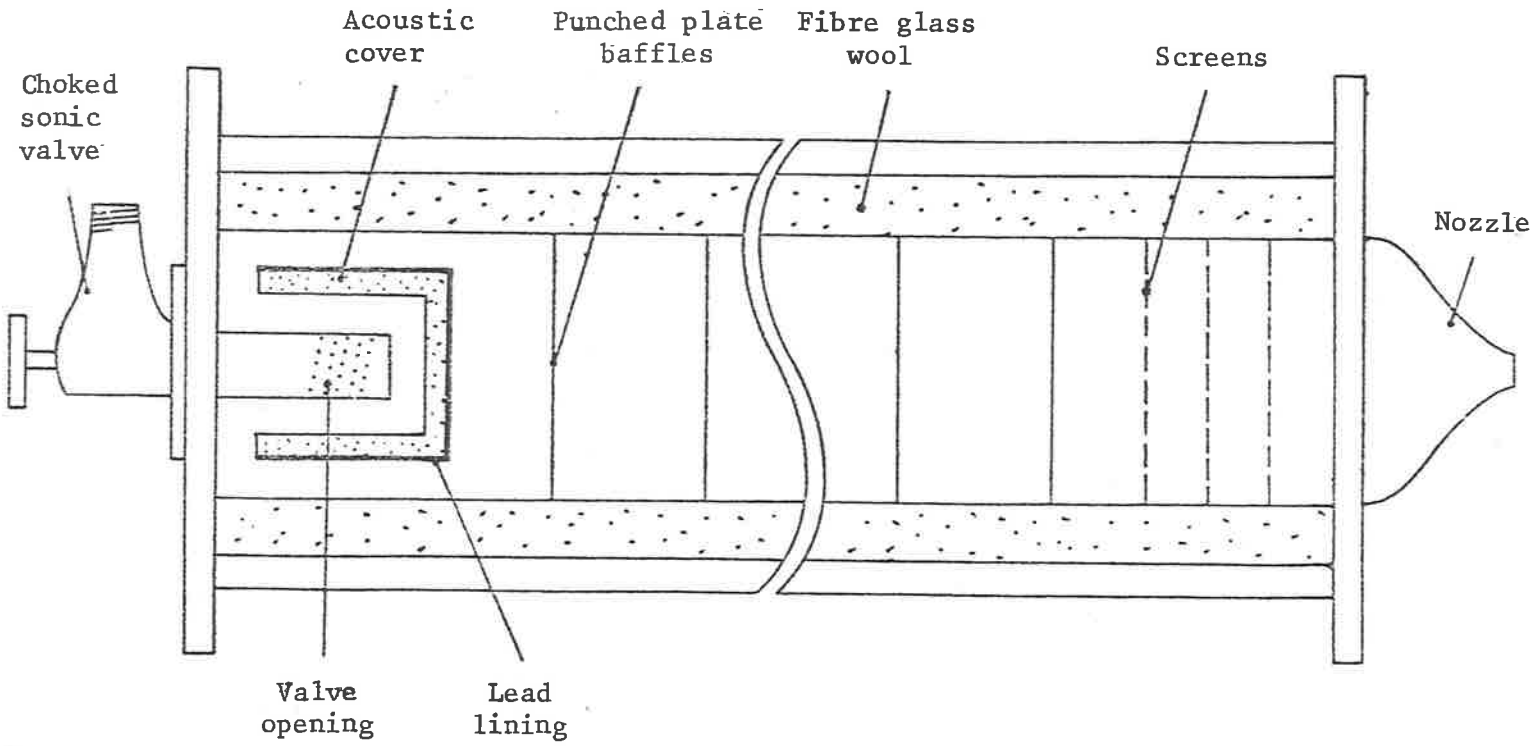

Fig. 2.3 Sectioned details of the plenum chamber

For the same mass flow rate through the valve the jet flow Mach number using a subsonic nozzle (exit area of 6.4 x 10 m^2) is 0.3 which is the lowest velocity of interest for the constant density case. At this flow condition, the mixing noise is seen to be higher than the internal noise at all 1/3 octave bands. Although the differences in levels in the frequency range 200 - 415 Hz are rather low (2 - 5 dB), the effect on the overall intensity is insignificant as the frequencies of interest in this work at the flow conditions considered are between 200 Hz to 40KHz, with most of the energy in the range between 1 KHz and 10 KHz.

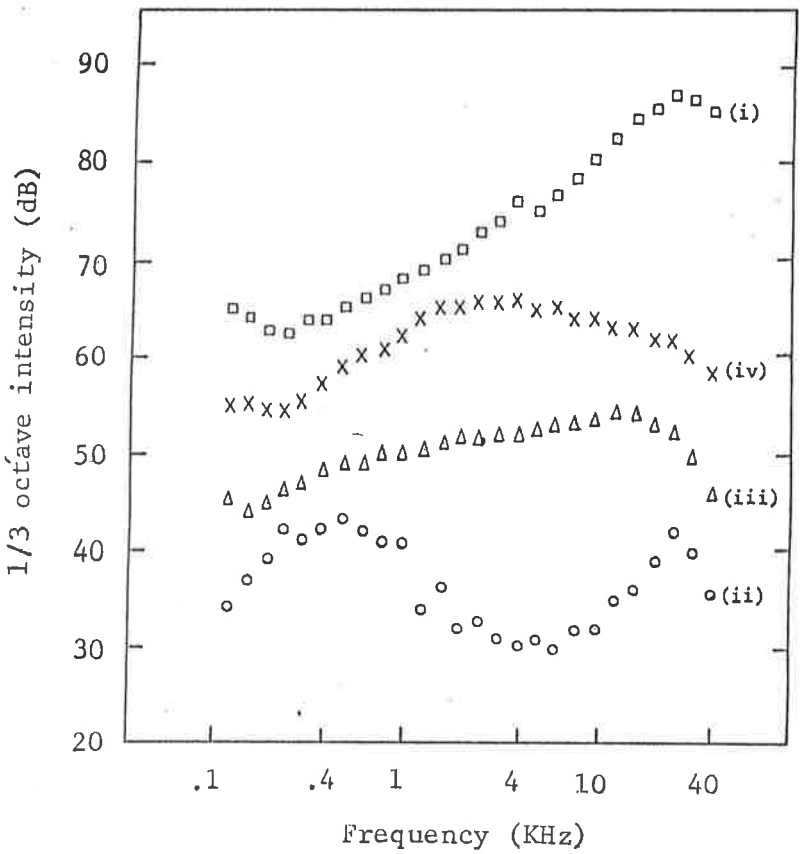

Fig. 2.4 Flow noise spectrum before and after acoustic treatment

(i) Valve noise before treatment (for flow rate of $U_J/a_o = 0.3$)

(ii) Valve noise after treatment

(iii) Jet noise spectrum ($U_J/a_o = 0.3$)

(iv) Jet noise spectrum ($U_J/a_o = 0.5$)

Since the flow through the valve is choked, the valve noise therefore varies with A* where A* is the total area of the open holes in the valve, and the spectral shape should remain the same except for a shift in the 1/3 octave intensities. The jet mixing noise however varies as $(A^*)^8$ according to Lighthill's U_J^8 law since the jet velocity varies with A*. At higher flow speed the difference in intensity between the mixing and valve noise was greater and the set up was found to be satisfactory.

For dense jets of $\rho_J/\rho_0 = 2.5$ and 4.0, flows at $U_J/a_0 = 0.2$ were also considered as the overall intensity levels were found to be higher than for the constant density case at $U_J/a_0 = 0.3$ (See Fig. 4.2).

Up to three wire screens of varying gauge are placed upstream of the nozzle to reduce the scale of the turbulence so that most would decay before entering the nozzle contraction. In this case the turbulence intensity at the nozzle exit is measured to be 0.8% which is typical for other laboratory jet flows at $U_J/a_0 = 0.30$.

2.1.3 Nozzles

For the subsonic jet studies, four convergent nozzles with exit geometries of round, square and rectangular (aspect ratios of 25:4 and 25:1) were designed and fabricated. All these nozzles have the same exit area of $6.4 \times 10^{-4} m^2$ (or 1 $inch^2$) and contraction ratio of 25:1. They are made from epoxy resin with a smooth internal contour to provide a uniform flow at the exit. In addition, three convergent-divergent nozzles originally designed for nominal Mach number (U_J/a_J) of 1.3, 1.6 and 1.8 are used. However, due to the boundary layer effect at the nozzle throats, the actual Mach numbers (U_J/a_J) for the correctly expanded jets are 1.3, 1.54 and 1.75 respectively. When using these nozzles a cone is fitted between the plenum inlet and the nozzle to reduce the time for the

flow to reach the steady operating condition. A list of dimensions and operating conditions of the nozzles is given in Table 2.1.

Mach Number	Subsonic	1.30	1.54	1.75
Flow stabilization time (ms)	300	335	450	570
Outlet diameter (mm)	28.7	20.96	21.00	20.00
Throat diameter (mm)		20.32	18.94	16.97

Table 2.1 Nozzle dimensions and operating characteristics

2.1.4 Anechoic chamber

The layout of the anechoic chamber is shown pictorially in Fig. 2.6 (plate 1). The dimensions of the chamber are 5.94 m x 6.86 m x 6.10 m (19.5 ft x 22.5 ft x 20 ft) in length. The room provides a free field environment which is anechoic down to 25 Hz and has a measured background noise level of 44 dB, which is much lower than the measured spectra at the lowest jet velocity of interest, as shown in Fig. 2.5.

The aluminium floor meshes in the chamber provide easy access to the instrumentation. The meshes are removed prior to the actual experiment to avoid reflection of higher frequency sound.

2.2 Flow and acoustic instrumentation

2.2.1 High speed digital data acquisition system

The multi-channel electronic data acquisition system was also designed and built in the Mechanical Engineering Department of the University of Adelaide.

The system is described in some detail by Thomas (E1). The multi-input unit enables 16 signals to be recorded simultaneously at a maximum sampling rate of 100,000 Hz. The input analogue signals are first converted into digital form with 8-bit precision

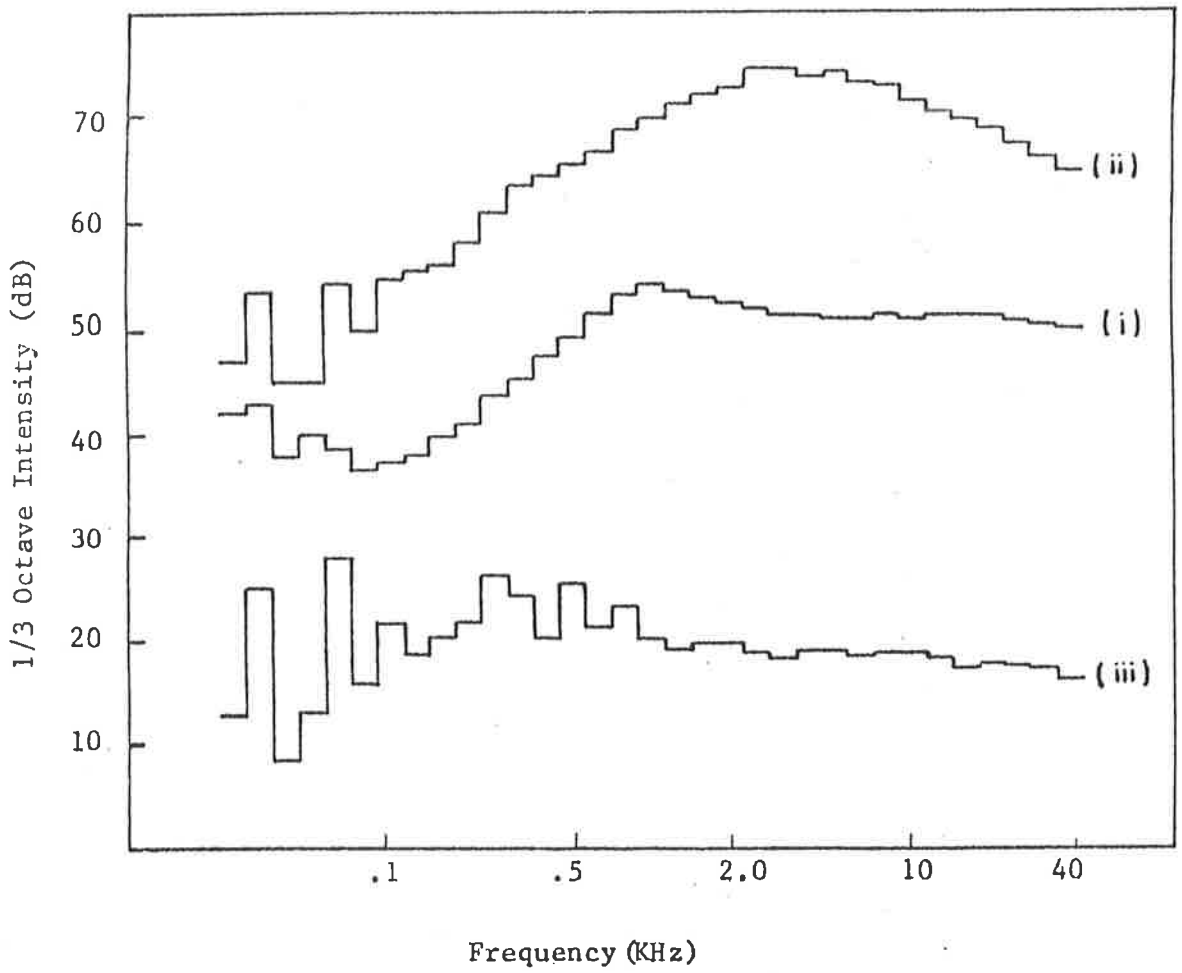

Fig. 2.5 Jet and instrumentation noise spectrum

(i) Jet noise ($\Theta = 45^{o}$, $U_J = 100$ m/s)
(ii) Jet noise ($\Theta = 45^{o}$, $U_J = 175$ m/s)
(iii) Background and instrument noise

written on a 16K shift register memory. With 8-bits precision, the input range of the system is divided into 256 divisions (2^8). The resolution of the digitised signal is therefore half the least significant bit which is = 0.2% of the input range. This unit is flexible in operation in that different sampling rate and memory space can be allocated to each channel independently. When the allocated memory is filled, the content of the memory is written onto a 9-track computer tape as a block of data or record.

The sampling rate, memory allocation, run identifier and number of records per run are programmable by a set of switches on the front panel. This information forms the preamble of each block of data written on the tape.

Because of the high sampling rate required in this experiment, the analogue to digital conversion time must be short. Of the 16 channels, five incorporate fast converters (Datel system model ADCHY12BC). Each of the converters has 12 bits and a conversion time of 8 μs. Since only 8 bits are used the short cycle capability in the converter reduces the conversion time to 4 μs. The internal buffer amplifier adds an extra 3 μs to the conversion time making a total of 7 μs per conversion.

The input voltage range of the A/D converter can be set to either 0 - 10 volts or ±5 volts. Since the inputs are fluctuating signals the ±5 volts range is used. The flow turbulence signals, which are typically in the order of milli-volts, have to be amplified before the conversion process to achieve adequate resolution. Signal amplifier units with carefully matched phase and frequency characteristics and variable gain from 1 to 100 are used. These units, described by Thomas (E1), have a band-width of 200 Hz to 70kHz at the half power point. The frequencies of interest (20 - 40 kHz) are all well within this range. The output signals from the microphone amplifiers are in the range of ±10 volts. Therefore to avoid clipping of the signals, they are divided down to bring them within the input range of the A/D converters.

The phenomenon of Nyquist frequency folding in digital sampling is that the signal component at frequencies above the 'folding' frequency, which is one half of the sampling frequency, will fold back about this frequency during the sampling process. It therefore appears as energy in the digitised signal at the lower frequency.

Throughout the experiments the sampling rate is kept at 100 Hz unless lower sampling rates are specifically required. The folding frequency in this case is therefore 50 kHz. In the turbulent signal most of the energy appears in the range below 10 kHz as shown in Fig. 3.8. Hence the error due to folding is insignificant even in the absence of filtering. In jet noise measurements, where the microphone response is flat up to 40 kHz, the signal monitored above this frequency rolls off at a rate in excess of 20 dB/1/3 octave. This effectively acts as a filter since energy frequencies above 40 kHz will have already been heavily attenuated before sampling.

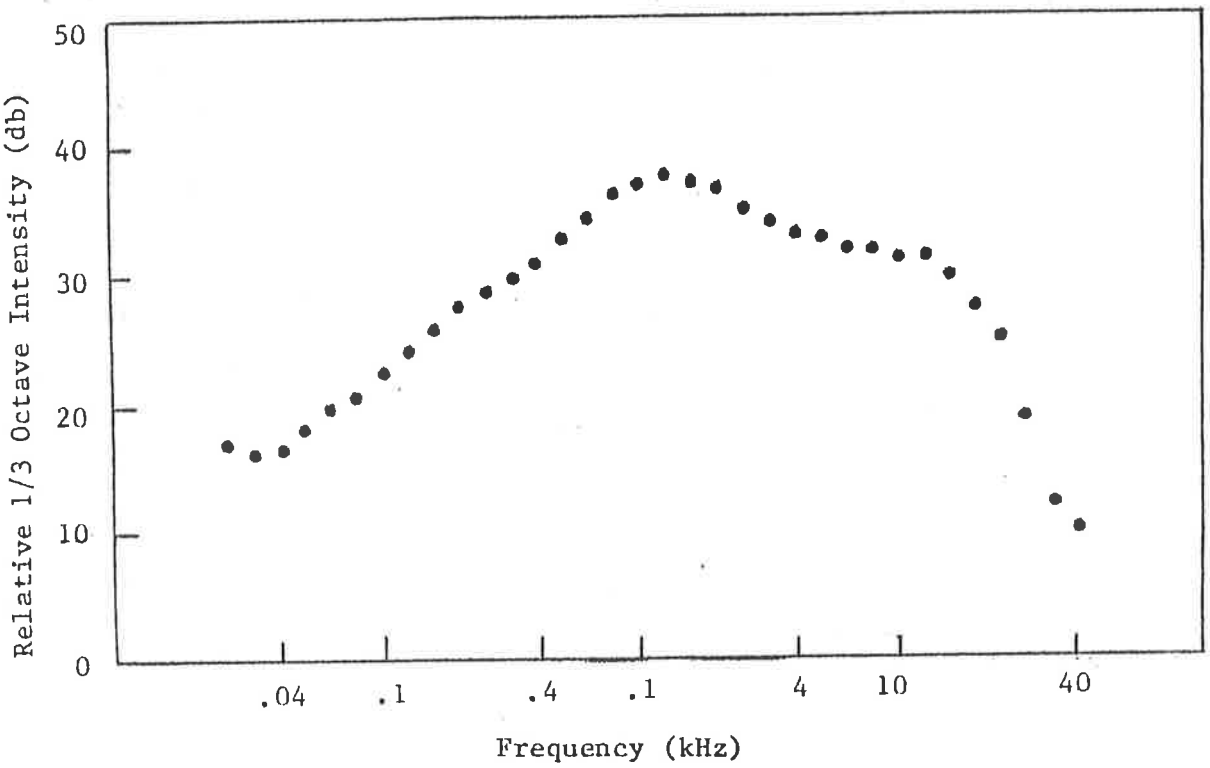

Fig. 2.8 Typical spectrum of a turbulent signal from a hot wire
(U_J/a_o = 0.5, X/D = 3, $\frac{Y}{D}$ = 1.0)

2.2.2 Hot-Wire anemometer

The hot wire probes and circuitry were also designed and built in the Department of Mechanical Engineering of the University of Adelaide. (For detail see Osborne (E2)).

In the velocity fluctuation measurements a single hot wire as shown in Fig. 2.9 was used. The needles for the probe are 0.5 mm jeweller's broaches set 3 mm apart. The wires are 5×10^{-6} m tungsten soft soldered to the needles. The ends of the wire are copper plated and the active unplated length is 1 mm giving a length to diameter ratio of 200. Constant temperature operation was used with an overheat ratio of 1:1.5. The cold resistance of the wires is typically 6.0 ohms. The time response of the wire and the feedback loop may be set by the square wave injection technique (see Thomas (E1)).

The constant temperature operation is achieved by the circuitry described by Thomas (E1). The circuit diagram is shown in Fig. 2.10. A high speed operational amplifier (National semi-conductor LM318) is used with a high performance power amplifier (2N2270) incorporated to boost the current output. Because of the high bandwidth of the operational amplifier, no trimming inductance is needed. The output offset is controlled by means of a 200 kΩ potentiometer connected to the internal offset control of the operational amplifier as there is no separate compensation network.

2.2.3 Acoustic measurement instrumentation

The acoustic measurements were obtained using standard sound measuring equipment. The set up in the control room is shown in Fig. 2.7 (plate 1). The far field acoustic radiation was measured at a distance of 1.7 metres from the nozzle exit by an array of microphones mounted on an arc in the plane of the jet axis at 20^{o}, 30^{o}, 45^{o}, 75^{o} and 90^{o} from the axis.

The microphones used were ½" condenser microphones (Bruel & Kjaer type 4133) with field effect transistor pre-amplifiers (Bruel & Kjaer type 2619). The free field frequency response of these

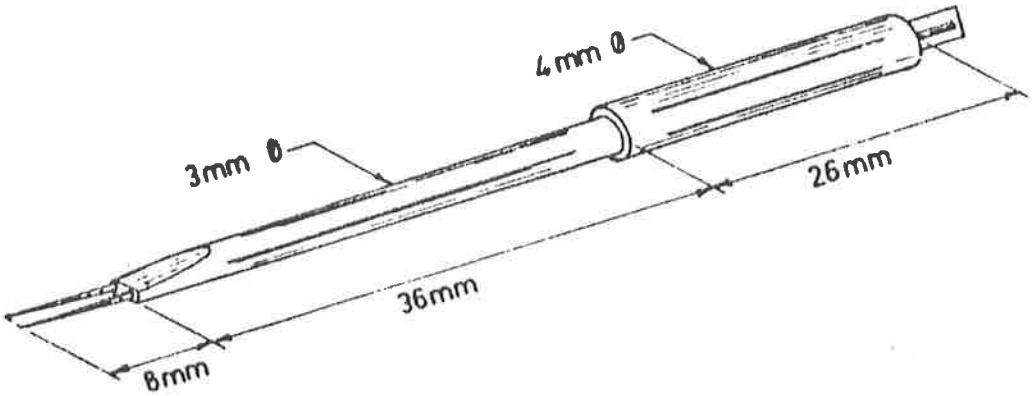

Fig. 2.9 Hotwire probe

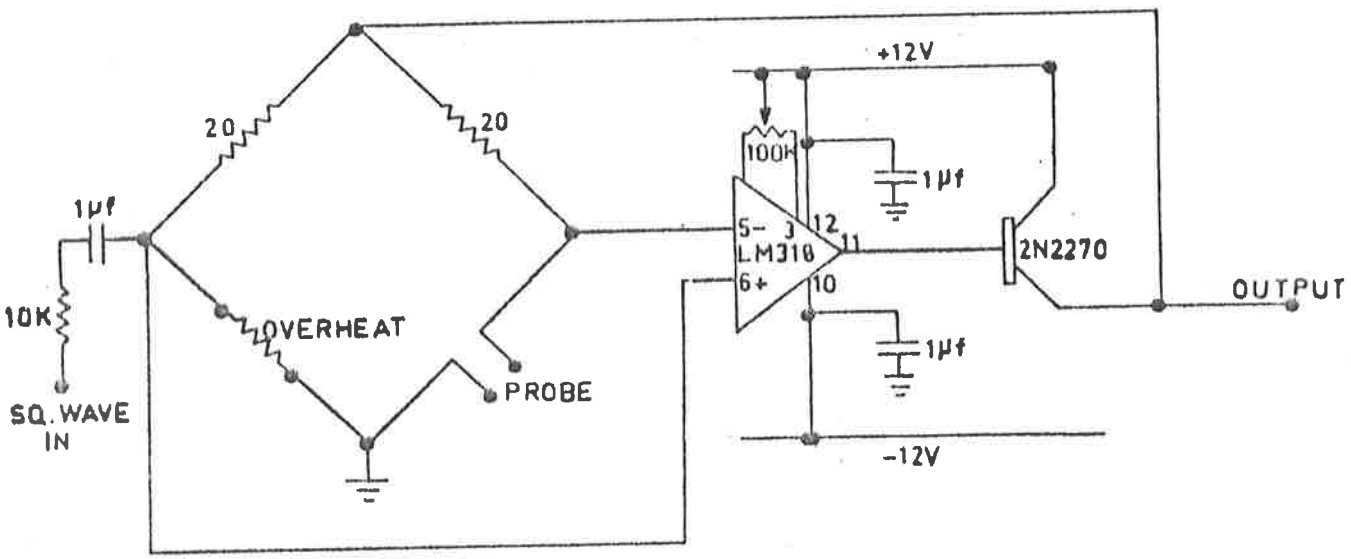

Fig. 2.10 Circuit diagram for the constant temperture feedback bridge

microphones is flat up to 40 kHz. During testing frequent checks were made on the microphone calibration using a 'piston phone' calibrator (Bruel & Kjaer type 4220). The outputs from the microphone amplifiers were attenuated to the ±5 volts input range of the Data Acquisition System. The recorded signals can be played back continuously into the real time 1/3 octave band analyser (Bruel & Kjaer type 3347) and the 1/3 octave intensities may be obtained. If required, the signals can be replayed at a rate 2^{-n} times the sampled rate (where $n = 1, \ldots.63$). The recorded data are processed in a computer, taking into account the frequency correction factors of the microphones to give the 1/3 octave and the overall intensities.

Standard practice is to examine regularly the instrument noise from the microphone and amplifier to ensure there is no possible contamination of the mixing noise. A typical spectrum of the instrument noise is shown in Fig. 2.5 together with a spectrum of the jet noise at the lowest velocity of interest U_J = 100 m/s. It is seen that the instrument noise has a much lower intensity level at all 1/3 octave bands than the mixing noise.

2.3 Optical observation facilities and technique

2.3.1 The Schlieren optical system

A basic 2-mirror folded schlieren system was used for optical observation of the flow and the acoustic field. The layout of the system is shown in Fig. 2.11.

The system incorporates two 203 mm (8") diameter front silvered spherical mirrors with identical focal lengths of 2438 mm (96") and 2 other front silvered plane mirrors.

In order to 'freeze' the motion of the turbulent flow a very short duration light source is needed for the one-shot picture.

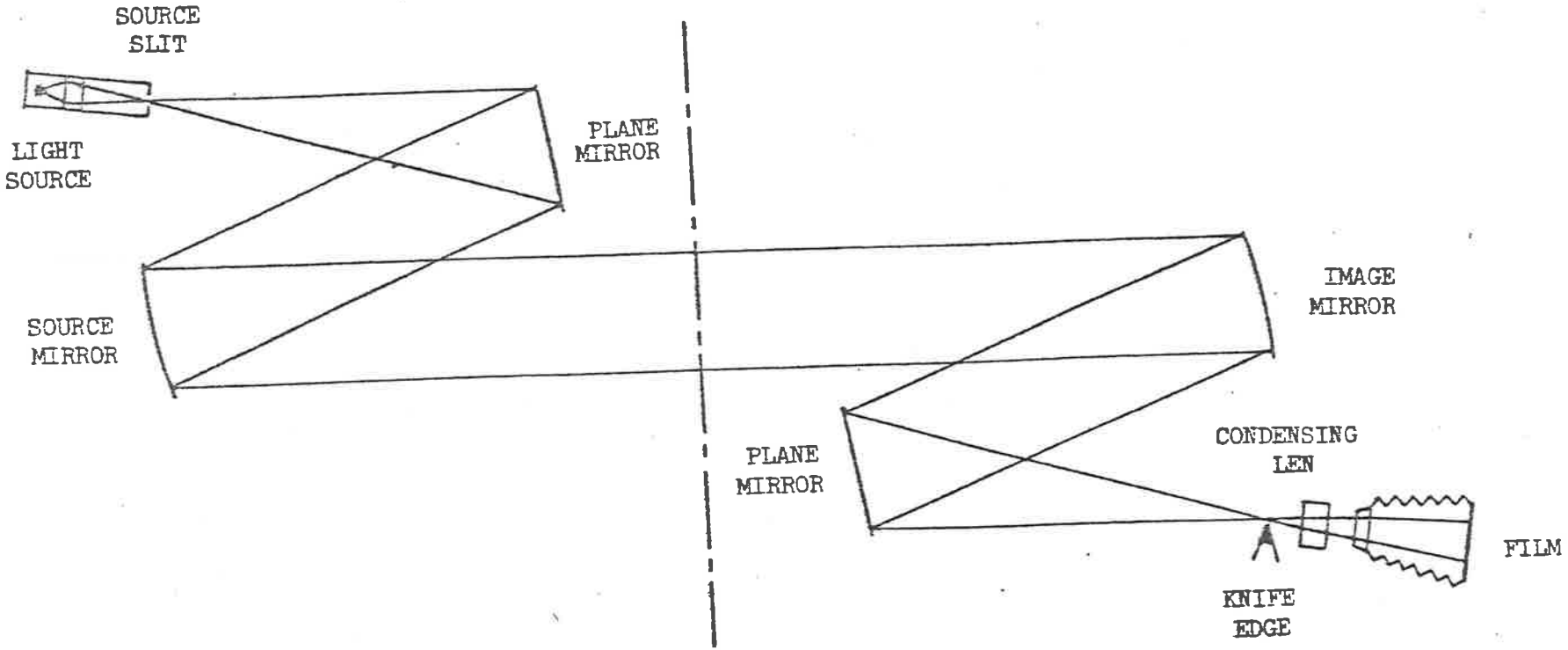

Fig. 2.11 Folded Schlieren System

A General Radio Strobotac 1538-A was found to be suitable. It produces a single flash of about 3 μs duration with enough light intensity to expose the film. The flash can be triggered externally by a mechanical switch. For continuous observation, a mercury arc source (Osram HBO 100 x/z) was used which has an effective arc size of 0.25 x 0.25 mm^2.

The knife-edge, condensing lenses and film holder were mounted on the same optical bench for easy alignment. The condensing lenses consist of 2 sets of lenses (one zoom lens and one standard 35 mm camera lens) which combine to give a large range of effective focal lengths. Normally a 3" x 4" Polaroid film was used but this could easily be replaced by a 4" x 5" flat film. For the high speed camera, the standard f/3.3 lens of the camera was used. In this case Kodak Tri-x reversal (7278 ASA 200) film was found to be satisfactory.

2.3.2 The high speed camera

In the early part of the experiment, a high speed Fastex rotating prism camera with a maximum framing rate of 7000 frames/second was used. However, the picture quality was found to be unsatisfactory especially at high speed. Later, an electronic camera (Imacon) which has a frame rate of 1 x 10^6 frames/second was used in an attempt to follow the sound waves. Six pictures each of $\frac{1}{2}$" x $\frac{1}{2}$" are exposed on a single $3\frac{1}{4}$" x $4\frac{1}{4}$" polaroid film. Because the photograph was of the image stored on the phospherous screen which has a relatively poor resolution of 13 linepairs/mm, this idea was also abandoned.

The high speed camera finally used in the study was a 16 mm rotating prism camera (Hycam 400'). It has a standard film capacity of 131.2 m (400 ft), but with simple accessories, it can accept

32.8 m (100 ft) or 65.6 m (200 ft) daylight loading spools. It has a maximum framing speed of 11,000 pictures/second using the 400 ft film. The synchronization of the film and the prism in the camera can produce pictures of extremely high quality with a resolution of 68 line pairs/mm at all framing speeds. The timing light in the camera produces a time-base reference on the film. The film speed is electronically controlled such that the framing rate can be maintained at the desired speed to ±1% accuracy. The speed control is a solid state electronic closed loop servo-system and the desired speed is set by a thumb dial.

The natural aperture of light transmitted in the camera is f/3.3, but a range of interchangeable shutters up to f/100 is available.

Another advantage of this camera is that it has an event synchroniser. The event switch can be triggered after a pre-determined footage of film has run through by means of a follower arm which rests on the film spool. The opening or closing of the event switch can be used to trigger either events such as the starting of the data system or the flow.

2.3.3 Timing light generator

To provide a time base on the film a timing light generator (Red Lake milli-mite timing light generator model 13-0001) is used to imprint timing marks on the film. It is a serial timing source operating with a frequency from a crystal controlled clock which has an accuracy of 50 parts in a million. In this mode of operation, it can drive a light emitting diode (LED) at 3 different rates of 10, 100 and 1000 Hz. The unit has been modified so that it can also operate from an external logic clock. In this mode of operation, the timing mark can be synchronised with other events or measure-

ments provided a common logic clock is used as a time reference.

2.3.4 Techniques of synchronization of flow, acoustic measurements and optical observations

The heart of the measurement system is the data acquisition unit with its internal logic clock as the reference timebase. The timing logic arrangement is illustrated diagramatically in Fig. 2.12.

The flow is turned on by closing the switch but a time delay is needed for the flow to reach the required operating condition before the camera is set rolling. After a predetermined footage of film has been exposed the built-in mechanism of the camera actuates the event synchroniser switch. The closing of this switch acts as an external trigger (or 'start' pulse)to start the data acquisition unit which can then acquire information. An 'enable' pulse is sent to the decade counter, with a maximum time delay of 20×10^{-9}s relative to the 'start' pulse, to set the electronic decade counter counting. The output from the decade counter then drives the timing light generator after each preset number of clock pulses is counted. The circuitry of this counter is designed such that a pulse is delivered to the timing light generator at the instance the 'enable' pulse reaches the counter. The first timing mark to appear on the film then corresponds tothe beginning of the signals acquired by the data acquisition unit. The subsequent marks correspond to a fixed delay in real time which can be easily obtained from the clock rate of the data acquisition unit.

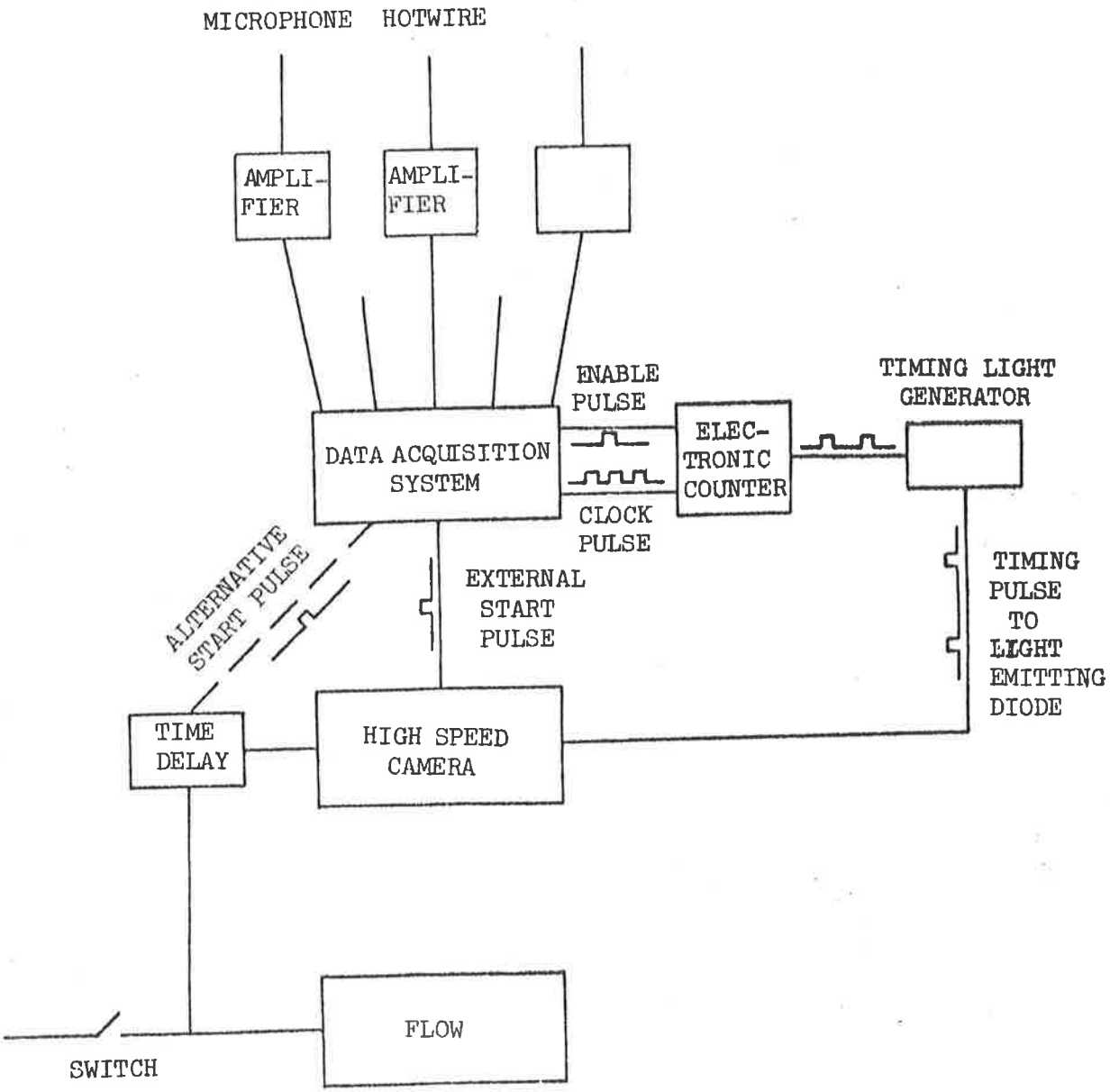

Fig. 2.12 Instrumentation for the synchronization of Measurements and Optical Observation

CHAPTER 3

3. JET FLOW STRUCTURES AND CHARACTERISTICS

3.1.1 Flow visualization

In this study, flow visualization combined with high speed photography was employed to provide a direct and simple method of obtaining qualitative informations on both the spatial and temporal development of the flow.

The one-shot shadowgraphs (plates 2 - 8) and high speed movies show that the intial mixing regions of round and two-dimensional turbulent jets are dominated by the large scale structures similar to those found in two-dimensional mixing layers. These large scale motions are seen to exist even when the jet flow is supersonic relative to the ambient speed of sound, as shown in Fig. 3.1 (plate 2), Fig. 3.16 and Fig. 3.17 (plate 9). In the transition region of the jet these structures are seen as distinct vortices with smooth boundaries which become less well defined in the turbulent region. The jet flow development can be easily followed in the high speed movies. The various stages of the flow development are represented diagramatically in Fig. 3.3. A vortex is formed at (B) as a result of the rolling up of the initial instability wave at (A). The vortex structure convects at nearly constant speed over a distance of 1 - 2 jet diameters until some irregularities in the eddy spacing cause one vortex to speed up and the preceeding vortex to slow down as at (C). As they get closer they spin around each other and eventually amalgamate to form a larger vortex at (D). The amalgamation process, which is an inherent part of turbulent mixing, is seen to be primarily responsible for the rapid broadening of the mixing layer as a result of the large entrainment of fluids from the potential core and the ambient surroundings. The randomness of these processes in time and in space result in the

mixing layer growth being smooth on the average. The vortex size and separation are observed to be increasing linearly with axial distance downstream from the nozzle exit.

In a high Reynolds number flow, the eddies are less recognisable as they are masked by fine scale turbulence. They exist as a lump of vorticity with irregular boundaries. With the increase in jet speed, the eddy spacings become smaller and the induced velocity fields of the large structures tend to smear out the identity of individual vortices sooner.

In an axisymetric jet, these structures are clearly visible in low speed flows as in Fig. 3.2 (plate 2). However at high Reynolds number, they cannot be observed easily without resorting to special techniques such as forcing the jet or the flash schlieren technique as used by Moore (D3). However their existence can be inferred from the periodic velocity and static pressure fluctuation as observed outside the mixing layer (see Fig. 3.4) which, as we shall see later, are due to the induced fields of these structures that extend from the mixing regions of the jet into the non-entrained regions.

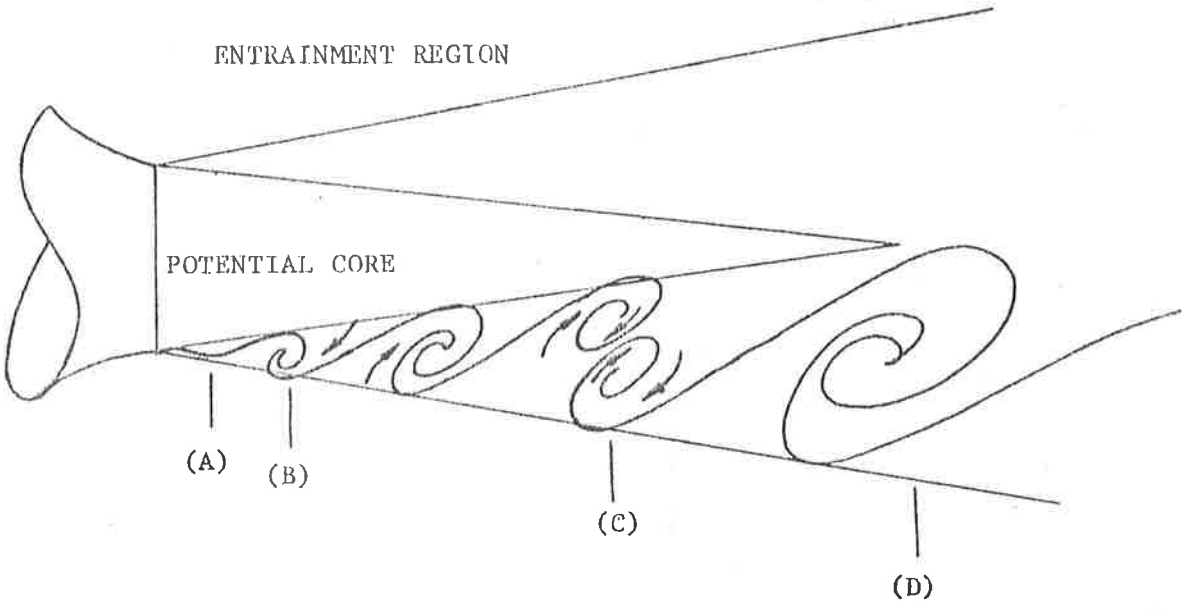

Fig. 3.3 Schematic diagram of a jet flow

Most of the flow visualization in this experiment was done on two-dimensional jets. The quantitative information on the spreading rates of the shear layer in the two-dimensional jets can be applied to the case of axisymetric jets. As pointed out by Morris (A18), who examined the effect of Mach number on the spreading and turbulence intensity of a model jet (50.8 mm or 2 inches diameter), the spreading rate of the annular mixing region of the jet agrees closely with that of a 2-D shear layer. Again, Bradshaw (E2) showed that the presence of a splitter plate on the axis of an axisymetric jet did not alter the jet structures. It is therefore believed that the development in the shear layer is dependent only on the initial boundary layer thickness at the nozzle exit. Hence in a 2-D jet, the two mixing layers should behave as independent 2-D mixing layers.

One can also argue analytically that at high Reynolds numbers the flow from an axisymmetric jet can be approximated by a 2-D mixing layer. From the stand point of the boundary layer theory the velocity component in the flow direction is large compared to the component normal to the flow direction. From the stand point of the instability of the jet boundary layer, the axial symmetry is not significant since the boundary layer thickness is small compared to the jet diameter. In this case the annular jet mixing layer can be replaced by a 2-D shear layer if the wavelength of the disturbance is small compared to the jet diameter.

From the above arguement, it is tempting therefore to assume that all turbulent mixing layers exhibit characteristics which are similar to those of a free 2-D mixing layer.

3.1.2 Near field pressure and velocity fluctuations

In a turbulent jet flow, the velocity and pressure signals in

the non-entrained regions of the jet are dominated by large positive or negative-going peaks. The periodic occurence of these peaks can be attributed to the passage of the large scale coherent motions within the mixing layer. The fluctuations, in relation to the large structures, can be further understood by the simultaneous flow measurements and optical observations.

Fig. 3.4 illustrates the simultaneous measurements of the velocity and static pressure fluctuations just outside the mixing layer at an axial distance of X/H = 3.0 downstream from a large aspect ratio (25:4) jet of velocity 10.5 m/s. The jet Reynolds number $U_J H/\nu$ is 7,000 and the probe positions are within the transition region of the jet based on the transitional Reynolds number $\frac{U_J X_T}{\nu} = 1.2 \times 10^5$ obtained in Yule's experiment (A11). In this region, the large scale structures are clearly visible as distinct vortices as shown in the sequential pictures in Fig. 3.4(b)(plate 3). The signals in Fig 3.4(b) are actually the first 16 mS of the signals in Fig. 3.4. The most striking feature of the velocity fluctuations in the potential core as shown in trace (A) of Fig. 3.4 is the periodic occurence of the large positive going peaks. The most probable interval between successive peaks is about 1.34 ms. Following the movie in Fig. 3.4(b) each positive peak corresponds to the passing of a large vortex. It is observed that the magnitude of the peaks appears to scale inversely with the distance between the probe and the vortex core. The deviation in the paths of the vortices therefore give rise to large and small peaks in the signal.

On the other hand, the velocity fluctuation in the entrainment region (trace (B) in Fig. 3.4 is significantly different from trace (A). The signal has rather broad and large negative going peaks with the most probable period of 3.3 ms between two successive

peaks. It is at first surprising that such a large difference in period should occur. On a closer examination of the movie film it becomes clear that the negative peaks in trace (B) are actually associated with the amalgamation process. It seems that a large peak is registered when two vortices are very close to each other, as is the case just before or during a pairing or an amalgamation at or near the point of measurement. Corresponding to the time a large negative peak is registered in trace (B), two successive peaks very close to each other are observed in trace (A). Usually the pair coincide with a small peak closely followed by a larger one as indicated by * in Fig. 3.4. This is the result of 'leap frogging' in the pairing process where a succeeding vortex attempts to overtake the preceeding one from the higher speed side of the shear layer and hence moves away from the probe. In doing so the vortices destroy each other's separate identities and finally merge to form a larger vortex.

It is interesting that Ko and Davies (A16) found a comparatively higher axial Strouhal number for the mixing layer and the potential core than indicated by measurement conducted in the entrainment region. It was incorrectly assumed by them that the measurement in the entrainment region was dominated by acoustic emission from the transition region, whose characteristic frequencies are of a lower order.

The causal relationship between the amalgamation processes and the peaks in the measured signals in the entrainment region of the jet is again demonstrated by the static pressure fluctuation (trace (C) in Fig. 3.4 where the large amplitude periodic fluctuation has superimposed on it small amplitude high frequency components. In trace (C) the condenser microphone inverts the signal and thus a positive peak actually represents a negative pressure difference.

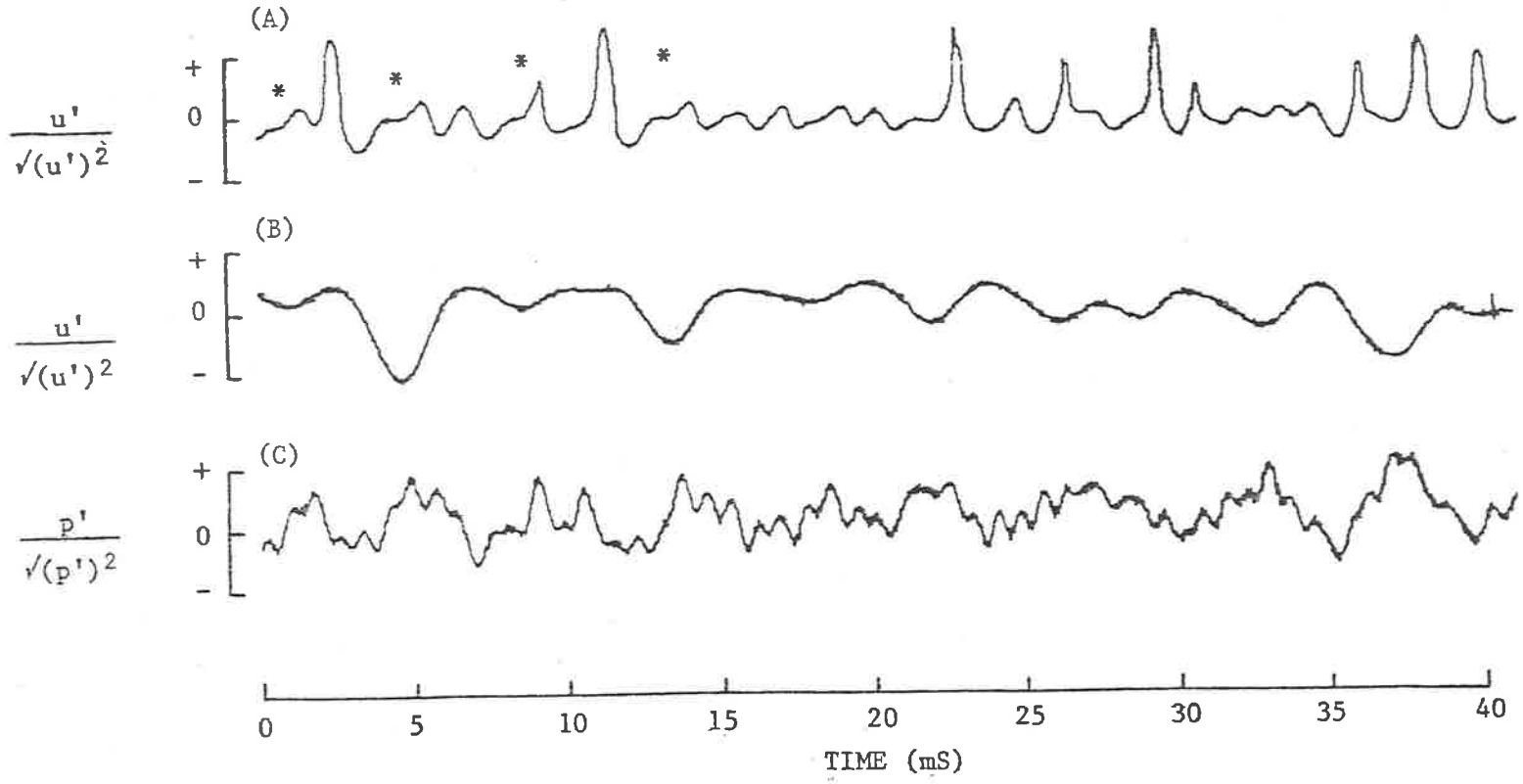

Fig. 3.4 Simultaneous velocity and pressure fluctuation in the unentrained region of a jet (U_J = 10.5 m/s)

(A) Hotwire X/H = 3.0, Y/H = 0.1
(B) Hotwire X/H = 3.0, Y/H = 1.5
(C) Pressure X/H = 3.0, Y/H = 1.5

Comparing traces (B) and (C), a large negative peak in trace (B) is immediately followed by a large distinctive peak in trace (C) suggesting that the static pressure fluctuations in the hydrodynamic near field of an incompressible mixing layer are induced by the velocity fluctuations inside the layer. The large pressure fluctuation process also suggests that it is probably an efficient noise generation mechanism.

The phase relationship between the induced velocity and pressure fields of the large structures in a jet mixing layer has been extensively mapped out by Lau et. al (A7). The intention of the experiment described here is to establish that these fluctuations are indeed the direct results of the large scale motion in the flow.

3.2 Some characteristics of the large structures in a turbulent jet

At high Reynolds number, statistical measurements have been used to provide quantitative information on the large structures in an axisymmetric jet. Space-time correlations were measured between two hot wires to estimate the spacing and convection speed of the structures.

The normalised cross-correlation coefficient $R_{AB}(\xi,\tau)$ between the signals A and B is defined by

$$R_{AB}(\xi,\tau) = \frac{\langle A\ (x,t)\ \ B\ (x+\xi,\ t+\tau)\rangle}{\bar{A}\ (x,t)\ \ \bar{B}\ (x+\xi,\ t+\tau)} \qquad (3.1)$$

where τ is the time delay, $\langle\ \rangle$ denotes the time average and an overbar denotes the R.M.S. value. Similarly, the normalized auto-correlation coefficient is defined by

$$R_{AA}(\tau) = \frac{\langle A\ (t)\ A\ (t+\tau)\rangle}{\bar{A}\ (t)\ \bar{A}\ (t+\tau)} \qquad (3.2)$$

3.2.1 The spacing of the large structures

The autocorrelations of the velocity fluctuations in both the potential core and the ambient region of a turbulent axisymmetric jet ($Re = 5.2 \times 10^5$) are measured at various axial locations between $1.0 < X/D < 5.0$ downstream from the nozzle exit. The normalised autocorrelations at $X/D = 4.0$ are shown in Fig. 3.5 where curve (A) is measured in the potential core and curve (B) in the entrainment region. The autocorrelations are rather periodic and the mean period T is defined by the time interval from zero to the first maximum. The mean period in the potential core T* is a better indication of the mean spacing of the structure since the signal in the ambient region is dominated by the amalgamation process. The mean eddy spacing ℓ_s, at the point of measurement, therefore scales as

$$\ell_s \sim U_c \, T^* \qquad (3.3)$$

where U_c is the average convection speed of the structures.

The linear variation of the mean periods in the velocity fluctuation with axial distance is illustrated in Fig. 3.6. In the initial mixing region of the jet the convection speed U_c is shown to be nearly constant (see Section 3.2.2) and following equation (3.3) the eddy spacing must increase with axial distance downstream. This increase in spacing and size of the structures is in fact achieved by the process of eddy amalgamation as seen in the shadowgraphs and high speed movies of the flow.

As seen in Section 3.1.2, the induced velocity fluctuations in the entrainment region are dominated by the amalgamation processes. Thus the mean period in the autocorrelation function is an indication

of how frequently amalgamation processes occur at the point of measurement and is not the vortex passing frequency. Thus at any

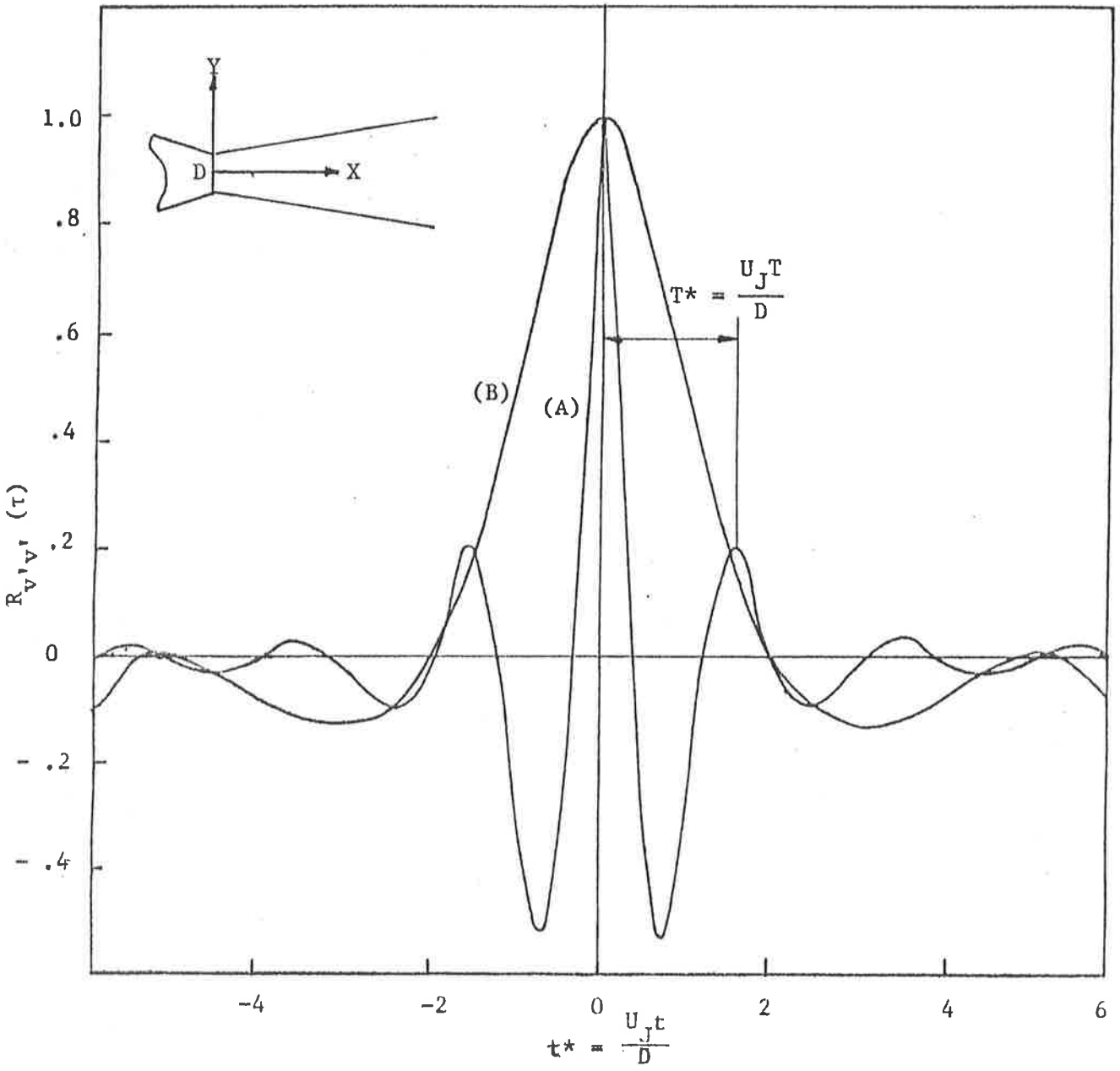

Fig. 3.5 Autocorrelation function of the velocity fluctuation in a turbulent jet.

($Re = \frac{U_J D}{\nu} = 5.2 \times 10^5$; (A) X/D = 4.0, Y/D = 0.0;

(B) X/D = 4.0, Y/D = 1.60)

axial location a longer mean period in the autocorrelation function is obtained in the entrainment region compared with the mean period measured in the potential core, as shown in Fig. 3.5 and Fig. 3.6.

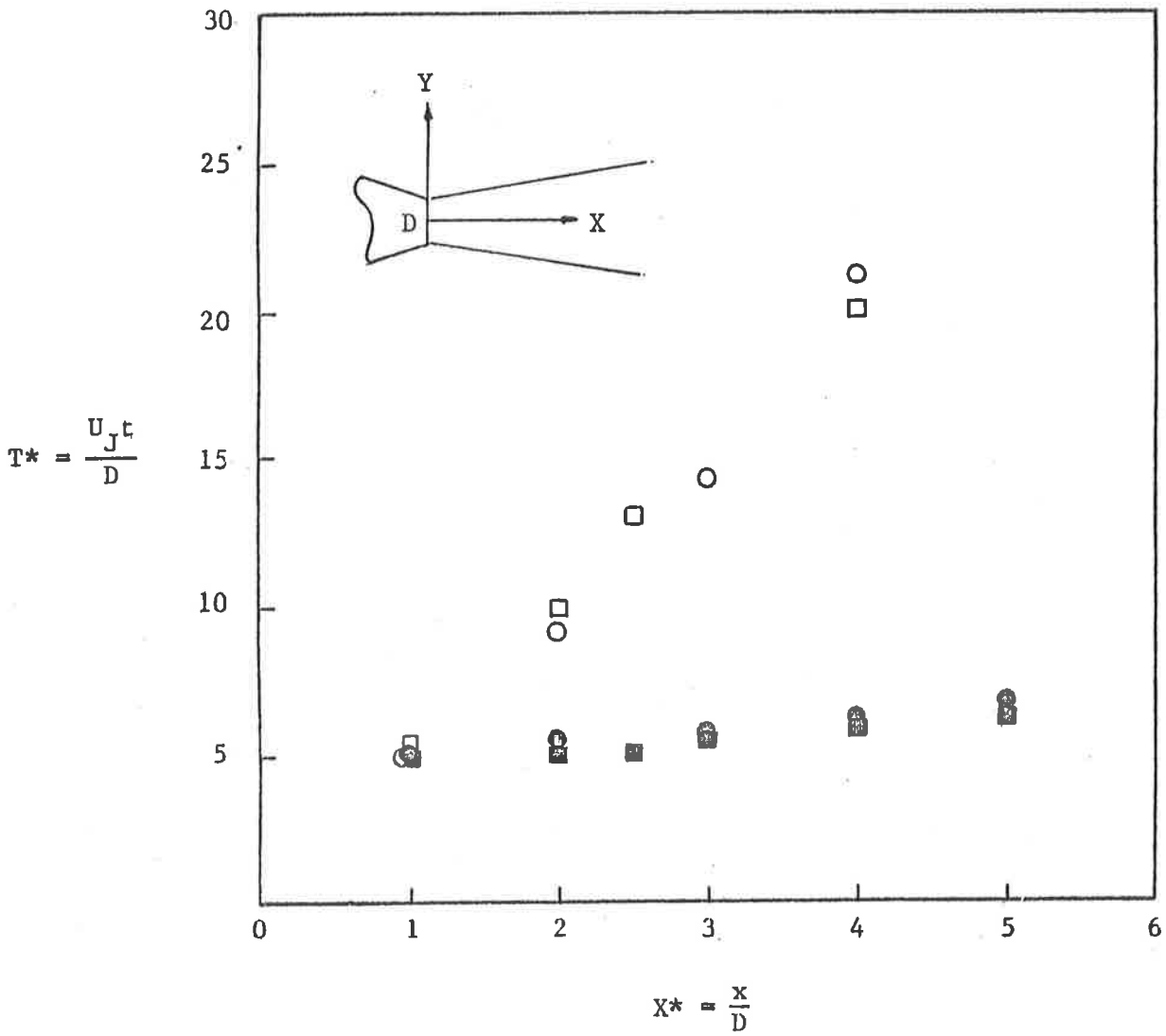

Fig. 3.6 Mean period of the velocity fluctuation in a turbulent jet

○ — air jet (U_J = 167.0 m/s, Re = $\frac{UD}{\nu}$ = 3.3 x 10^5)

□ — CO_2 jet (U_J = 149.5 m/s, Re = $\frac{UD}{\nu}$ = 5.2 x 10^5)

closed symbols (in potential core)
open symbols (in the entrainment region)

3.2.2. The convection velocity of the large structure

The convection speed of the large structure is a significant component in jet noise problems in that

(1) it enhances the downstream radiation and hence influences the directivity pattern;

(2) in a stationary frame of reference, the sources in motion lead to a doppler shift in measured frequencies;

(3) apart from mixing noise, intense Mach waves are radiated when the speed of the source becomes supersonic relative to the speed of sound in the ambient acoustic medium, as can be seen in Fig. 3.16 and Fig. 3.17 (plate 9).

The convection of the flow pattern can be seen from the simultaneous velocity fluctuations at different axial locations of a 25.4 mm (1 in) diameter jet as shown in Fig. 3.7. The hot wires are separated by a distance $\Delta X/D = 0.6$ with the first wire at $X/D = 2.4$. The changing velocity signals with axial distance is a good indication that the flow is not frozen but is varying, in agreement with the flow visualization experiments. The disappearance of some peaks in the hot wire signal further downstream is clearly the result of the amalgamation processes as the vortices convect downstream.

The convection speed of the structure is measured by the space-time cross-correlation of the velocity fluctuations of two hot wires displaced axially by a distance ΔX and is defined as

$$U_c = \frac{\Delta X}{\Delta \tau} \quad ,$$

where $\Delta \tau$ is the time delay of the most significant peak in the

cross-correlation function. The correlation technique involves integration over a long time and therefore gives rise to an average convection speed.

The space-time crosscorrelation for the unfiltered velocity signals in the entrainment region of a round jet is shown in Fig. 3.8. The number on each curve represents the downstream hot wire separation $\Delta X/D$ relative to the reference hot wire. In this case the hot wires are located in the entrainment region of the jet and the convection speed U_c obtained is 0.41 U_J. Similar

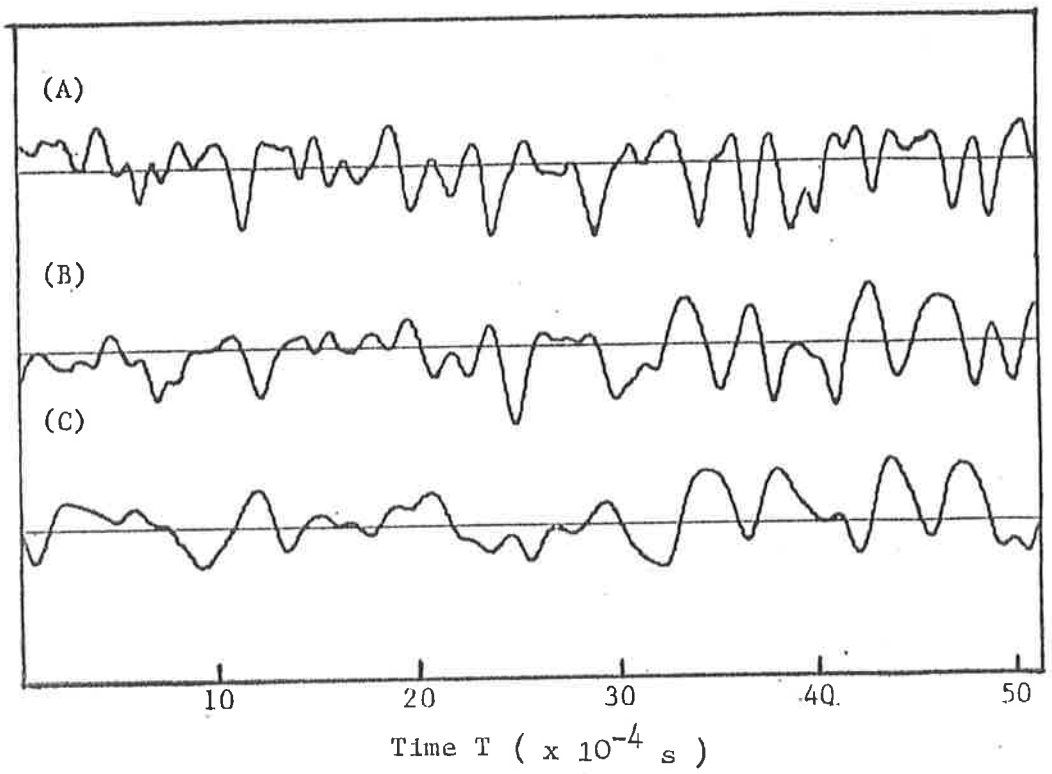

Fig. 3.7 Simultaneous hot wire measurements in the entrainment region of a jet.

(U_J = 40 m/s, Re = $\frac{UD}{\nu}$ = 6.47 x 10^4; (A) X/D = 2.4;

(B) X/D = 3.0; X/D = 3.6)

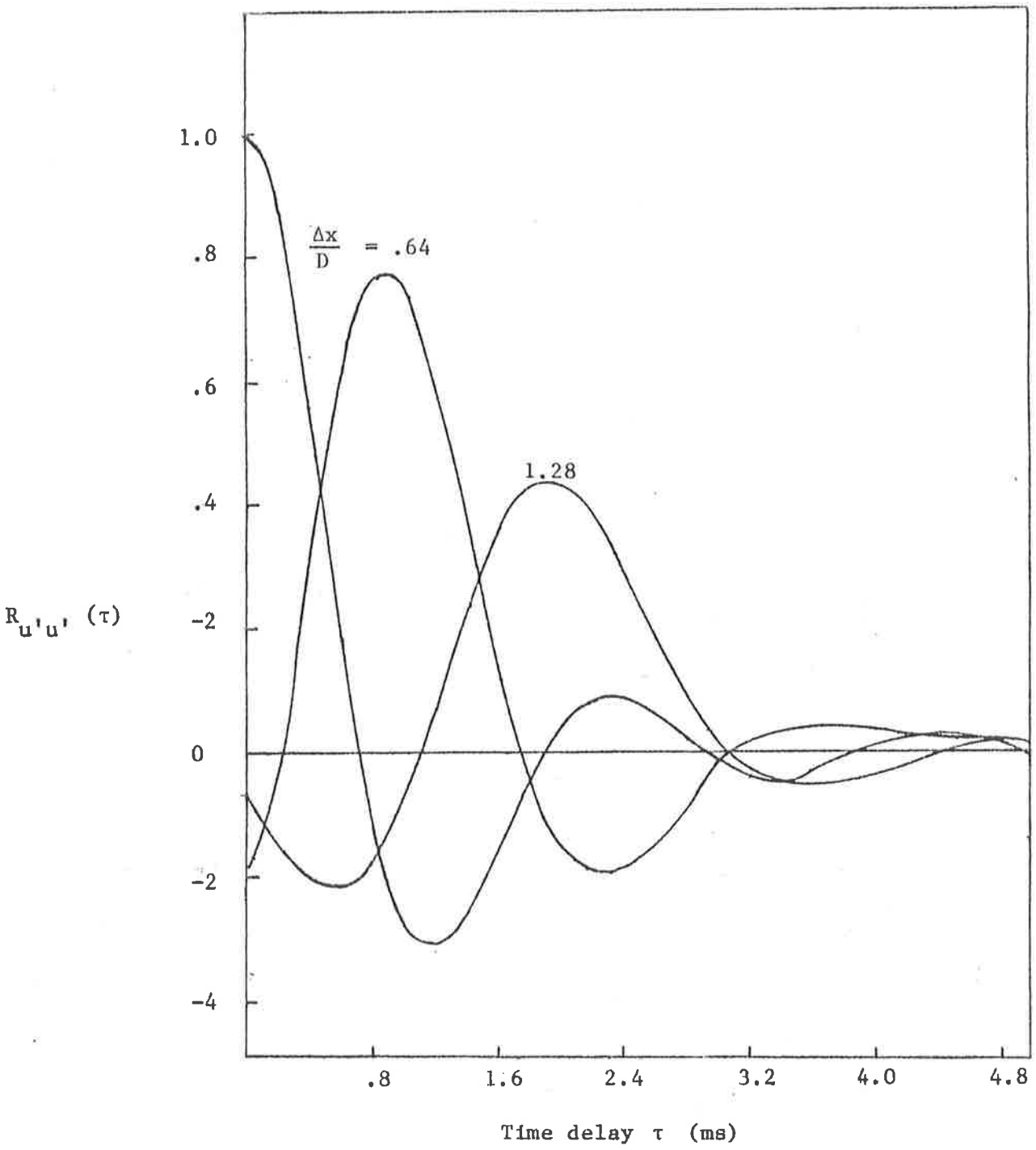

Fig. 3.8 Space-time cross correlation of the unfiltered velocity fluctuations in the entrainment region of a jet.
($U_J \simeq 40$ m/s, Re = 6.47×10^4 fixed wire at X/D = 2.4)

measurements in the same axial locations in the potential core resulted in $U_c/U_J = 0.73$. Other investigators have reported similar variation in the measured convection speed at different radial locations of a jet. Davies, Fisher and Barrett (A9) found that at X/D = 1.5, $U_c/U_J = 0.6$ in the shear layer and $U_c/U_J = 0.7$ in the potential core. Seiner (A20) at the location X/D = 4.0 obtained values of U_c/U_J of 0.55 and 0.82 in the shear layer and in the potential core respectively. It therefore appears that there is no unique convection speed across the shear layer. The possible explanation for the variation of convection speed with radial position is the high shear stress in the layer which distorts the structures into an elliptical shape as they convect downstream as observed optically. The distortion seems to be symmetrical about the core of the structure and the difference in convection speed on either side of the shear layer is the deformation rate of the large structure. The convection velocity of the vortex core along the lip line of the jet is therefore a logical choice for the average convection speed. This value is the mean of the measured convection velocities on either side of the shear layer.

The mean convection speed is plotted in Fig. 3.9 as a function of axial position together with the data of other investigators. The turbulent convection speed in the initial region of the jet (X/D < 5.0) is found to be nearly constant. For a constant density jet, this value is roughly 0.57 U_J compared to the normally accepted values of $(0.63 \rightarrow 0.67)U_J$. The ratio U_c/U_J does however depend strongly on the density ratio (ρ_J/ρ_o) as we shall see in Section 3.3.3.

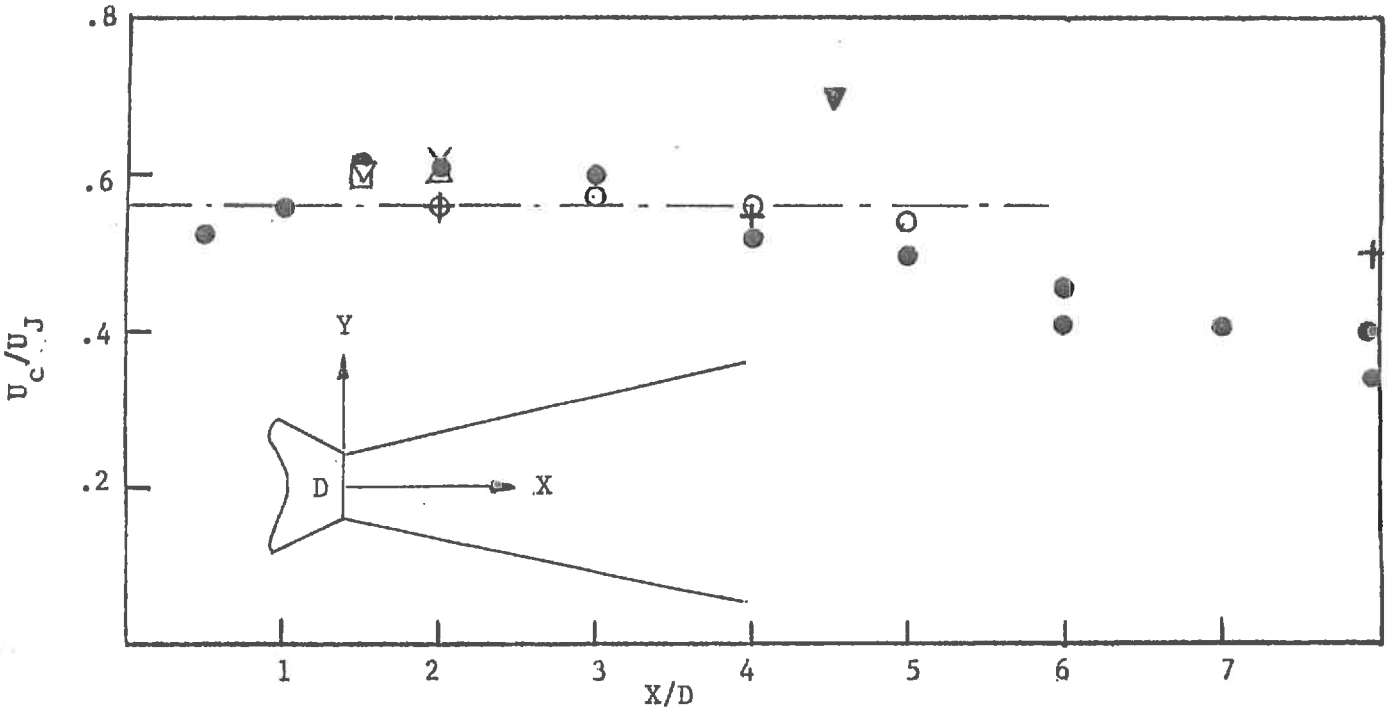

Fig. 3.9 Mean convection speed in the mixing region of a turbulent jet (ρ_j/ρ_o = 1.0, Y/D = 0.5)

- o - present data
- □ - Ko & Davies [A16]
- △ - Bradshaw, Ferris and Johnson [A19]
- ▽ - Davies, Fisher and Barrett [A9]
- × - Lau and Fisher [A7]
- ● - Peterson [A14]
- \+ - Seiner [A20]

3.3 Effects of density and velocity on turbulent jet flow

3.3.1 Flow convection speed and average density from the mixing layer model

From the entrainment measurement and measurement of the convection speed of the large structure, Brown (A2) proposed a simple model to estimate the dependence of density and velocity ratio across the layer on the relative entrainment rate, the spreading rate of the layer and the convection speed of the larger structure.

By a Galilean transformation $x = U_c\ t$ where U_c is the average convection speed of the large structures the mixing layer is modelled as an 'equivalent' temporal problem. Then by dimensional analysis further guided by experimental results the predictions of the model can be derived (see appendix for detail analysis) which are summarised as follows :

$$\lambda_1 + \lambda_2 = 0.178\ (1 - r) \tag{3.4}$$

$$\lambda_1/\lambda_2 = 1/K(s) \tag{3.5}$$

$$\delta' = 0.178\ \frac{(1 + K(s))\,(1 - r)}{K(s) + r} \tag{3.6}$$

$$U_c/U_1 = \frac{K(s) + r}{1 + K(s)} \tag{3.7}$$

$$\rho_m/\rho_2 = \frac{1/s + K(s)}{1 + K(s)}\ , \tag{3.8}$$

where $\lambda_i = \frac{V_{ei}}{U_1}$ and V_{ei} is the entrainment velocity of the ambient fluid i, r is the velocity ratio U_2/U_1, s is the density ratio ρ_2/ρ_1, $K(s) = 1/s^{0.6}$, δ' is the spreading rate of the mixing layer, U_c is the convection speed of the structure and ρ_m is the average density in the mixing layer.

The results are valid for incompressible flows and they are used as a guide and comparison to the present jet mixing layer experiments.

3.3.2 Velocity and density dependence of shear layer spreading rate

The one-shot shadowgraphs of a 2-D jet for a range of velocity and density are shown in plate 4 - 8. Estimations of the spreading rate of the mixing layer are obtained by drawing straight line mean tangent to the 'edge' of the mixing layer as shown in Fig. 3.3 . The visual thickness δ'_{vis} is

$$\delta'_{vis} = \frac{\Delta\delta_{vis}}{\Delta x}\ , \tag{3.9}$$

where x is the distance in the axial direction.

As discussed in Section 3.1.1, the growth rate of a 2 - D mixing layer has been found by Morris (A18) to be in good agreement with that of an axisymmetric jet flow and similarly the results from

a 2-D jet flow can be applied to an axisymmetric jet. From the shadowgraphs, the velocity dependence of the mixing layer growth rate of a jet of fixed density is shown in Fig. 3.18. The mixing layer thickness at subsonic velocities is obtained from the 2 - D jet following the criterion described above. For the flow from a round convergent - divergent nozzle, the thickness is approximated by twice the thickness from the lip line to the outer 'edge' of the flow. This measurement could be over estimated as the outer edge of the mixing layer in a 2-D flow is seen to diverge from the lip line more than the inner edge. At any rate, significant thinning of the layer is observed. This thinning evidently is a result of the compressibility effect connected with Mach number since the free streams density ratio is nearly constant. This compressibility effect is also observed at high subsonic speed as shown in Fig. 3.18. At low to medium subsonic speed the growth rate is only weakly dependent on the jet velocity.

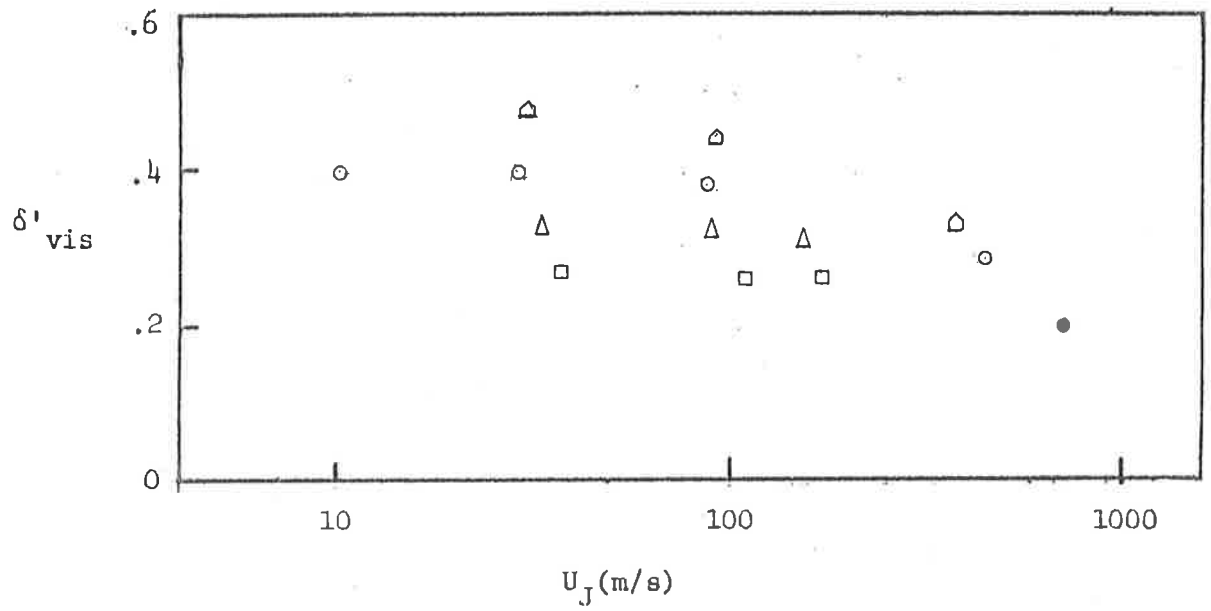

Fig. 3.18 Velocity dependence of the visual shear layer growth rate

(□, ρ_J/ρ_o=2.5 ; Δ,1.5 ; o,0.6 ; ⌂,0.17)

(Closed symbols for convergent-divergent nozzles and open symbols for convergent nozzles)

The density dependence of the visual mixing layer growth rate is compared with Brown's model and other available published data in Fig. 3.19. For jet density ratios greater than unity the measurements for the 2-D jet agree well with Brown's mixing layer model but the discrepancy increases when $\rho_j/\rho_o < 1.0$. From Fig 3.14 and Fig. 3.15, it can be seen that for a light jet, especially at low velocity, the definition of the edges of the shear layers is rather poor. The ranges of the possible interpretations of δ'_{vis} from the shadowgraphs are displayed as error bars in Fig. 3.19. For consistency the most conservative spreading rate was used in all cases which could therefore partially account for the discrepancy.

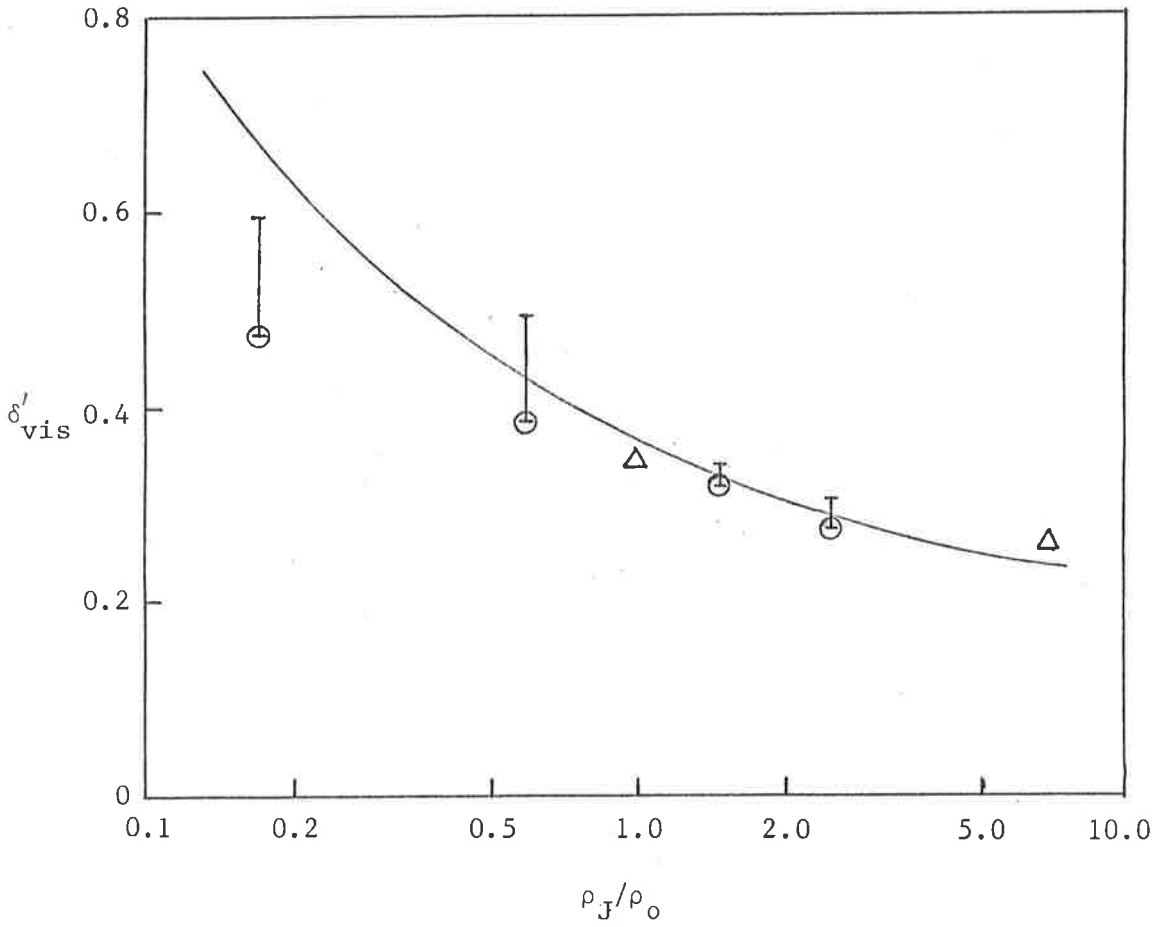

Fig. 3.19 Density dependence of the visual shear layer growth rate for subsonic jets. (o,measured data; —,Brown & Roshko shear layer model where $K(s)=1/s^{.6}$; Δ,Brown [A2]; I,error bars)

3.3.3 Density dependence of the flow convection velocity

The measured flow convection speed in the initial mixing region of a jet is shown in Fig. 3.20 as a function of density ratio. As discussed in Section 3.2.2., the measured convection speed varies with radial location of the jet. The average speed in this case is obtained by taking the mean of the two measured convection speeds, as defined by equation (3.4), in the potential core and the entrainment region. This is found to be close to the measurements obtained at the jet lip line as in Fig. 3.20. For the same jet exit velocity, the convection speed in a dense jet is found to be higher than in a light jet. It varies from 0.38 - 0.72 U_J for ρ_J/ρ_o in the range 0.17 -0.72. This is consistent with equation (3.6) of the 2-D mixing layer model. In Fig. 3.20 the mean convection speed in the jet is found to be slightly higher than that predicted by the model. However, they do exhibit similar trends in their density dependence.

Using the values obtained in Fig. 3.19 and Fig. 3.20, the values of $\delta'_{vis} \frac{U_c}{U_J}$ are tabulated for jets of various density ratios for $U_J/a_o < 1.0$.

ρ_J/ρ_o	0.2	1.0	1.5	2.5
$\delta'_{vis}\ U_c/U_J$	0.186	0.199	0.203	0.189

The result show that $\delta'_{vis} \frac{U_c}{U_J}$ is roughly constant with an average value of 0.194 over the density range. This is consistent with the mixing layer model where for $U_2 = 0$ ($r = U_2/U_1 = 0$), equation (3.6) and equation (3.7) become

$$\delta' = 0.178 \frac{1 + K(s)}{K(s)} ,$$

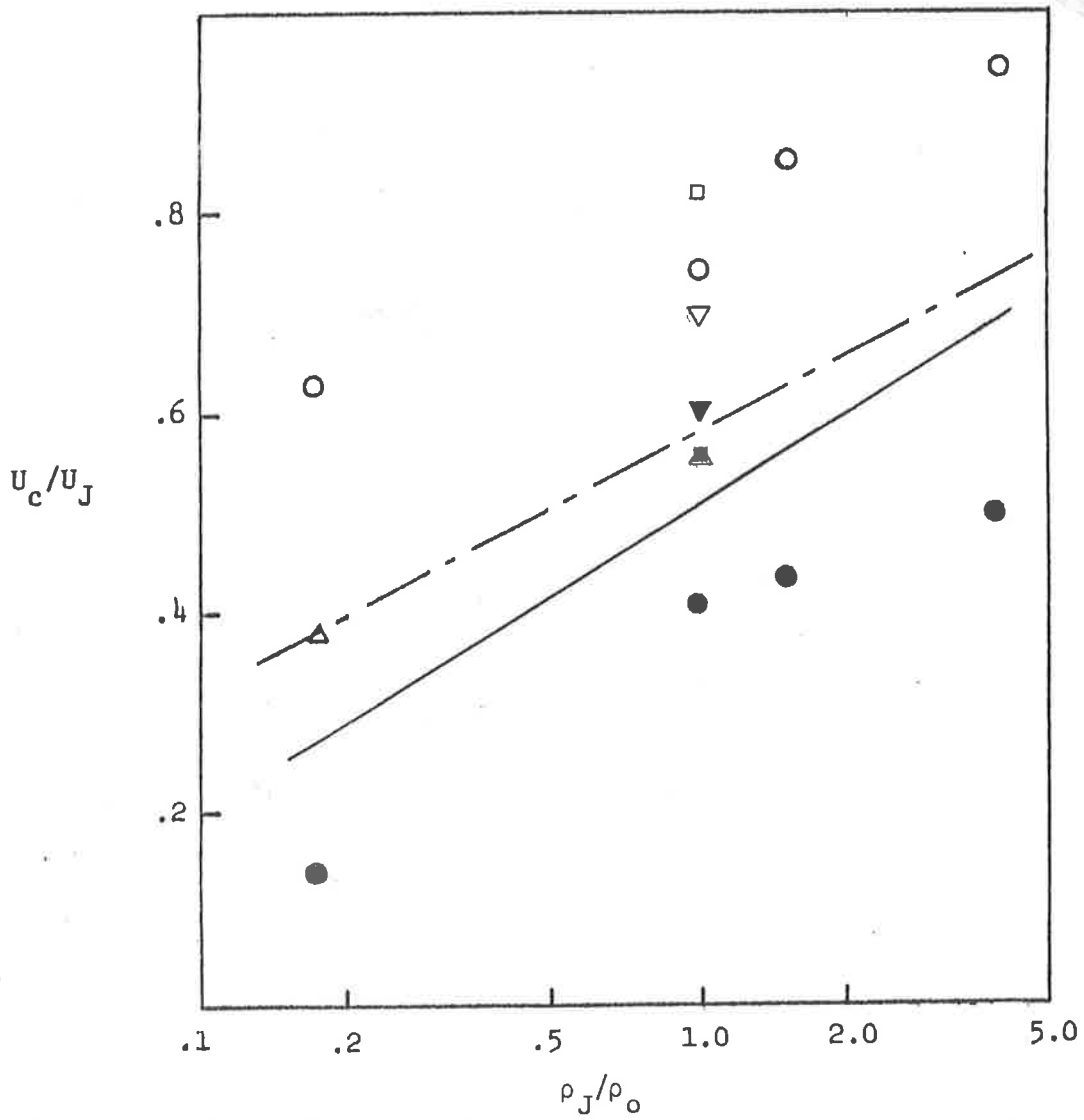

Fig. 3.20 Density dependence of the flow convection speed

● - measurement in the entrainment region

○ - measurement in the potential core

△ - measurement in the lip line

—·— - mean value between the potential core and entrainment region measurement

——— - Brown's model

□ -Seiner (A20); (X/D = 4.0, closed symbol for measurement in shear layer and open symbol for measurement in potential core)

▽ -Davies, Fisher and Barrett (A9); (X/D = 1.5, closed symbol for measurement in shear layer and open symbol for measurement in potential core)

$$U_c/U_1 = \frac{K(s)}{1 + K(s)}$$

and clearly $\delta' \frac{U_c}{U_1} = 0.178$.

Thus for a fixed U_J, $\Delta\delta/\Delta t$ is a constant since $\delta'_{vis} = \frac{\Delta\delta_{vis}}{\Delta x}$ and $U_c = \frac{\Delta x}{\Delta t}$ and $\Delta\delta_{vis}/\Delta t$ is the total entrainment rate which is concluded by Brown (A2) to be dependent only on the velocity ratio. The higher shear layer growth rate observed in jets where the density is low is in fact a result of the slower flow convection velocity in the layer and is not a result of higher entrainment rate.

3.4 Correlation of the turbulent flow dynamics with sound production

Attempts to establish a more definitive understanding of the relation between turbulent flow dynamics and the sound production are frequently deduced from the statistical interdependence of the velocity or pressure fluctuations and the radiated noise as indicated by 2-point space-time cross-correlations. The hot wire-microphone system used by Lee & Ribner (D23) showed a poor normalised cross-correlation coefficient of only 1 - 2%. Meecham and Hurdle (D24), who inserted a microphone with a noise cone in the turbulent flow region of a jet, cross-correlated the near field static pressure fluctuation with the far field and obtained values varying from 0.4% to 15.5%. They hence concluded from the result that the main sources of noise were confined to a cylindrical volume centred around the jet axis with a diameter roughly that of the jet diameter. However, as pointed out by Siddon and Hogland (D25)

the magnitude of the noise produced by the probe embedded in the turbulent flow casts doubt on the validity of such correlation measurements.

The physical presence of the probe in the flow could also affect the flow itself. In the present investigation the near field measurement is made in the ambient fluid adjacent to the entrainment region so that only the induced velocity and pressure fluctuation of the large scale structures are monitored. By this method probe-flow interaction is kept to a minimum and the measured signals are not masked by the fine scale turbulence in the mixing layer.

In this experiment, for an axisymmetric jet the normalised cross-correlation obtained from the unfiltered signals is typically of the order of 2 - 4%. A correlation function of this magnitude provides no conclusive evidence of any relationship between the large scale structure and the noise. This result is to be expected since the noise in a jet comes from an extensive region of the flow and the near field measured only a small part of that flow.

The correlation of near-field pressure signals from two circumferentially deployed microphones by Fuchs (D18) showed a monotonic fall of the correlation coefficient with increasing microphone displacement. For the present work it was reasoned that the 2 - D mixing in which the pressure and velocity are more in phase in the spanwise direction should give rise to a higher value of measured cross-correlation coefficient. A ground plane of length equal to 5H was therefore installed in the place of one of the lip lines of a 2 - D jet (aspect ratio L/H = 25/4; H = 1.0 cm) as illustrated in Fig. 3.21.

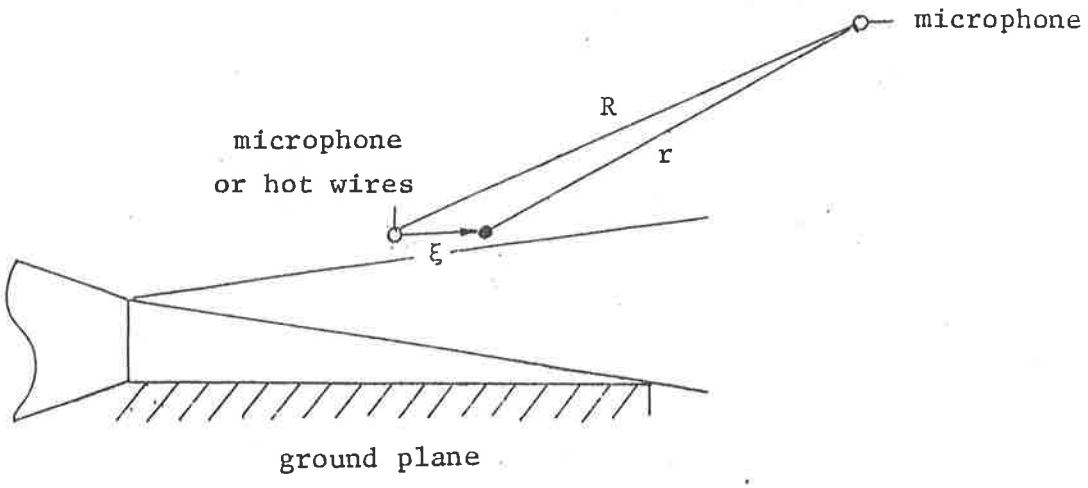

Fig. 3.21 Schematic of 2-D nozzle, ground plane arrangement and probe positions.

In the direct correlation measurement the far field microphone was located at the acoustic emission angle $\theta = 45^{\circ}$ to the jet axis and at a distance of either 0.5 m or 0.75 m from the exit. The near field probe (microphone or hot wires) was placed just outside the top mixing layer the origin of which is at the nozzle lip. In each case a large distinctive peak was observed at a time delay roughly equal to acoustic transmission time of R/a_o where R is the probe separation. In cases (A) and (B) in Fig. 3.22 the measured values were 2.28 ms and 1.56 ms respectively compared to the values of 2.08 ms and 1.37 ms based on causality. As observed in Section 3.1.2., the near field velocity or pressure signal is dominated by the large scale motion in the vicinity of the probe. When the velocity signals from 2 probes separated by a distance ξ on the x direction were crosscorrelated a peak at a time delay $\tau_m = \xi/U_c$ would be obtained. Thus the measured peak correlation between the near field velocity fluctuation and the far field noise should occur at a time delay τ_m given by

$$\tau_m = r/a + \xi/U_c$$

where positive ξ means the dominant source is downstream from the near field probe. The higher measured values indicate that the source is located at about 1.5 H downstream of the probe or at X/H = 4.5. In Fig. 3.23 where the direct correlation of the static pressure fluctuation of the flow and the acoustic field were measured slightly higher values of 2.37 ms and 1.66 ms were obtained. The difference in the measured peak time delay between the pressure-velocity and the pressure-pressure correlations is seen in Section 3.1.2 to be related to the microphone signal lagging the hot wire signal in the entrainemnt region.

Shortly after the above experiment was completed, Yu and Tam (D17) published an investigation of trailing edge noise. Their set up was rather similar to that described above except that the trailing edge was located at 8.5 times the nozzle height downstream. They also found that the peak correlation corresponds to causality and was located close to the trailing edge of the plate. They concluded that the interaction of the convecting large structures with the trailing edge was dominant in determining the correlation between the near field and the far field. However, it is known that turbulence located near a sharp edge can provide a powerful source of noise radiation, as the analysis of Crighton (B5) has shown. The high correlation obtained in this experiment certainly derives from the large scale motion in the shear layer either directly, which the experiment was designed to demonstrate, or indirectly via the generation of noise from the trailing edge of the plate. Further experiments are necessary to resolve the matter.

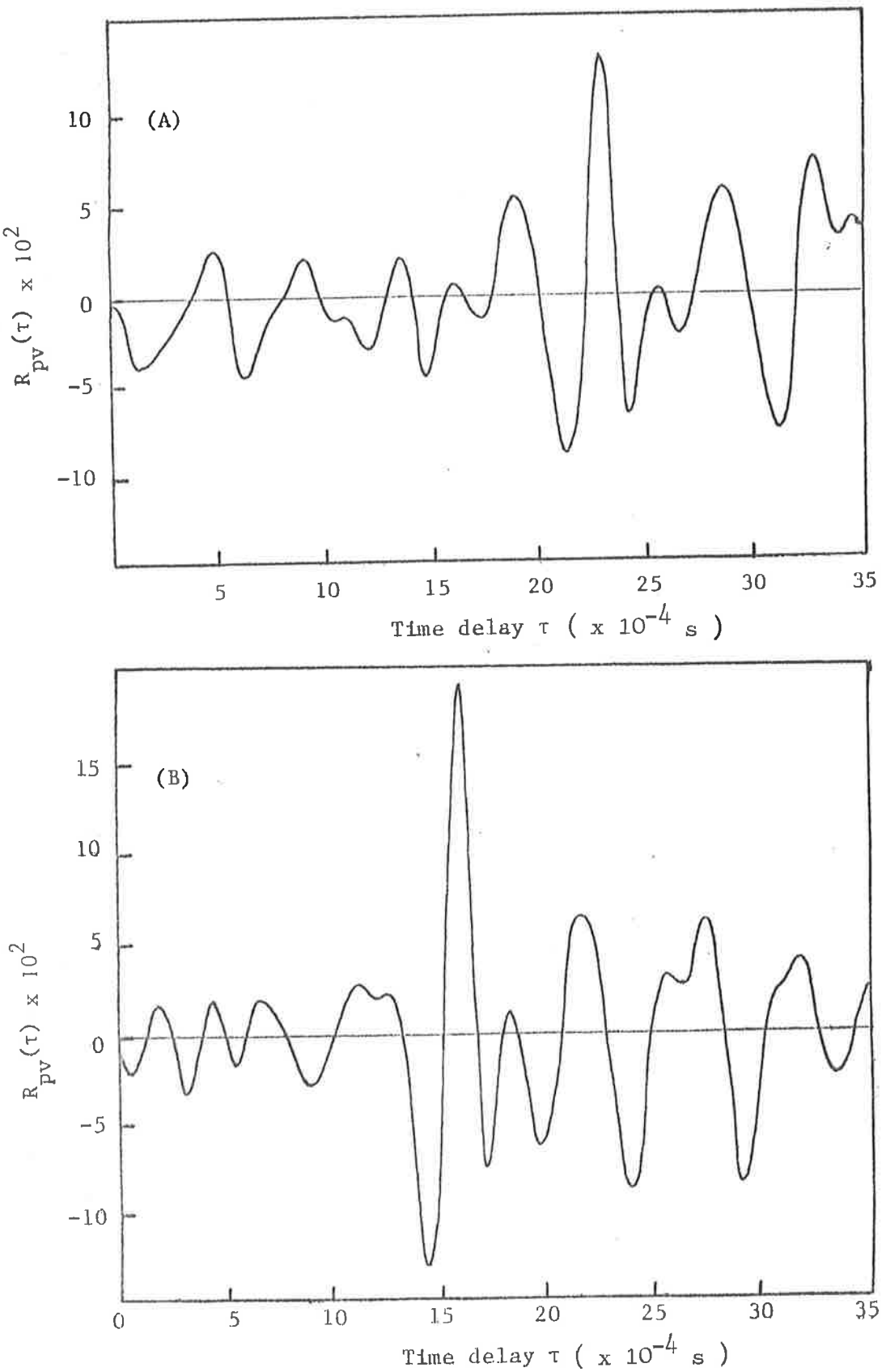

Fig. 3.22 Cross-correlation of near field velocity fluctuation with the acoustic far field.

(A) $x_{hw}/H = 3$, $R/D = 74$, $\theta = 45^{o}$

(B) $x_{hw}/H = 3$, $R/D = 51$, $\theta = 45^{o}$

($Re = \frac{U_J D}{\nu} = 1.0 \times 10^5$)

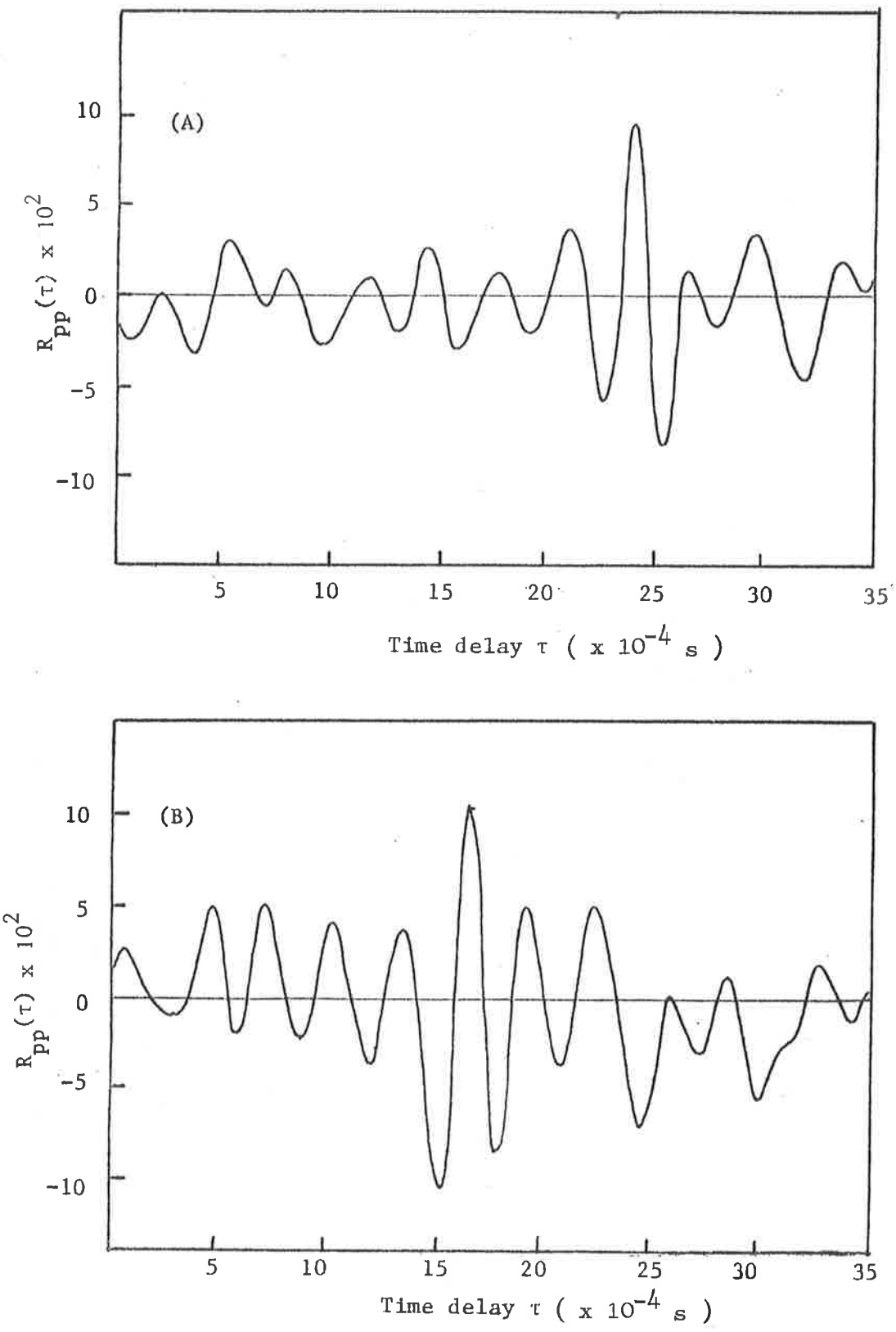

Fig. 3.23 Cross-correlation of near field hydrodynamic pressure fluctuation with the far acoustic field

(A) $X_{mic}/H = 3$, $R/D = 74$, $\theta = 45^{o}$

(B) $X_{mic}/H = 3$, $R/D = 51$, $\theta = 45^{o}$

($Re = \frac{U_J D}{\nu} = 1.02 \times 10^5$)

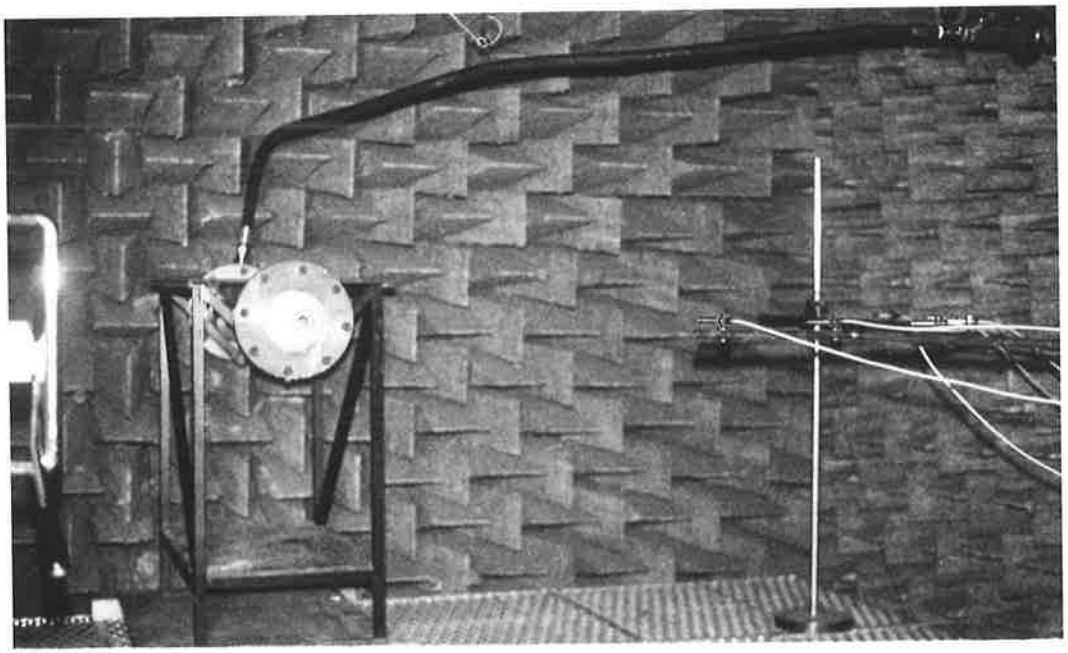

Fig. 2.6 The layout in the anechoic chamber.

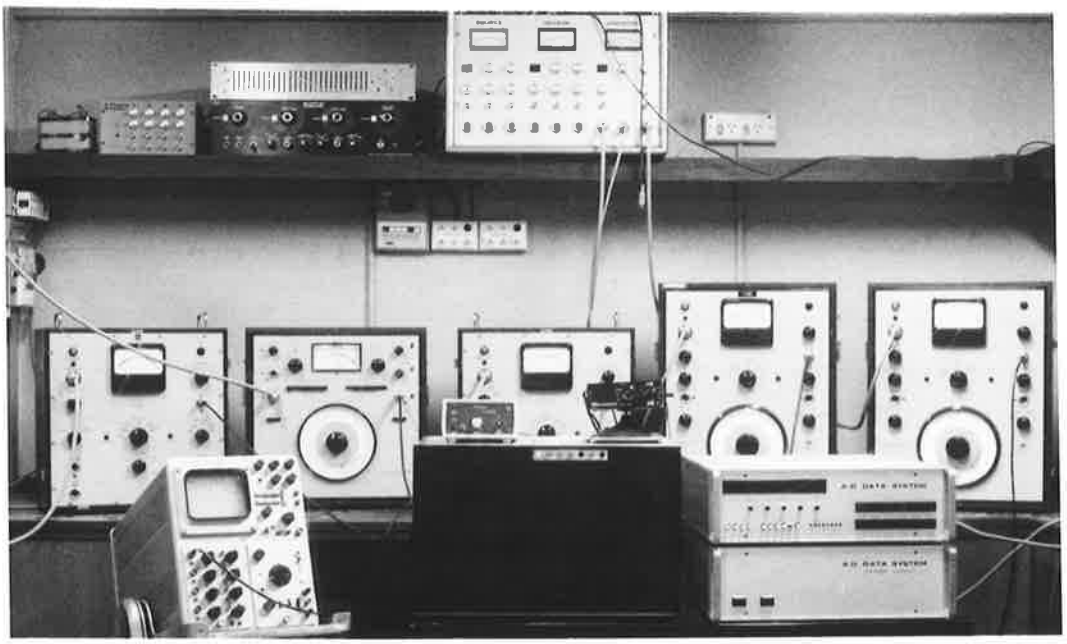

Fig. 2.7 The acoustic and recording instrumentation.

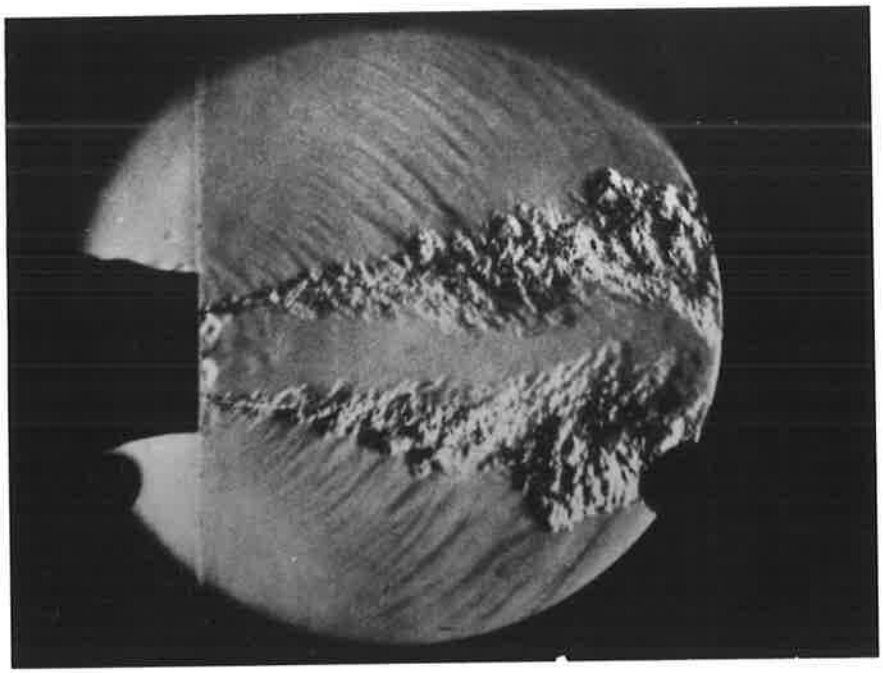

Fig. 3.1 Schlienren picture of a 2-D helium jet.

(U_J = 834 m/s, Re = 1.93 x 10^5)

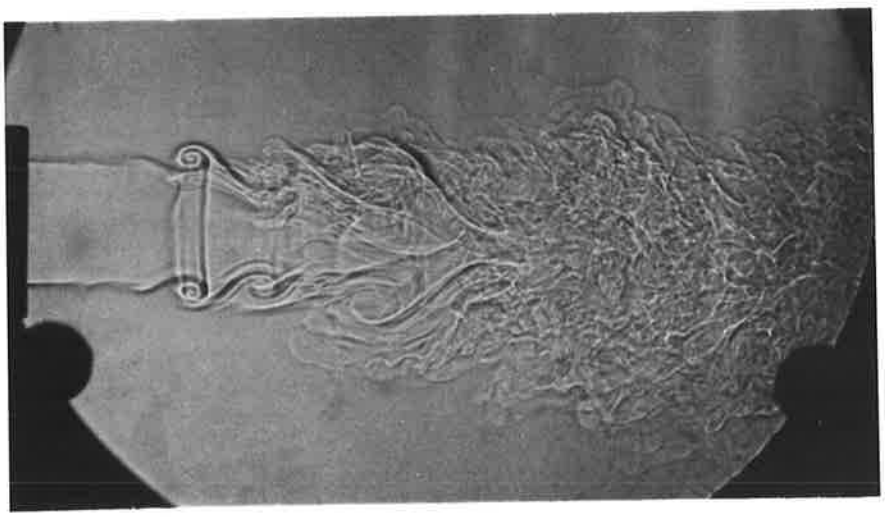

Fig. 3.2 Shadowgraph of an axismmetric jet at low Reynolds number

(U_J = 3 m/s, Re = 5.8 x 10^3)

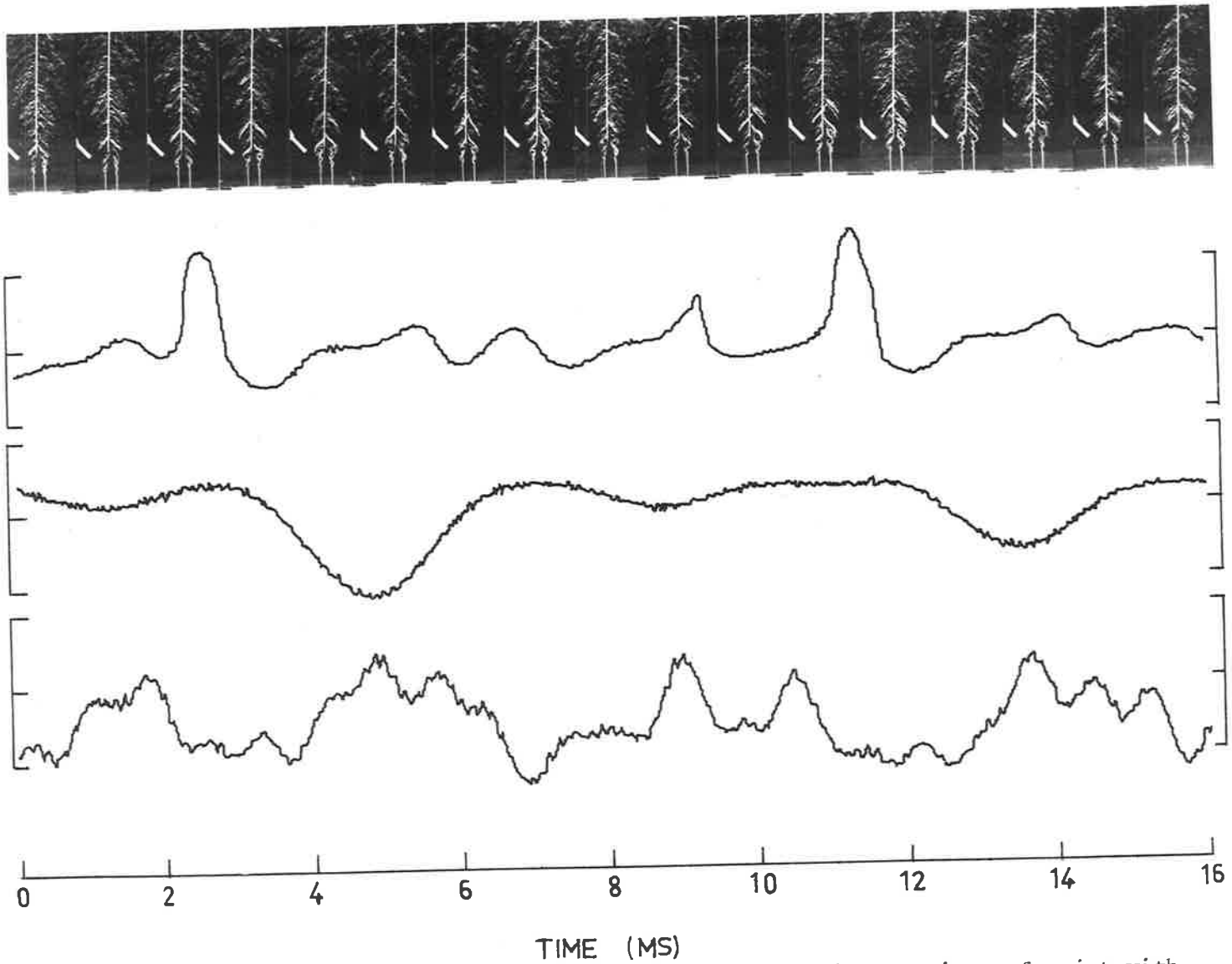

Fig. 3.4(b) Velocity and pressure fluctuation in the unentrained regions of a jet with synchronised visual recording. (U_J = 10 m/s, Re = 1.2 x 10^4)

(Plate 3)

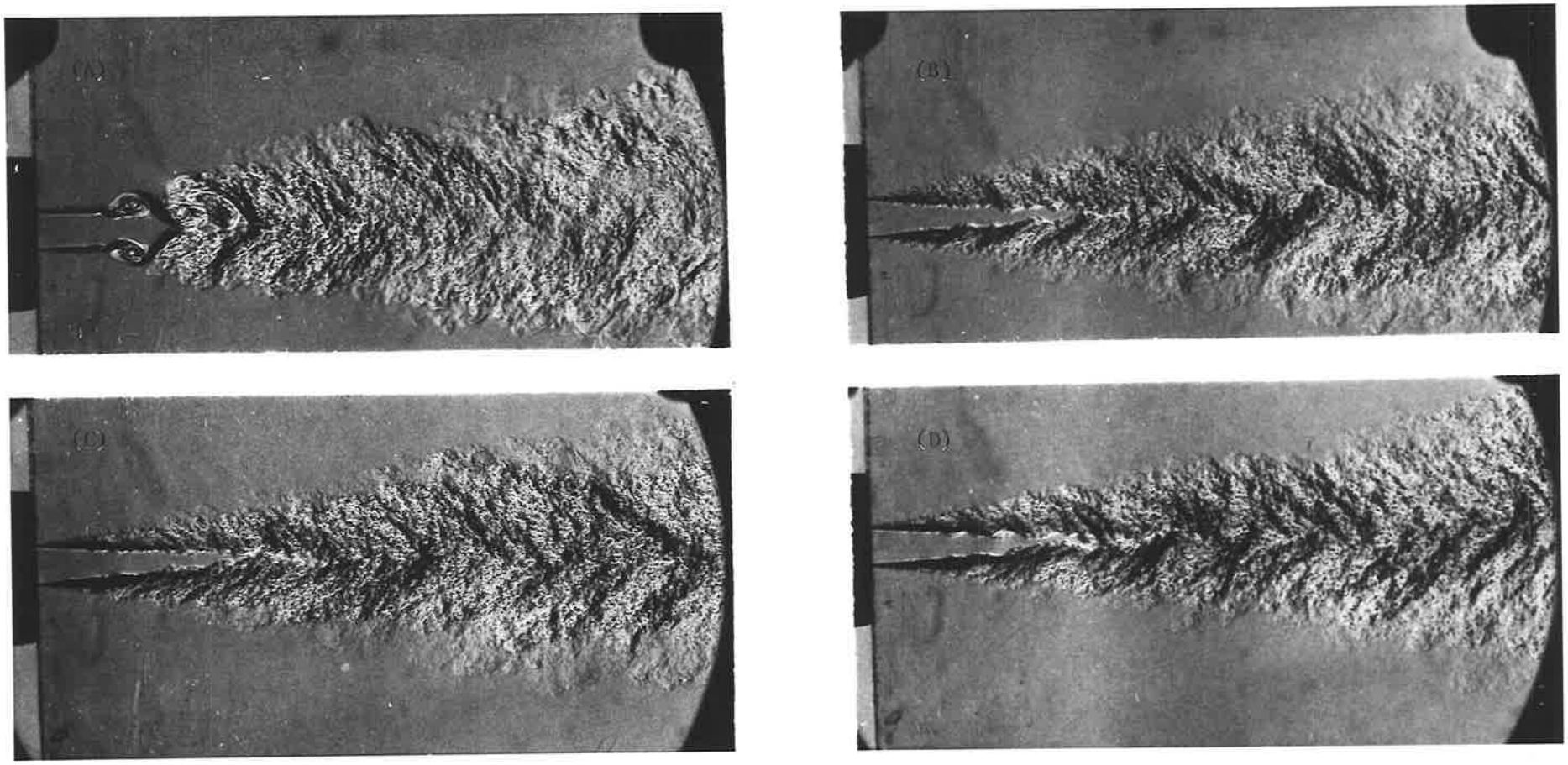

(plate 4)

Fig. 3.11 Shadowgraphs of a two-dimensional jet flow
(ρ_J/ρ_o = 2.5, ν = 3.8 x 10^{-6}, Re = $\frac{UD}{\nu}$; (A) 1.3 x 10^4 ; (B) 5.0 x 10^4 ; (C) 1.5 x 10^5; (D) 2.3 x 10^5)

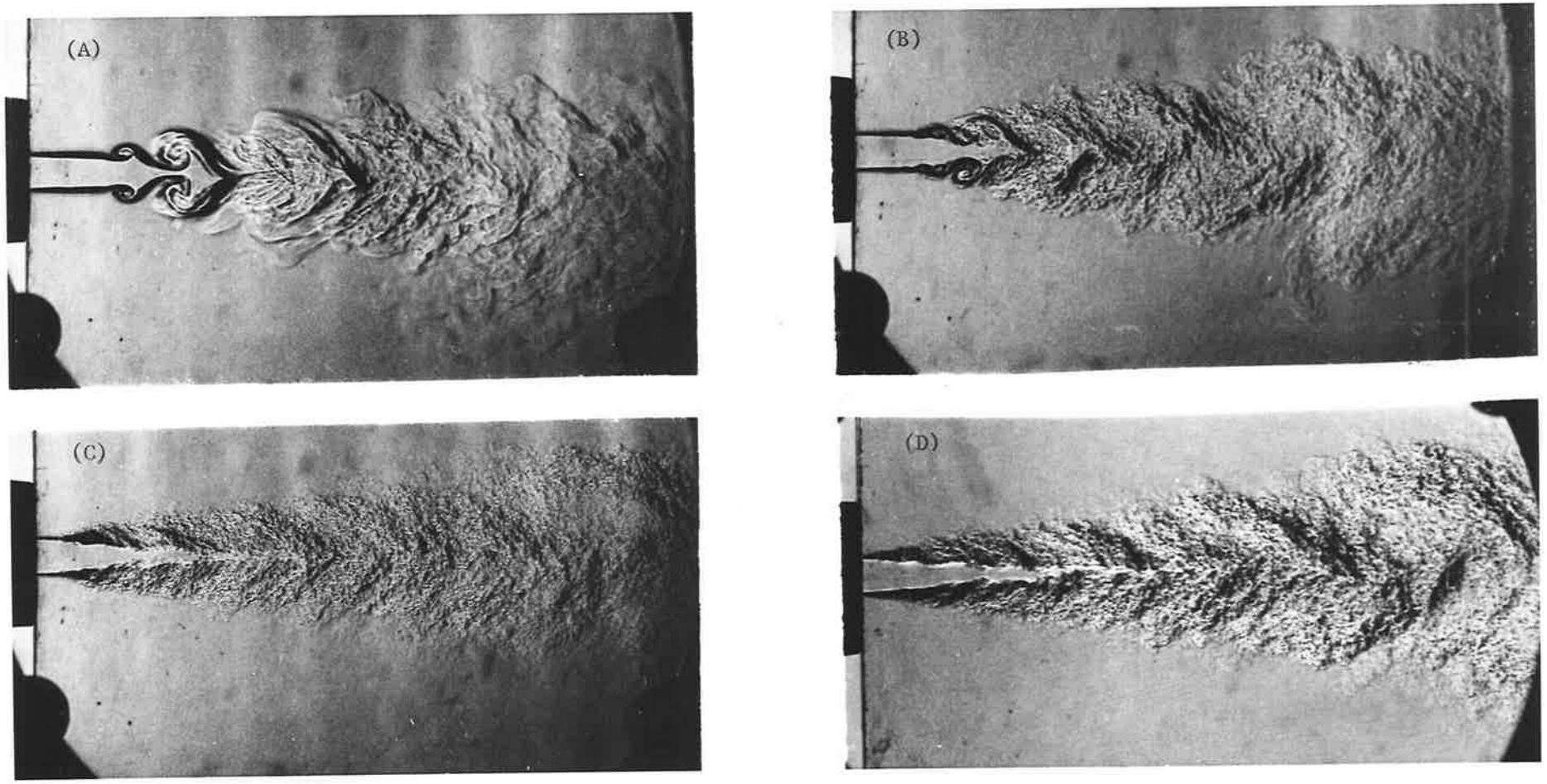

Fig. 3.12 Shadowgraphs of a two-dimensional jet flow.
(ρ_J/ρ_o = 1.52, ν = 8.2 x 10^{-6}, Re = $\frac{UD}{\nu}$; (A) 4.4 x 10^3 ; (B) 4.0 x 10^4 ; (C) 1.2 x 10^5 ; (D) 2.0 x 10^5)

(plate 5)

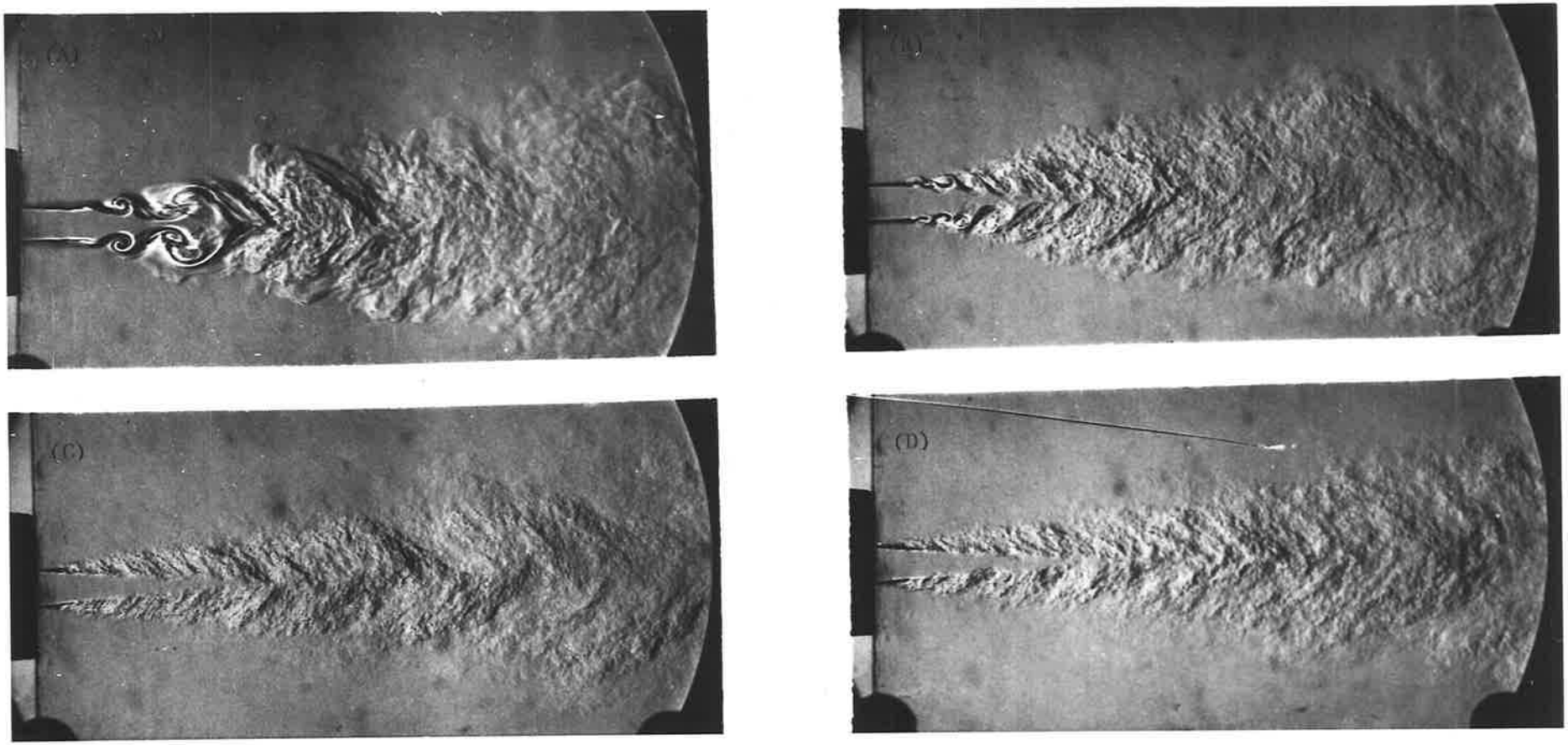

Fig. 3.13 Shadowgraphs of a two-dimensional jet flow
(ρ_J/ρ_o = 1.24, ν = 1.0 x 10^{-5}, Re = $\frac{UD}{\nu}$; (A) 2.5 x 10^3; (B) 2.5 x 10^4; (C) 7.4 x 10^4; (D) 1.5 x 10^5)

(plate 6)

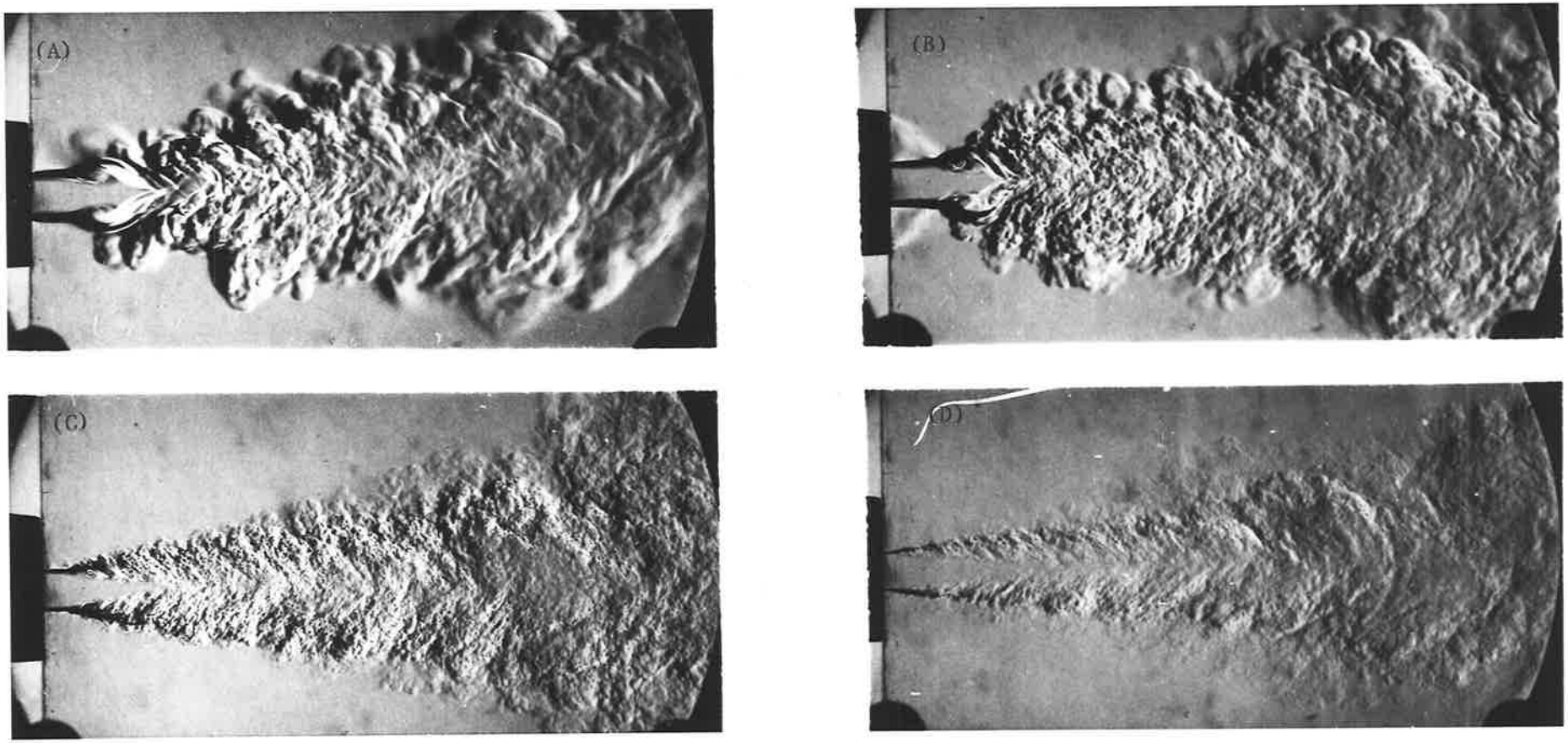

(plate 7)

Fig. 3.14 Shadowgraphs of a two-dimensional jet flow
(ρ_J/ρ_o = 0.57, $\nu = 5.1 \times 10^{-5}$, Re = $\frac{UD}{\nu}$; (A) 4.0×10^2; (B) 4.0×10^3; (C) 1.27×10^4; (D) 6.0×10^4)

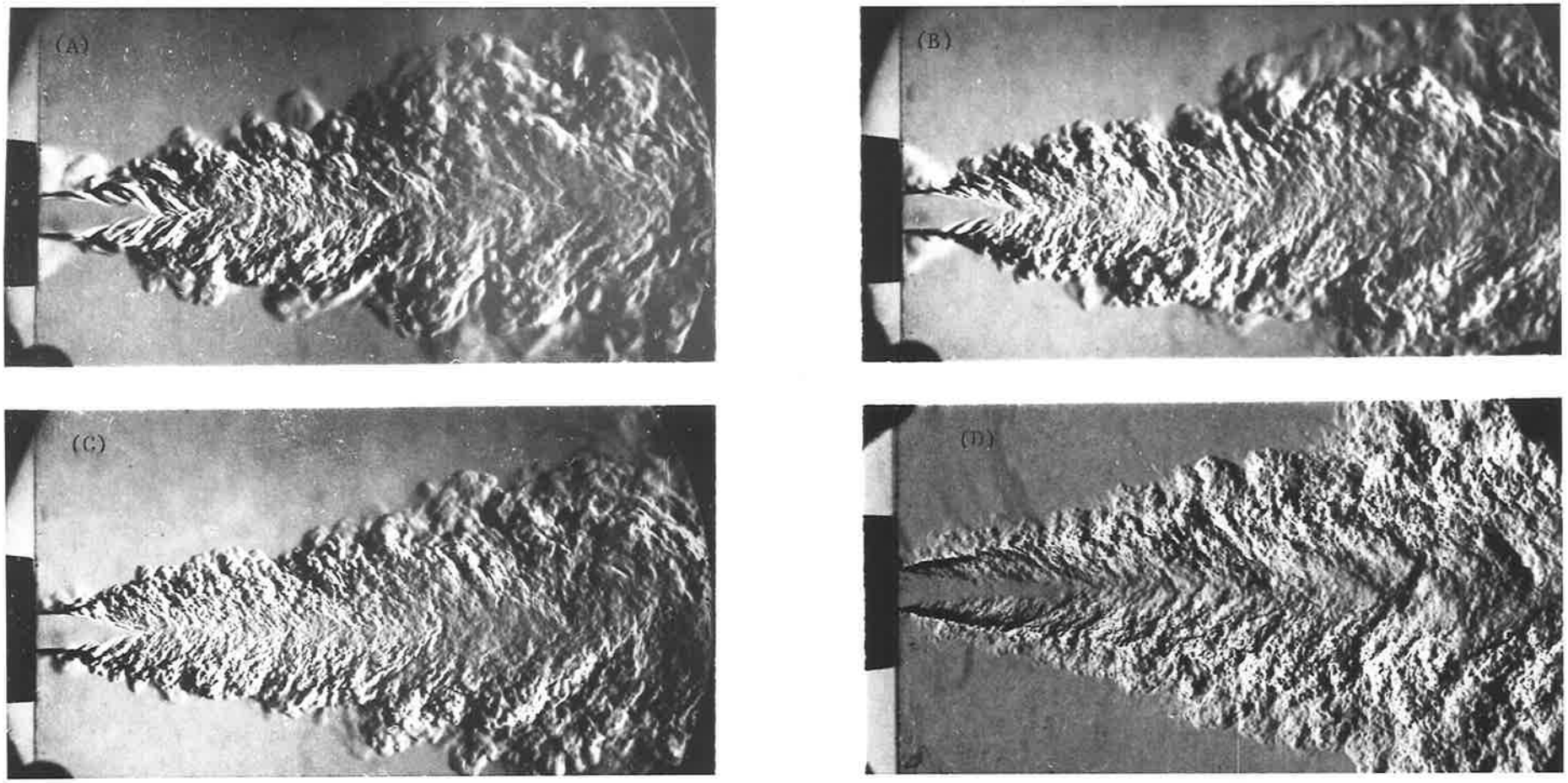

Fig. 3.15 Shadowgraphs of a two dimensional jet flow
($\rho_J/\rho_o = 0.14, \nu = 1.1 \times 10^{-4}$, $Re = \frac{UD}{\nu}$; (A) 1.3×10^3; (B) 2.4×10^3; (C) 7.1×10^3; (D) 2.9×10^4)

(plate 8)

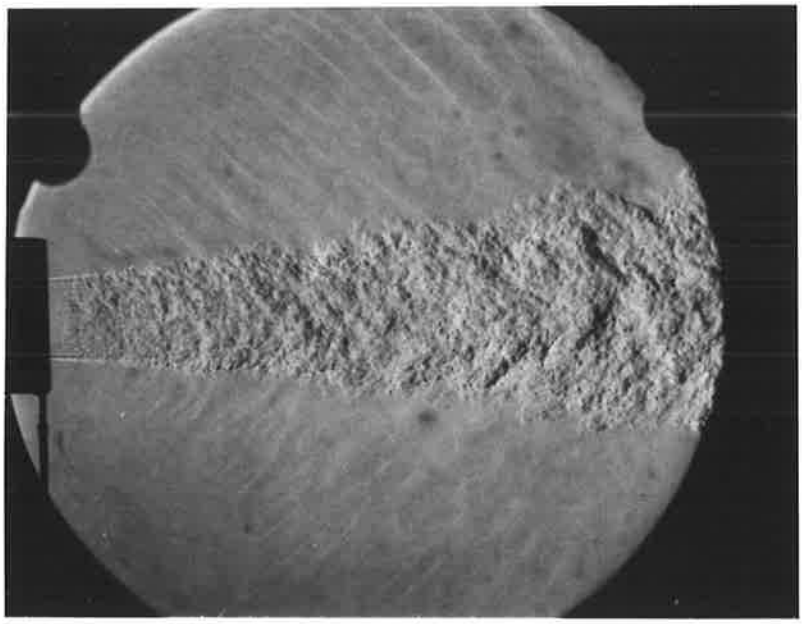

Fig. 3.16 Schlieren picture of a supersonic jet flow.
(ρ_J/ρ_o = 0.637, U_J/a_o = 2.06, Re = 1.78 x 10^5)

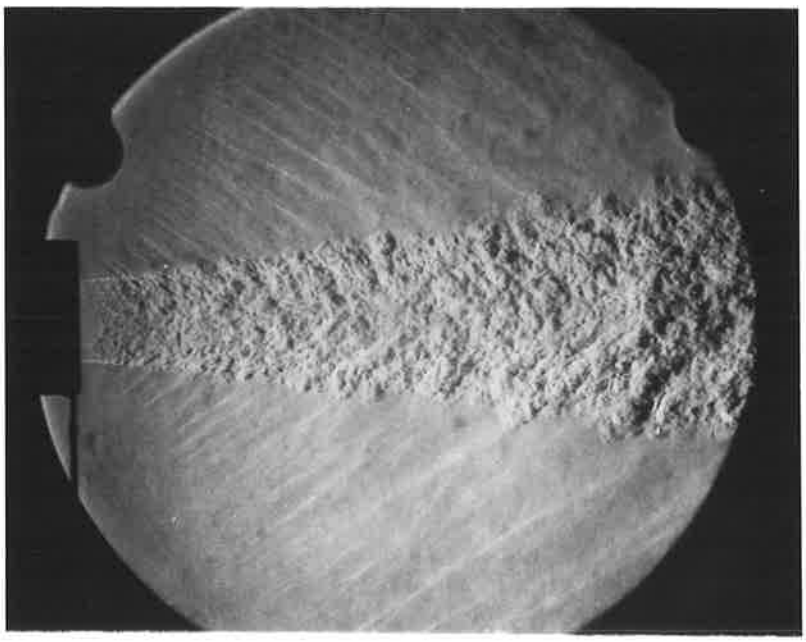

Fig. 3.17 Schlieren picture of a supersonic jet
(ρ_J/ρ_o = 0.6, U_J/a_o = 2.66, Re = 1.92 x 10^5)

4. ACOUSTIC RADIATION CHARACTERISTICS

4.1 ACOUSTIC MEASUREMENTS TEST PROGRAMME

As discussed in chapter three the density effect on the large structure convection speed and spreading rate of the shear layer are in good agreement with the predictions of the mixing layer of Brown (A2) (see appendix A). The model also enables a prediction to be made of an 'average density' in the mixing region. As discussed in chapter one, both the convection speed and mean density are required to predict the intensity from Lighthill's scaling law expressed in equation (1.1). Thus the predicted results could be used to examine the applicability of this scaling law to non-uniform density jets.

As discussed in chapter one, there appears to be no general agreement between the various theoretical models and mechanisms proposed on the excess noise observed in hot jet at low Mach number although all claim to be in agreement with the available hot jet data. It is also unclear whether this excess noise is a result of density inhomogeneity irrespective of how this density difference arises. To date, the only published data on noise from jets of varying composition is from Lassiter and Hubbard (D9). From their limited number of tests they concluded that the sound pressure from air, helium and Freon jet could be predicted by equation (1.1) with ρ_m being the jet density ρ_J. They observed no excess noise provided equation (1.1) was interpreted in this way. However, their experiments appear to be in error at low jet density c.f. the present experimental results and Lockheed's data in Fig. 4.4 and Fig. 4.6. Thus the conclusion drawn from the limited test conditions where jets of different compositions were operated in different velocity regimes, by extrapolation in the velocity direction is therefore in error.

Fig. 4.1 illustrates the test conditions of the flows used in this study. Altogether there are four nozzles employed in this study; one subsonic flow convergent nozzle and three supersonic convergent-divergent nozzles having Mach numbers of 1.3, 1.54 and 1.75 respectively. In the terms of the jet to ambient fluid density ratio and jet velocity to ambient fluid speed of sound ratio, the shaded area in Fig. 4.1 shows the test points that were obtained using the convergent nozzle. Flow conditions available with the convergent-divergent nozzles, which when the flow is correctly expanded operate at specific pressure ratios, depending on the working gas, are represented by the three solid lines.

A particular advantage of the experimental facilities was that it was a simple matter to maintain at approximately constant density while varying the velocity (i.e. test points on horizontal broken lines) by varying the compositions of the working gas to account for compressibility effects as the speed was increased.

In this experiment, a total of 49 tests conditions were selected. There were shown as the points marked Fig. 4.1. For each test condition, the required mixture of the working gas and pressure upstream of the nozzle was first calculated and the actual flow conditions at the exit were recalculated from the measured stagnation pressures. The actual flow exit conditions for each test point in Fig. 4.1 are tabulated in Table 4.1. From such an extensive test programme, effects of density and velocity can be determined independently from these measurements. It was hoped that such an extensive set of data obtained in a single facility with the same instrumentation would provide a bench mark against which theoretical models and predictions schemes for jet noise could be checked.

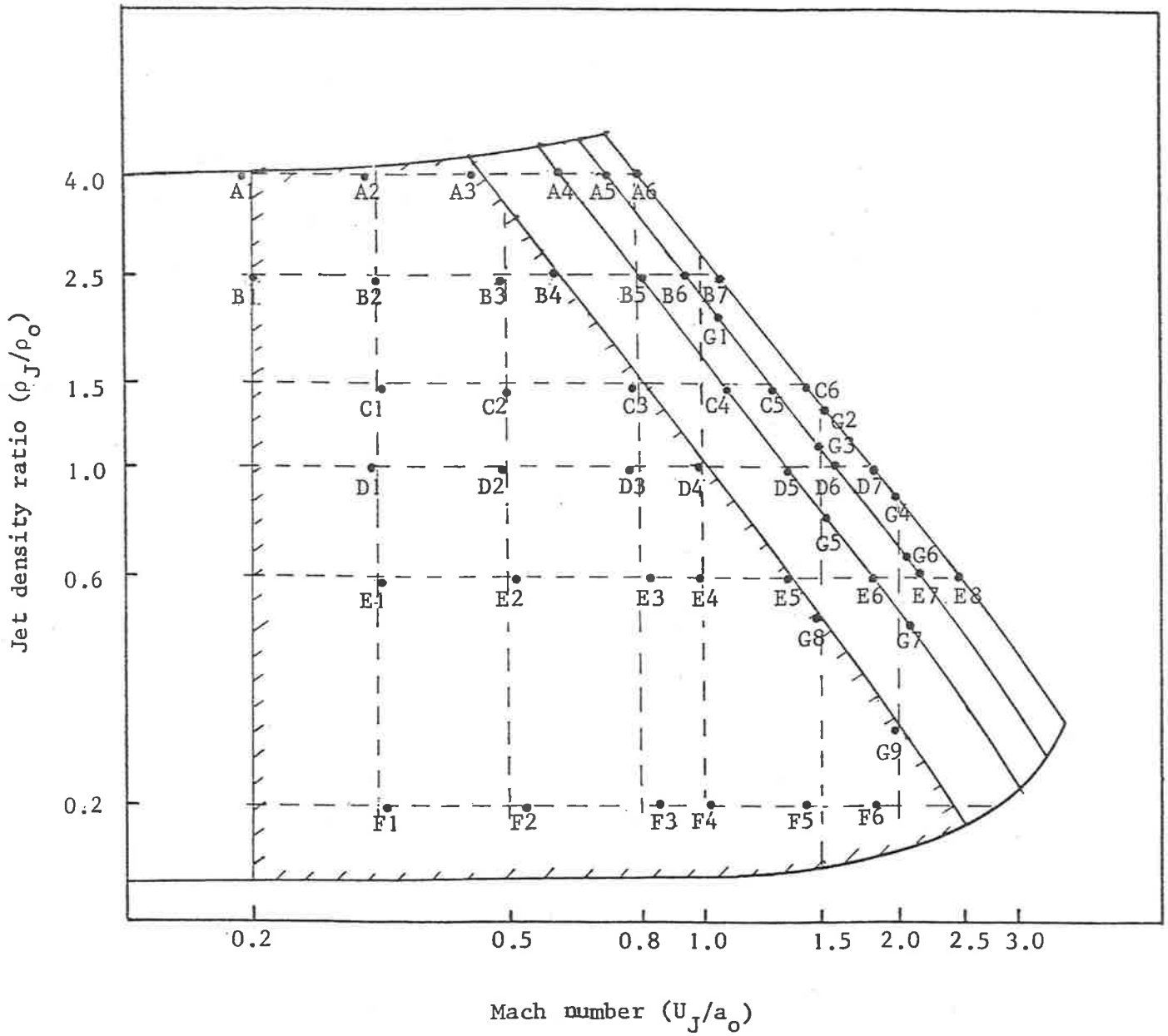

Fig. 4.1 Test Programme Chart

Table 4.1 Test point flow exit conditions

Test Point	U_J/a_o	U_J/a_J	R_J/R_o	γ_J/γ_o	ρ_J/ρ_o
A1	0.192	0.419	0.256	0.813	3.946
A2	0.283	0.613	0.268	0.817	3.833
A3	0.453	1.00	0.269	0.822	4.003
A4	0.596	1.311	0.282	0.827	4.013
A5	0.700	1.535	0.298	0.831	3.996
A6	0.794	1.747	0.310	0.835	4.046
B1	0.201	0.342	0.408	0.858	2.482
B2	0.303	0.511	0.418	0.861	2.450
B3	0.495	0.814	0.455	0.871	2.355
B4	0.581	0.987	0.439	0.870	2.518
B5	0.770	1.289	0.481	0.610	2.458
B6	0.914	1.533	0.512	0.888	2.500
B7	1.050	1.533	0.557	0.899	2.488
C1	0.314	0.393	0.597	0.929	1.464
C2	0.500	0.609	0.756	0.940	1.401
C3	0.791	0.995	0.773	0.948	1.499
C4	1.043	1.293	0.871	0.996	1.493
C5	1.267	1.537	1.000	1.000	1.472
C6	1.435	1.742	1.094	1.012	1.491
D1	0.296	0.295	1.017	1.002	1.000
D2	0.490	0.487	1.052	1.001	0.994
D3	0.785	0.771	1.143	1.018	0.986
D4	0.995	0.983	1.206	1.024	1.001
D5	1.314	1.287	1.379	1.041	0.998
D6	1.594	1.558	1.567	1.057	1.088
D7	1.804	1.743	1.756	1.070	0.999

Table 4.1 Test point exit flow conditions

Test Point	U_J/a_o	U_J/a_J	R_J/R_o	γ_J/γ_o	ρ_J/ρ_o
E1	0.301	0.225	1.704	1.066	0.594
E2	0.517	0.387	1.731	1.068	0.599
E3	0.826	0.614	1.834	1.076	0.595
E4	0.979	0.734	1.867	1.077	0.595
E5	1.337	0.996	2.110	1.091	0.596
E6	1.741	1.283	2.414	1.118	0.600
E7	2.114	1.565	2.760	1.118	0.612
E8	2.395	1.749	3.134	1.129	0.602
F1	0.316	0.130	5.061	1.166	0.199
F2	0.549	0.225	5.106	1.166	0.199
F3	0.841	0.354	5.106	1.166	0.203
F4	1.090	0.449	5.355	1.167	0.199
F5	1.411	0.579	5.613	1.171	0.197
F6	1.818	0.746	5.962	1.173	0.198
G1	1.055	1.584	0.667	0.921	2.030
G2	1.525	1.753	1.231	1.027	1.358
G3	1.493	1.550	1.383	1.044	1.123
G4	1.957	1.763	2.052	1.088	0.882
G5	1.553	1.301	1.889	1.078	0.758
G6	2.062	1.560	2.635	1.113	0.637
G7	2.011	1.313	3.117	1.129	0.481
G8	1.485	0.989	2.587	1.110	0.491
G9	1.916	0.975	4.319	1.153	0.299

4.2 SCALING PARAMETERS FOR JET NOISE MEASUREMENTS

4.2.1 FREQUENCY PARAMETER

In Lighthill's analysis where the stress tensor T_{ij} is approximated by the Reynolds stress $\rho U_i U_j$ the resultant scaling law for the far field intensity is expressed in equation (1.1).

Since the sources embedded in the shear layer are in motion the observed frequency f in a fixed frame of reference is Doppler shifted to give the source frequency f_s by the following relationship

$$f_s = f\ (1 - M_c \cos\theta) \quad . \tag{4.1}$$

The normalised frequency parameter f_N often used in the study of jet noise is

$$f_N = \frac{f_s D}{U_J} \quad . \tag{4.2}$$

Ffowcs Williams (B3) showed that the term $(1 - M_c \cos\theta)$ in equation (4.1) should be replaced by

$$\left| (1 - M_c \cos\theta)^2 + \alpha^2 M_c^2 \right|^{\frac{1}{2}} \quad . \tag{4.3}$$

The parameter α was introduced to account for the finite life of an eddy. It also eliminated the singularity when $M_c \cos\theta = 1$. This parameter is normally taken as 0.3 as measured by Davies et. al. (A9).

The frequency parameter to be derived here is based on the optical observation and flow measurement of the mixing layer in chapter three. A non-dimensional frequency $f_N = \frac{f_s D}{U_J}$ will in general be a function of the density ratio. It was thought in this work that since a major effect of the density difference was to change the convection speed of the large structure that a more

characteristic time for the life of the large eddies, particularly in the later part of the potential core, would be scaled by D/U_c. Thus a non-dimensional frequency also considered in this work was

$$f_N = \frac{f_s D}{U_c} \tag{4.4}$$

where U_c/U_J is a function of density ratio ρ_J/ρ_o given by equation (7.5) in the appendix. Thus the frequency parameter in equation (4.4) becomes

$$f_N = \frac{f \left| (1 - M_c \cos\theta)^2 + \alpha^2 M_c^2 \right|^{\frac{1}{2}} D}{U_c} \tag{4.5}$$

4.2.2 SOURCE DENSITY PARAMETER

The other important scaling parameter in jet noise is the density term ρ_m that appears in equation (1.1). The mixing layer model of Brown (A2) which seems to predict the spreading rate of the mixing layer and the velocity of the flow rather well can be used to calculate the average flow density in the mixing layer. The result is given in equation (7.13) which is repeated here for convenience,

$$\frac{\rho_m}{\rho_o} = \frac{1/s + K(s)}{1 + K(s)} \tag{4.6}$$

The values obtained from this relation are compared to those values assumed in other published experiments and are tabulated below.

The values in the last column are calculated from equation (4.6) assuming $K(s) = s^{-0.6}$. When $K(s) = s^{-0.5}$ is used the values are identical to those values obtained using the geometric mean method as shown in column two. As expected these values are closer to

$\frac{\rho_J}{\rho_o}$	$\frac{\rho}{\rho_o} = \sqrt{\rho_J/\rho_o}$	$\frac{\rho_m}{\rho_o} = \frac{\rho_J + \rho_o}{2\rho_o}$	$\frac{\rho_m}{\rho_o} = \frac{1}{0.7(\frac{\rho_o}{\rho_J} - 1) + 1}$	$\frac{\rho_m}{\rho_o} = \frac{1/S + K(S)}{1 + K(S)}$
4.0	2.00	2.50	2.10	2.30
2.5	1.58	1.75	1.72	1.73
1.5	1.22	1.25	1.30	1.27
1.0	1.0	1.0	1.00	1.00
0.6	.78	0.80	.68	.74
0.2	.45	0.60	.26	.38

the lower of the densities on the two sides of the shear layer since the entrainment rate is relatively higher on the lower density side. The values in the second last column from Tanna et. al (D2) in the hot jet experiment are based on the assumption that the static temperature profile is similar to the velocity profile and the region of maximum turbulent intensity or the source region is of the order 0.7 times the jet efflux velocity. The source density ρ_m calculated using the mixing layer model falls in between the geometric mean (jet and ambient density) and the value of Tanna for $\rho_J/\rho_o \leq 1.5$. At higher densities values obtained using the 2-D model are the highest among the three.

4.3 RESULTS AND DISCUSSION OF ACOUSTIC MEASUREMENTS

4.3.1 Velocities and density dependence of overall intensity

Fig. 4.2 shows the velocity dependence of the far field noise intensity for different jet densities measured at $\theta = 90^o$ where the effects of refraction and convection amplification are absent. For uniform density jet ($\rho_J/\rho_o = 1.0$) an intensity which varies as $(U_J/a_o)^{7.0}$ from $U_J/a_o = 0.3$ to $U_J/a_o = 1.5$ fits the data better than

Lighthill's eighth power law. Deviations from the $(U_J/a_o)^{8.0}$ law of the overall intensity for this constant density jet have been obtained in many experiments over smaller velocity ranges and less than ambient densities (D1-D6).

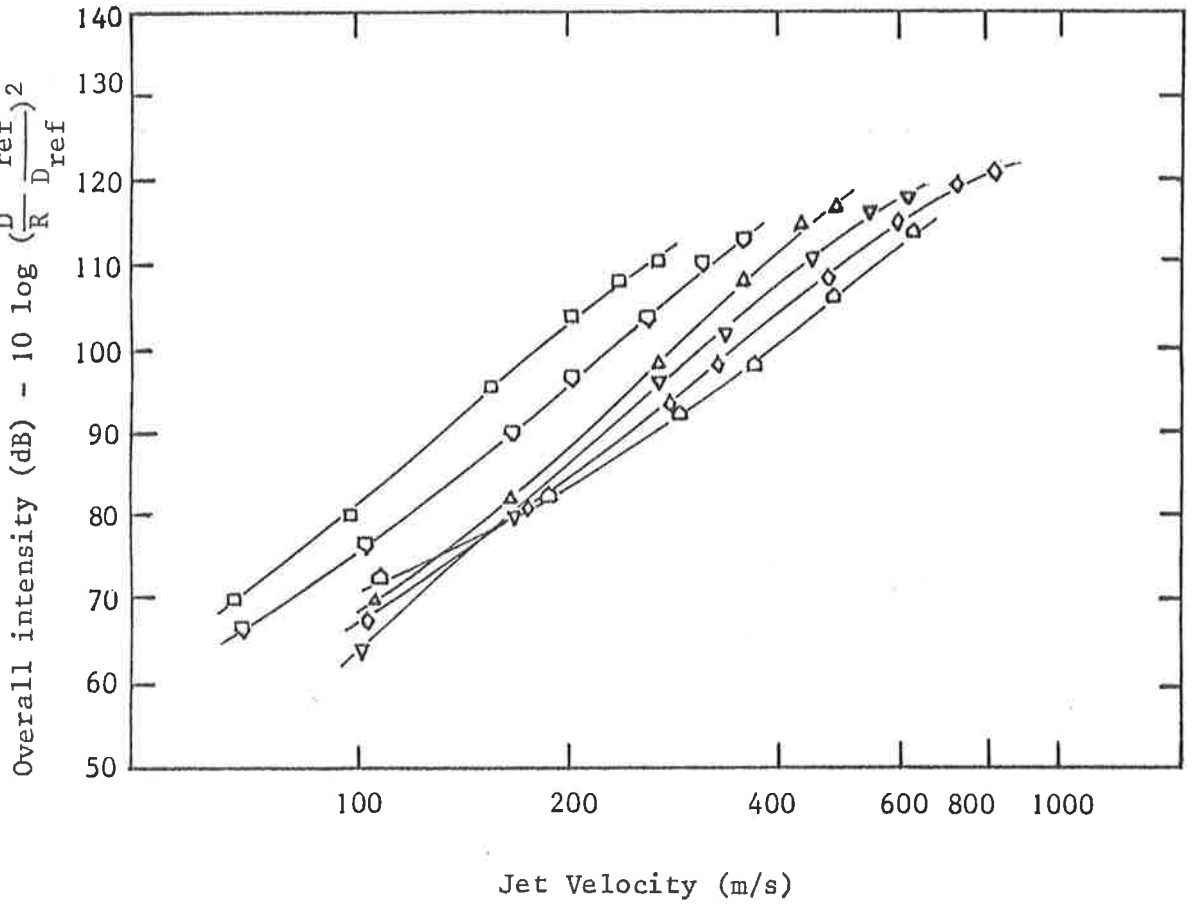

Fig. 4.2 The effect of density on the velocity dependence of the overall intensity at $\theta = 90^0$

(R_{ref} = 1.68 m and D_{ref} = 0.0287 m)

(ρ_J/ρ_o ; □, 4.0; ▽,2.5; △,1.5; ▽,1.0; ◇ ,0.6; ⌓,0.2)

For jet density ratio ρ_J/ρ_o less than unity, the intensity appears to scale on a lower power of velocity. For ρ_J/ρ_o = 0.2, when $U_J/a_o > 0.5$ the intensity is approximated by $(U_J/a_o)^{6.0}$ and for $U_J/a_o < 0.5$, it scales as $(U_J/a_o)^{5.0}$. Thus, relative to the constant density jet, lower density jets are observed to be noisier at low velocity. In the case of the heavier than air jet the overall intensity is higher. For ρ_J/ρ_o = 2.5 and ρ_J/ρ_o = 4.0

it varies as $(U_J/a_o)^{6.5}$ throughout the range of velocity considered.

In Fig. 4.3, the overall intensities at $\theta = 90^o$ are normalised by $(\rho_m/\rho_o)^{2.0}$ where ρ_m is the respective source density from equation (4.6). A good collapse onto the $\rho_J/\rho_o = 1.0$ curve is obtained at high

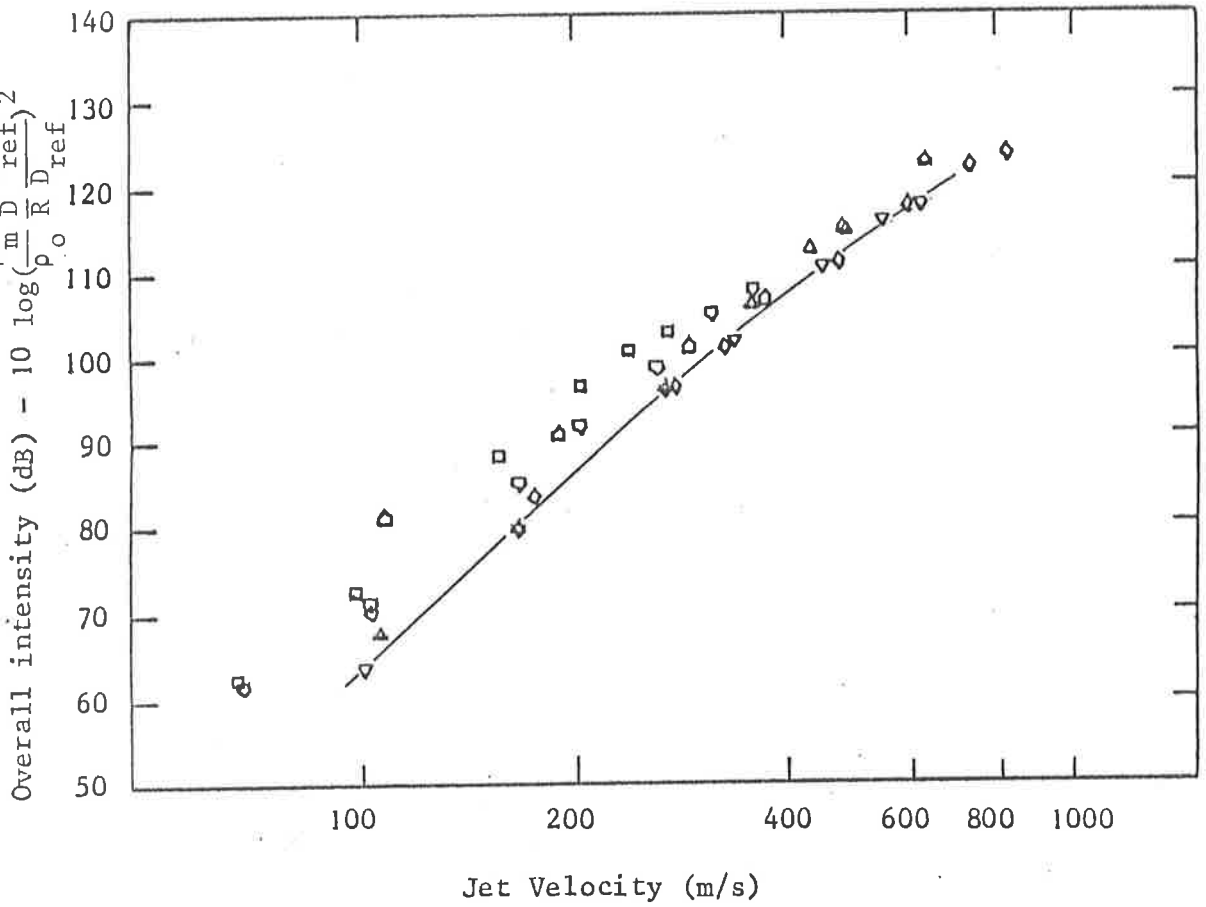

Fig 4.3 The velocity dependence of the normalised overall intensity at $\theta = 90^o$

(R_{ref} = 1.68m, D_{ref} = 0.0287 m)

(ρ_J/ρ_o; □, 4.0; ▽, 2.5; △, 1.5; ▽, 1.0; ◇, 0.6; ⌂, 0.2)

velocity and the collapse becomes progressively poorer at low Mach number where non uniform density jets are found to be relatively noisier. This result tends to support the view that the Reynolds stress source term, whose far field intensity should vary as $(\rho_m/\rho_o)^{2.0}$, predominates at high Mach number and it is also obvious from the scaling result that excess noise, which exists in non-uniform density jets, becomes significant in the low velocity region.

Considering that in this study the intensity of a uniform density jet varies as $(U_J/a_o)^{7.0}$, the fifth to sixth power velocity dependence of the intensity of the excess noise suggests that the source is dipole in character. These results lend support to Morfey's view that in a non-uniform density jet there are two sources; a quadrupole type from Reynolds stress which predominates at high velocity and a dipole type that predominates at low velocity.

At high Mach number, a reduction in the noise intensity is observed for all jets. At supersonic Mach numbers the role of the large structure becomes less significant as compressibility begins to affect the development of the large scale vortical motions. This is evident from the significant thinning of the mixing layer in supersonic flow as seen in the shadowgraphs in chapter three.

In comparing the density effect on turbulent mixing in supersonic and incompressible variable-density flow, where the equations of motion for the compressible case are the mass, momentum and energy equations, while the governing equations for the other case are the mass, momentum and diffusion equations, Brown and Roshko's analysis (A1) showed that compressibility effects are distinct from the effects due to density difference alone. At high Mach number, compressibility effects introduce a $\overline{P'v'}$ term which they assert accounts for the marked difference between Mach number zero and high Mach number mixing layers having the same velocity and density ratio. From the order of magnitude estimate (for detail see (A1)) Reynolds stress $\overline{u'v'}$ is proportional to the spreading rate of the mixing layer, which decreases with increasing Mach number.

To date, data on noise from jets of varying compositions are limited. The only available data are those from Lassiter and Hubbard (D9) where the range of flow conditions covered are very

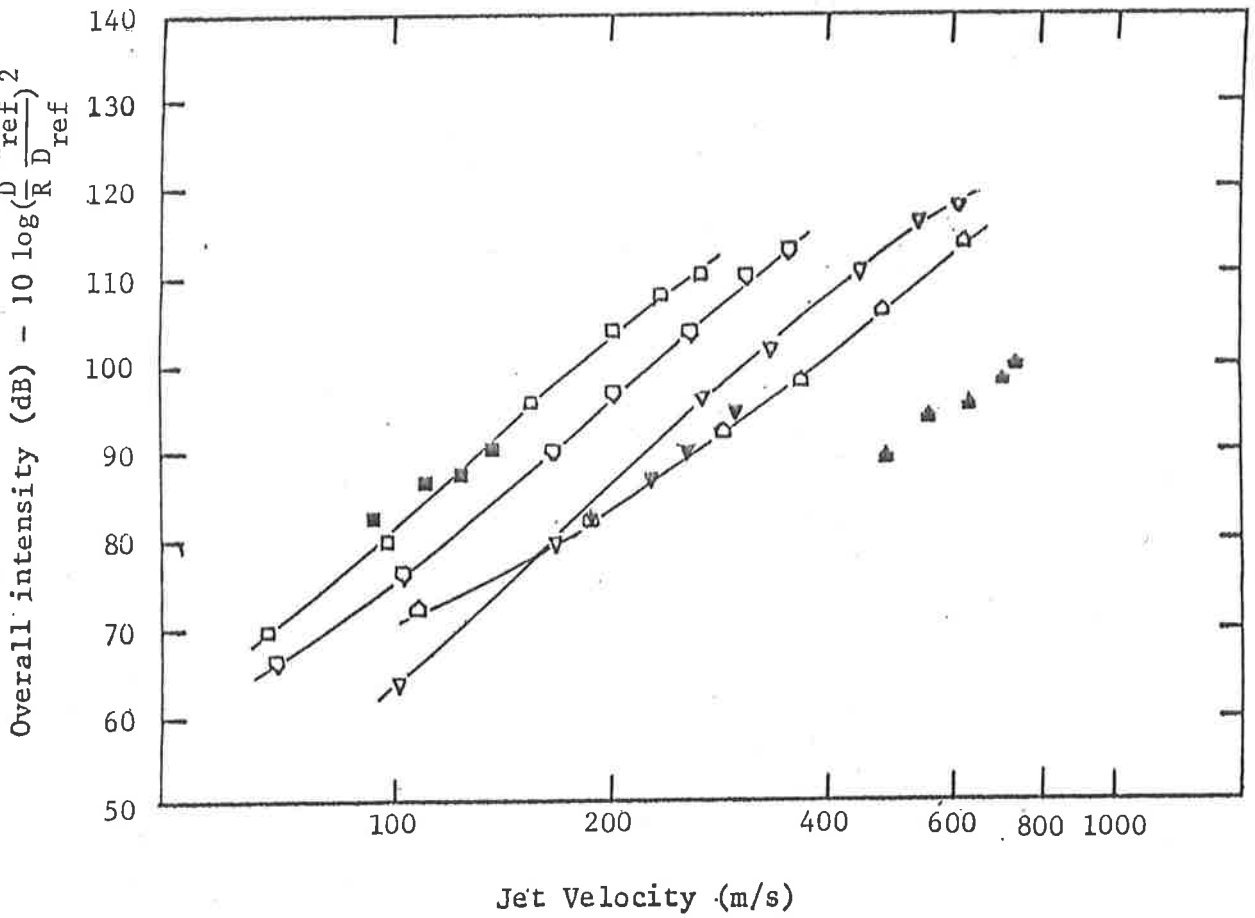

Fig. 4.4 The effect of density on the velocity dependence of the overall intensity at $\theta = 90^{o}$

(R_{ref} = 1.68m and D_{ref} = 0.0287m)

— measured: □, ρ_J/ρ_o = 4.0; ▽, 2.5; ▽, 1.0; ⌂, 0.2

— Lassiter & Hubbard : ■, Freon Jet; ▼, air jet;

⏏, Helium jet

limited. In their tests where air, helium and Freon 12 were used as jet fluids, only four to five tests of different velocities were conducted for each fluid. Their data are compared to the present measurements in Fig. 4.4. It should be noted that in their experiments, the jet density for each working fluid is not constant due to the increasing Mach number. The jet exit conditions for the highest flow velocities considered in each fluid in their test are tabulated in Table 4.2.

Table 4.2 Flow parameters for jet noise test (obtained from Lassiter and Hubbard (D9) Table 1)

Medium	Mexit = U_J/a_o	U_J/a_J	ρ_J/ρ_o
Air	0.9	0.82	1.19
Helium	0.9	2.33	0.20
Freon 12	0.9	0.37	4.83

For the air jet, their intensities are 3-5 dB lower than the constant density jet in this experiment. While for the Freon jet the intensities are within 2-3 dB to the measured intensities of $\rho_J/\rho_o = 4.0$ case. Their result is in agreement with the observed trend where the denser jet is noisier. However, their Helium jet measurements which showed a difference of 17-18 dB lower than the $\rho_J/\rho_o = 0.2$ case in this study appeared to be in error. Unfortunately, comparison in the lower velocity region is not possible as their tests for helium jets were conducted only in high velocities.

By extrapolating in the velocity direction from the limited test points coupled with the erroneous Helium jet measurements their conclusion that far field sound intensity should vary as jet density was unfortunately in error and also the phenomenon of excess noise from the inhomogeneous density jets was not observed.

The velocity dependence of the overall intensity at $\theta = 90^o$ measured by Tanna (D2) on a hot jet is reproduced in Fig. 4.5. For different jet temperatures, the overall intensity exhibits the same trend as observed in Fig. 4.2 where lighter jets are noisier at low velocity, a trend which is reversed at high velocity. Comparisons of the two sets of results are made by considering the equivalent density ratios of the hot jet using the relationship $T_J/T_o = \rho_o/\rho_J$. The equivalent density ratios for jet flows of the temperature ratios in Fig. 4.5 are tabled below.

T_J/T_o	1.0	2.3	3.4
ρ_J/ρ_o	1.0	0.43	0.29

In the present study, there is no flow with the density ratios the same as the equivalent densities for hot jets of T_J/T_o = 2.3 and 3.4.. Thus comparison is made in cases in this study where density ratios are nearest to the equivalent density ratios. As shown in Fig. 4.6 the close agreement in the overall intensity between the

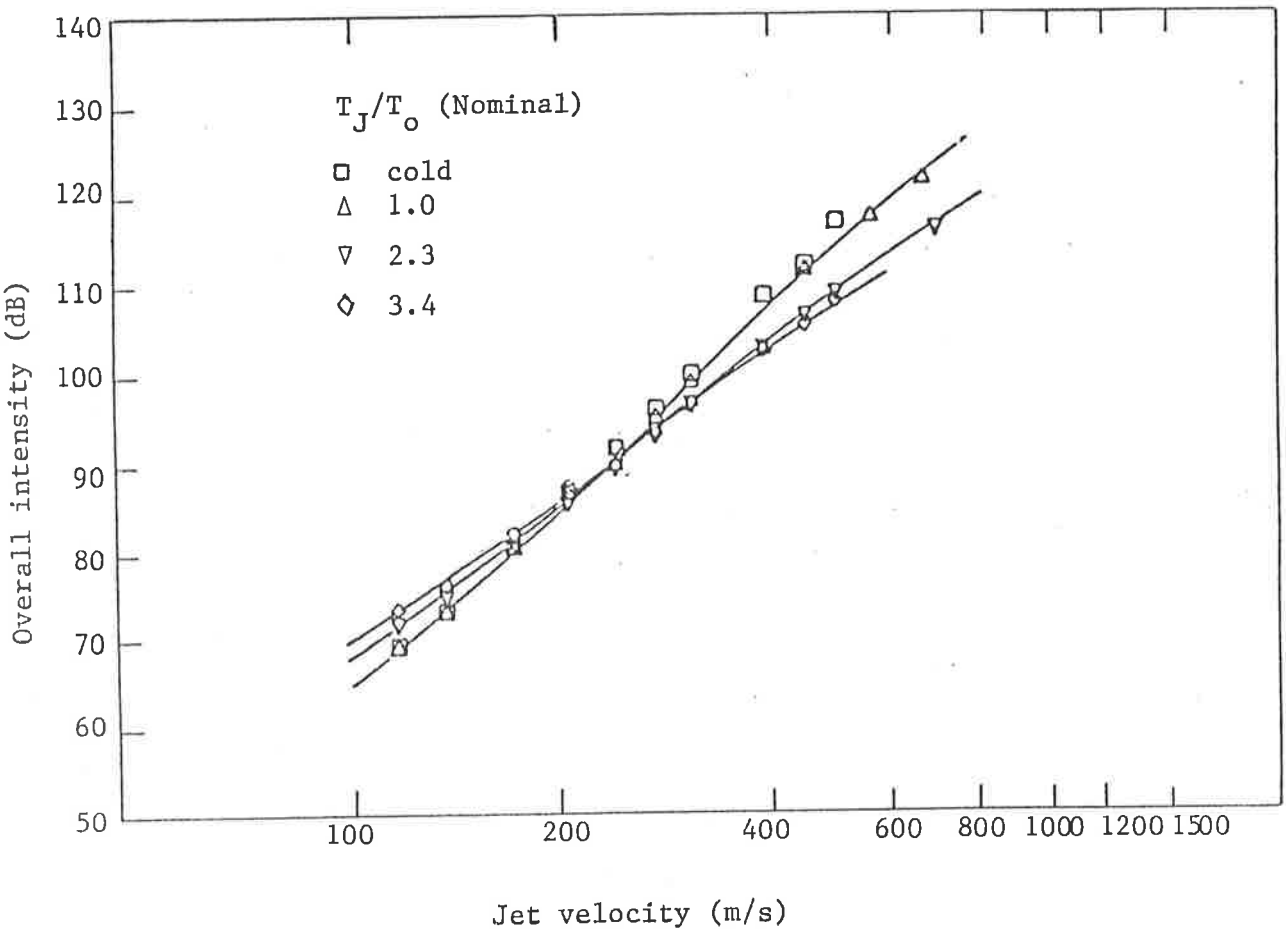

Fig. 4.5 Effect of density ratio on velocity dependence of OASPL (Lockheed)

two sets of results over such a wide density and velocity range is remarkable. For the uniform density jet of ρ_J/ρ_o = 1.0, the differences

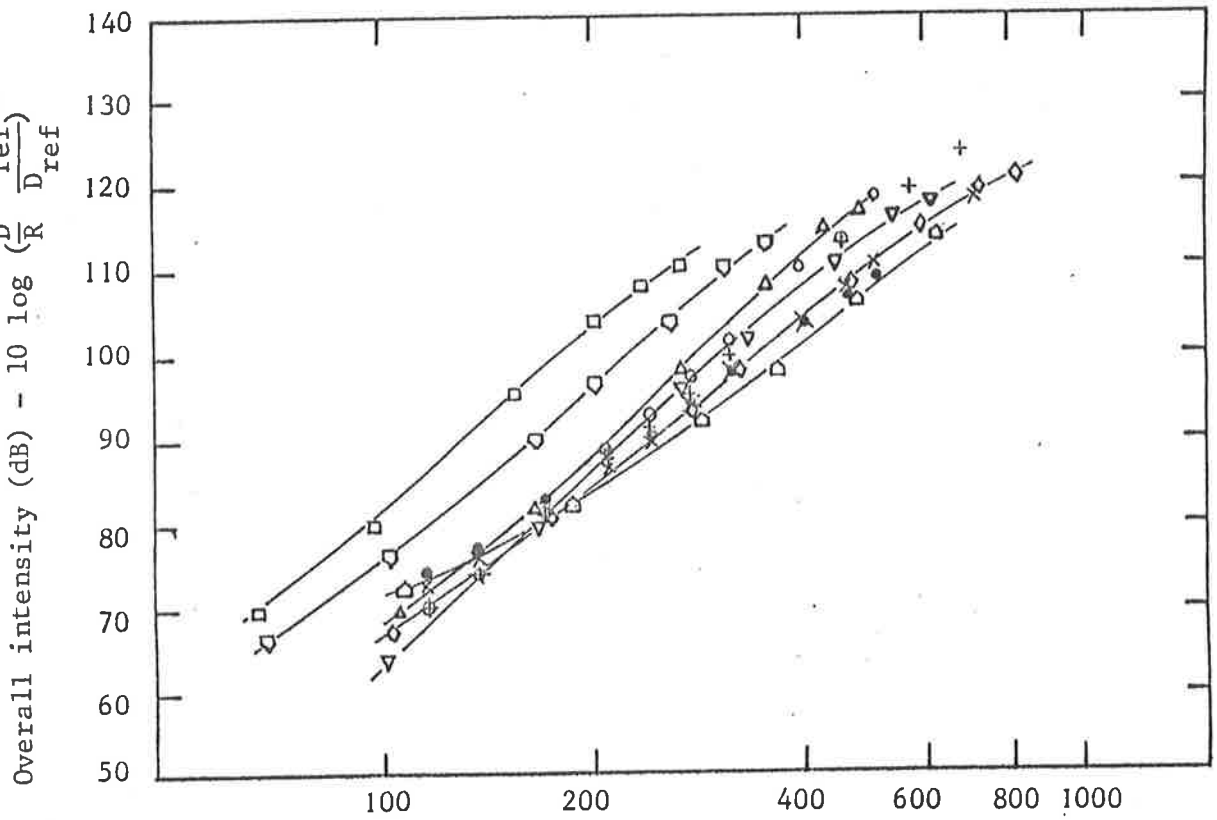

Fig. 4.6 Velocity dependence of overall intensity at $\theta = 90^o$ for jets of various densities.

— measured: □, ρ_J/ρ_o = 4.0; ▽, 2.5; Δ, 1.5; ∇, 1.0; ◇, 0.6; ⌂, 0.2

— Lockheed: +, T_J/T_o = 1.0 (ρ_J/ρ_o = 1.0); x, 2.3, (0.43) ●, 3.4, (0.29); o, cold jet

in the normalised overall intensities between the varying temperature and varying compositions cases are within 2 - 3 dB. In the hot jet where ρ_J/ρ_o = 0.29 (T_o/T_o = 3.4) the overall intensities are consistently higher than the varying composition case where ρ_J/ρ_o = 0.2. At this low density discrepancies in the medium velocity range are as high as 4 - 5 dB whereas in low and high velocities it is about 1-2 dB. Based on the density scaling of $(\rho_J/\rho_o)^2$ the intensities for ρ_J/ρ_o = 0.29 case should be 3.2 dB higher than ρ_J/ρ_o = 0.2 case at the same velocity. Thus, taking density scaling into consideration, the dis-

crepancy between these cases is therefore reduced. For ρ_J/ρ_o = 0.43 in hot jet (T_J/T_o = 2.3) the intensity at high velocity is nearly the same as for the case of ρ_J/ρ_o = 0.6 in the present study and it becomes relatively higher with decreasing velocity. Based on density scaling between the two cases, the intensities for the hot jet should be lower by 2.9 dB at the same velocity. Thus the actual discrepancy is about 3 dB at high velocity. At low velocity the intensities for ρ_J/ρ_o = 0.43 fall in between those for ρ_J/ρ_o = 0.2 and 0.6 as shown in Fig. 4.6 this is consistent with the observed trend that lighter jet is noiser at low velocities.

4.3.2. Effect of Velocity and Density on One-Third Octave Spectra

The measured one-third octave spectra for $\theta = 20^o$ to 90^o at all the operating conditions have been examined and the effects of velocity and density are discussed.

For a uniform density jet (ρ_J/ρ_o = 1.0) the measured one-third octave spectra for a range of velocities at $\theta = 45^o$ and $\theta = 90^o$ are represented in Fig. 4.7. At $\theta = 90^o$ as in Fig. 4.7 (A) the spectra are rather broad and the peak frequency increases monotonically with velocity. At angles closer to the jet axis the peaks of the spectra become more pronounced as seen in Fig. 4.7 (B) where $\theta = 45^o$. When the same data are plotted in Fig. 4.8 on a source Strouhal number basis as defined by equation (4.5) at $\theta = 90^o$, the spectra at subsonic velocities appears to collapse rather well with the peaks occuring at nearly the same Strouhal number. However, at angles closer to the jet axis, as in Fig. 4.8(B) and Fig. 4.8(C) where $\theta = 45^o$ and $\theta = 30^o$ respectively, the peak Strouhal numbers are seen to decrease slowly as

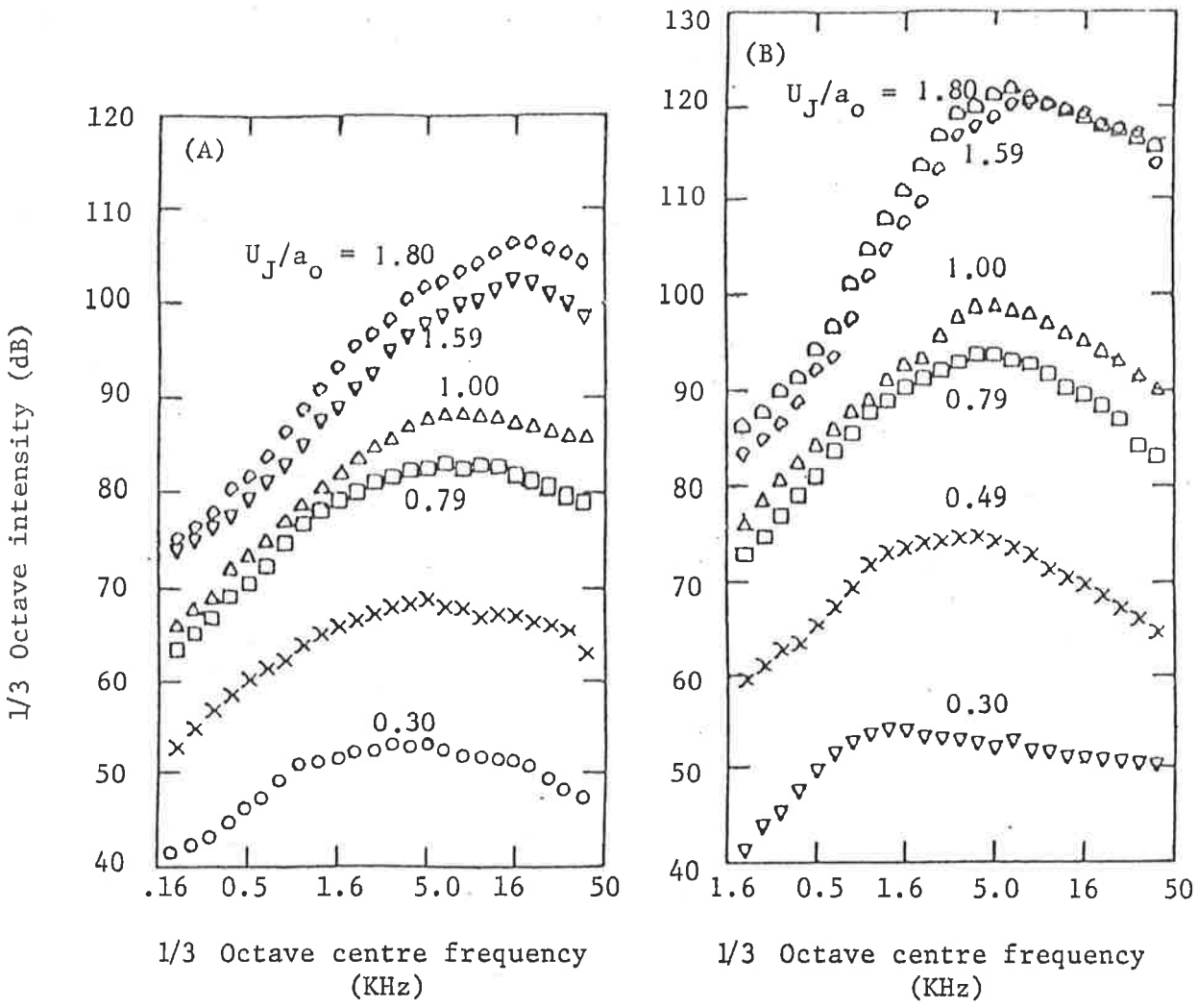

Fig. 4.7 The influence of velocity on the 1/3 octave spectra for a constant density jet. ((A) $\theta = 90^o$, (B) $\theta = 45^o$)

the jet speed increases. The variation of the peak Strouhal number with angular position and velocity for a uniform density jet is plotted in Fig. 4.9. At a fixed velocity the peak source Strouhal number decreases steadily as one moves closer to the jet axis. This is consistent with the observation of Lush (D1) who demonstrated that the convective amplification of the sound is much reduced if the wavelength is short compared to the sound path length through the mixing layer. At higher velocity the noise generated is in the higher frequency range and, at a small radiation angle, the sound path length through the layer is long and the reduction in the

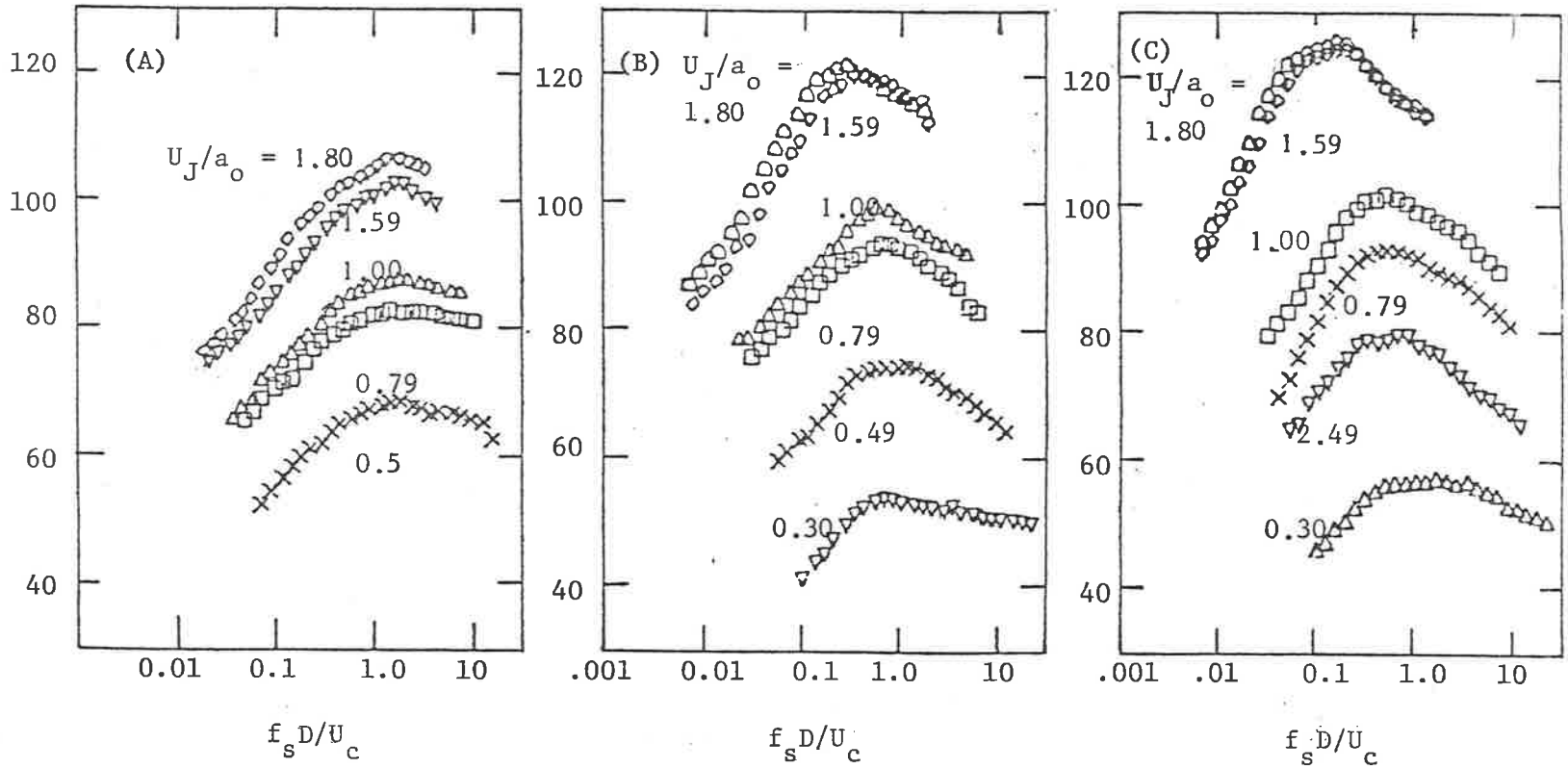

Fig. 4.8 Influence of velocity on the dimensionless frequency spectra for a constant density jet.

(A) $\theta = 90^o$, (B) $\theta = 45^o$, (C) $\theta = 30^o$

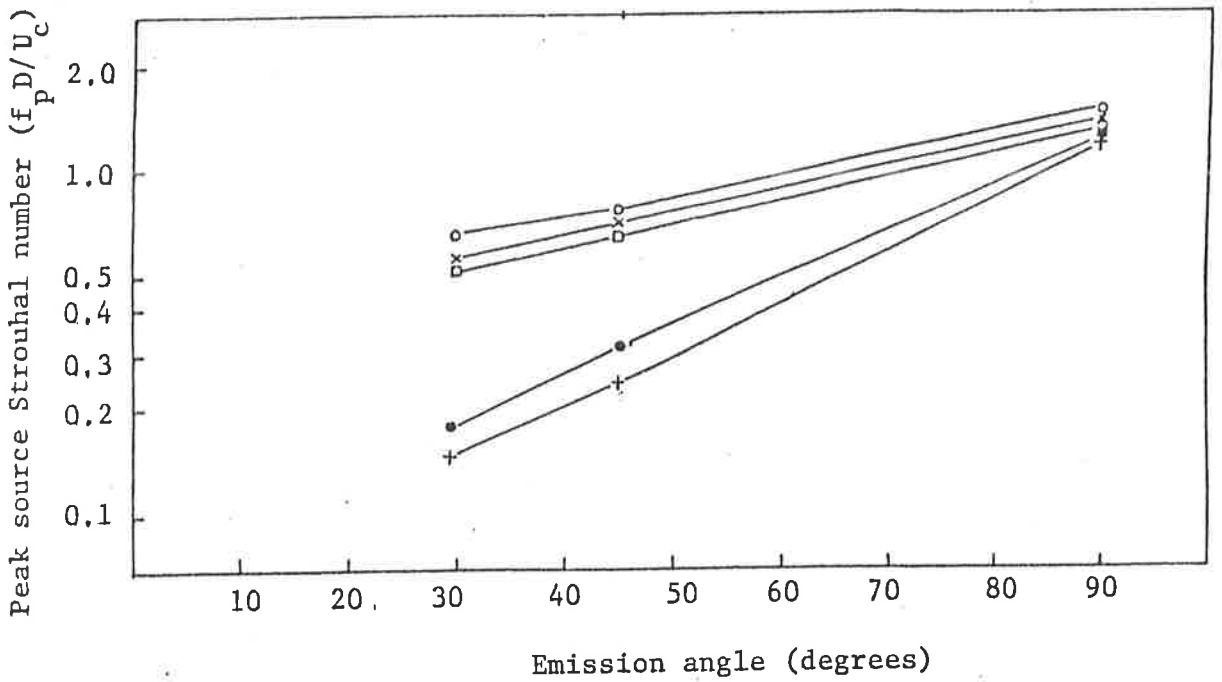

Fig. 4.9 Variation of peak Strouhal number with angular position (ρ_J/ρ_o = 1.0; U_J/a_o: o, 0.49; x, 0.79; □, 1.00; •, 1.59; +, 1.80)

convective amplification effectively shifts the spectral peaks to the lower frequencies. For supersonic flow, although the peak source Strouhal number at $\theta = 90^o$ is nearly the same as for the subsonic flow, it decreases drastically with θ. This occurs when the source convection speed is supersonic relative to the ambient speed of sound and Mach waves of a fixed frequency are radiated predominantly in the Mach angle $\theta_m = \cos^{-1}(\frac{a_o}{u_c})$. The Mach waves are clearly visible in Fig. 3.1., Fig. 3.17 and Fig. 3.18 radiating in the forward arc direction.

The effect of density on the 1/3 octave spectra is demonstrated by the measurements made at $\theta = 45^o$. In Fig. 4.10 the spectra at four different jet velocities U_J/a_o of 0.5, 1.0, 1.5 and 2.0 for various densities are presented on the dimensionless frequency scale, $f_s D/U_J$, as defined by equation (4.2) and equation (4.3) where $M_c = \frac{U_c}{a_o}$ and U_c has been taken as (0.63 - 0.67) U_J, as has been done in many

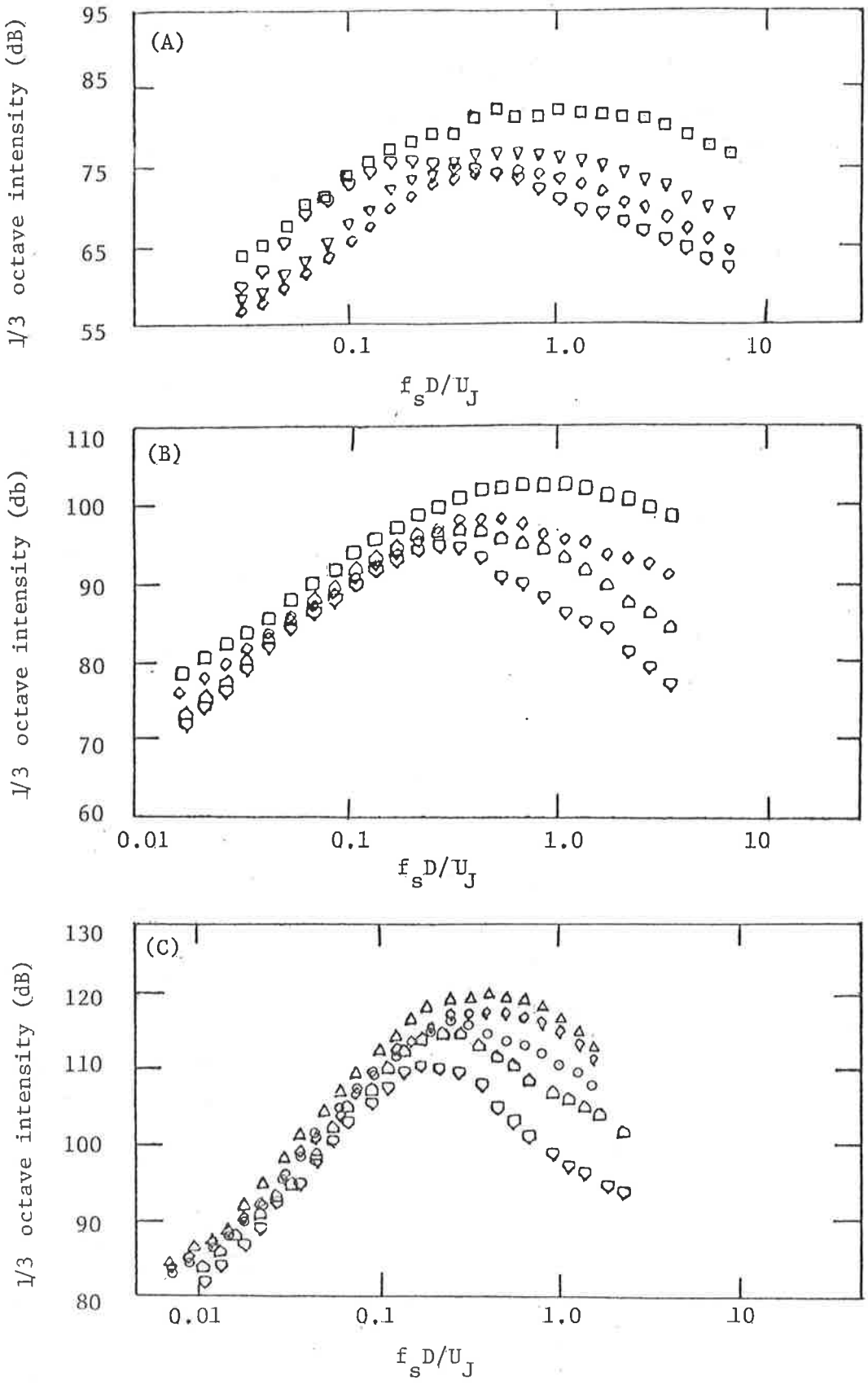

Fig. 4.10 Measured one-third octave spectra for various jet densities at $\theta = 45^{o}$

(A) $U_J/a_o \simeq 0.5$; □, B3; ▽, C2; ◇, D2; ▽, F2

(B) $U_J/a_o \simeq 1.0$; □, G1; ◇, D4; △, E4; ▽, F4

(C) $U_J/a_o \simeq 1.5$; △, G2; ◇, G5; ○, G3 ; △, G8; ▽, F5

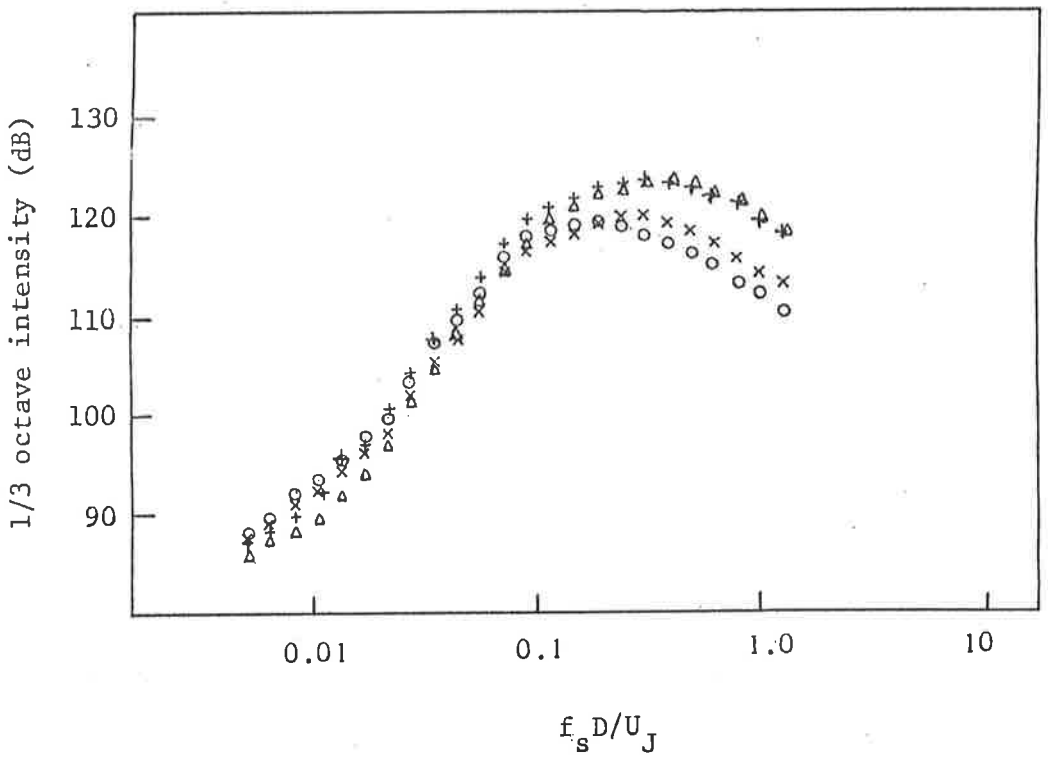

Fig. 4.10(D) Measured one-third octave spectra for various jet density at $\theta = 45^o$

($U_J/a_o \simeq 2.0$; Δ, G4 ; +, G6; X, G7; o, G9)

previous experiments (D1, D2, D5, D6). From the plots it can be seen that the peaks of the spectra become more pronounced with increasing velocity and decreasing density. For the same jet exit velocity, the peak Strouhal number ($f_s D/U_J$) is higher for denser jet. Similar trends are also observed in the case of hot jets as shown in Fig. 4.11 which is reproduced from the work of Tanna et al (D2) where the one-third octave spectra of various jet temperatures at $U_J/a_o = 0.5, 0.9, 1.47$ at $\theta = 45^o$ were measured. It is however, not appropriate to examine and compare spectra from jets of different densities on the $f_s D/U_J$ frequency scale since it is not universal as discussed in section 4.2.1. The earlier measurements have shown that the convection velocity is very much dependent on jet density and thus correct Doppler shifting of the measured frequency f to source frequency f_s can only be obtained if the correct U_c is used. Thus

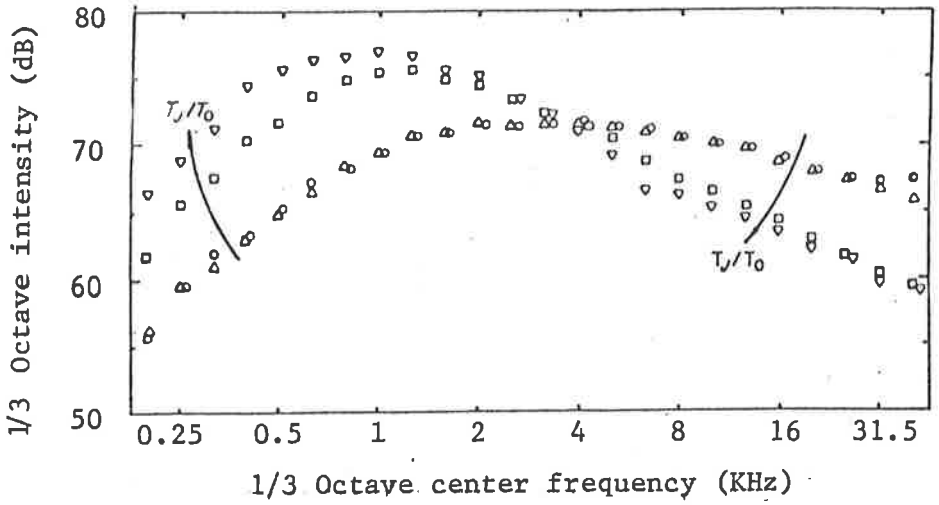

Fig. 4.11(A) Effect of T_J/T_o on 1/3 octave spectra at jet velocity $U_J/a_o = 0.5$; $\theta = 45^o$
(Δ, $T_J/T_o = 0.95$; o, 1.0; $\square$, 2.3. ∇, 3.4)
[Reproduced from Tanna [D2] Fig. 10.]

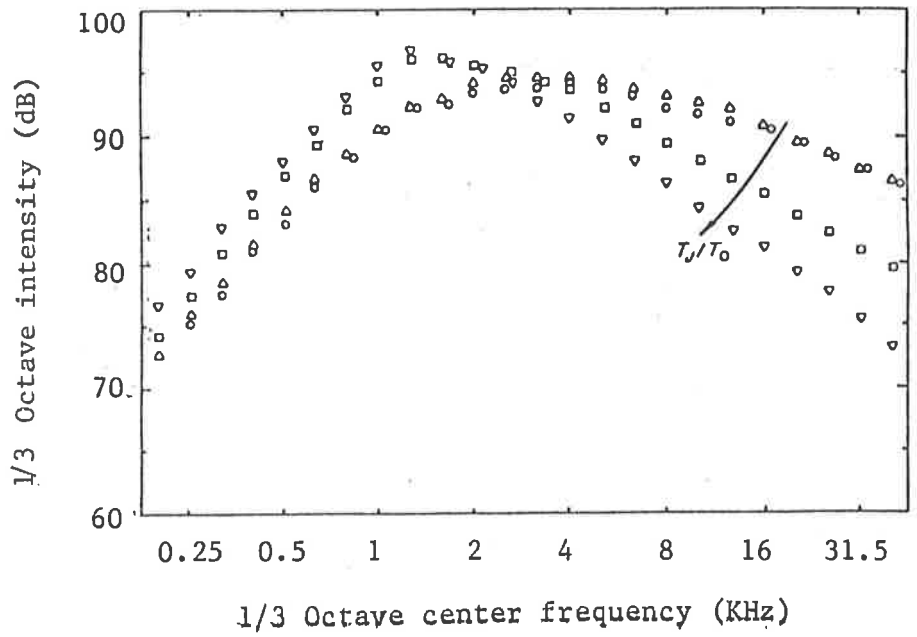

Fig. 4.11(B) Effect of T_J/T_o on 1/3 octave spectra at jet velocity $U_J/a_o = 0.9$; $\theta = 45^o$
(Δ, $T_J/T_o = 0.84$; o, 1.0; $\square$, 2.3; ∇, 3.4)
[Reproduced from Tanna [D2] Fig. 11]

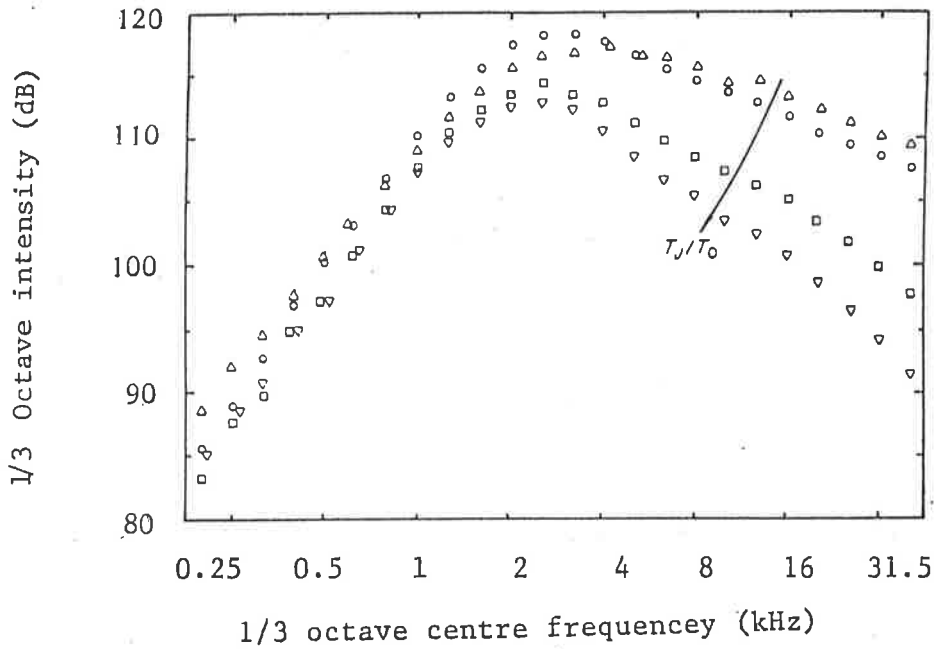

Fig. 4.11 (C) Effect of T_J/T_o on 1/3 octave spectra at jet velocity U_J/a_o = 1.47; $\theta = 45^o$
(Δ, T_J/T_o = 0.57; o, 1.2; $\square$, 2.3; ∇, 3.4)
[Reproduced from Tanna [D2] Fig. 12.]

when the data are plotted on the frequency scale $f_s D/U_c$, based on the flow convection speed a much better collapse of the spectra is obtained as shown in Fig. 4.12. At high velocities of U_J/a_o = 1.0 1.5 and 2.0 in Fig. 4.12(B), Fig. 4.12(C) and Fig. 4.12(D) the spectra nearly exhibit parallel stacking with the peaks occuring at nearly the same normalised frequencies. In low velocity where non-uniform density jets have been reported to be noisier, it is interesting to note in Fig. 4.10(A) where U_J/a_o = 0.5 that relative to the constant density jet, the one-third octave intensities of ρ_J/ρ_o = 0.2 jet are higher at the low frequency end and lower at the high frequencies. This behavior was also reported by Tanna (D2) in his hot jet measurements. However, for the same velocity the spectra from denser jets appear to exhibit parallel stacking with the constant density jet spectrum. When the results in the Fig. 4.10(A) are again plotted on the $f_s D/U_c$ scale, as in Fig. 4.13, with the one-third

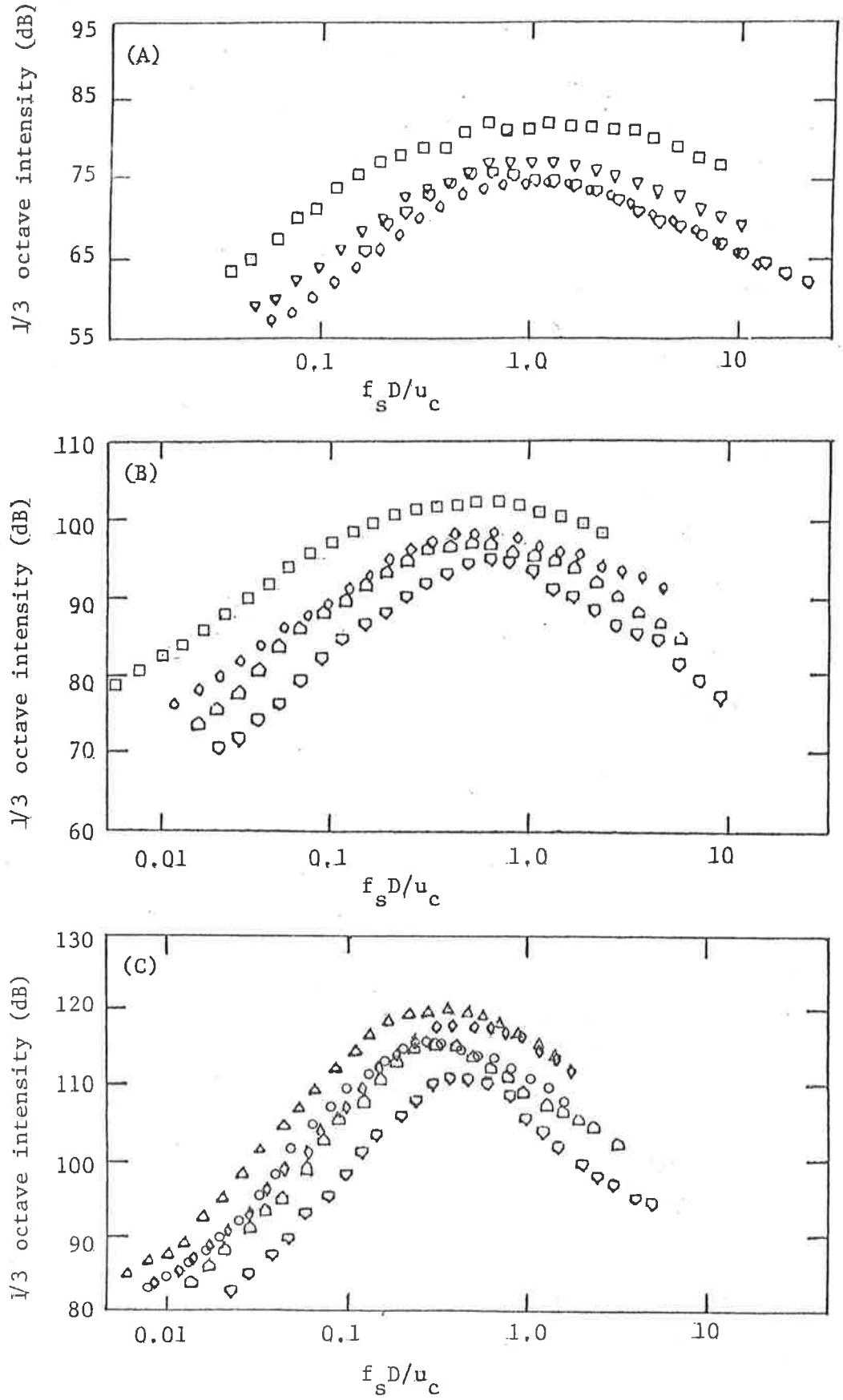

Fig. 4.12 Normalised frequency spectra for various jet density at $\theta = 45^{o}$

(A) $U_J/a_o \simeq 0.5$; □, B3; ▽, C2; ◇, D2; ▽, F2

(B) $U_J/a_o \simeq 1.0$; □, G1; ◇, D4; △, E4; ▽, F4

(C) $U_J/a_o \simeq 1.5$; △, G2; ◇, G5; ○, G3; △, G8; ▽, F5

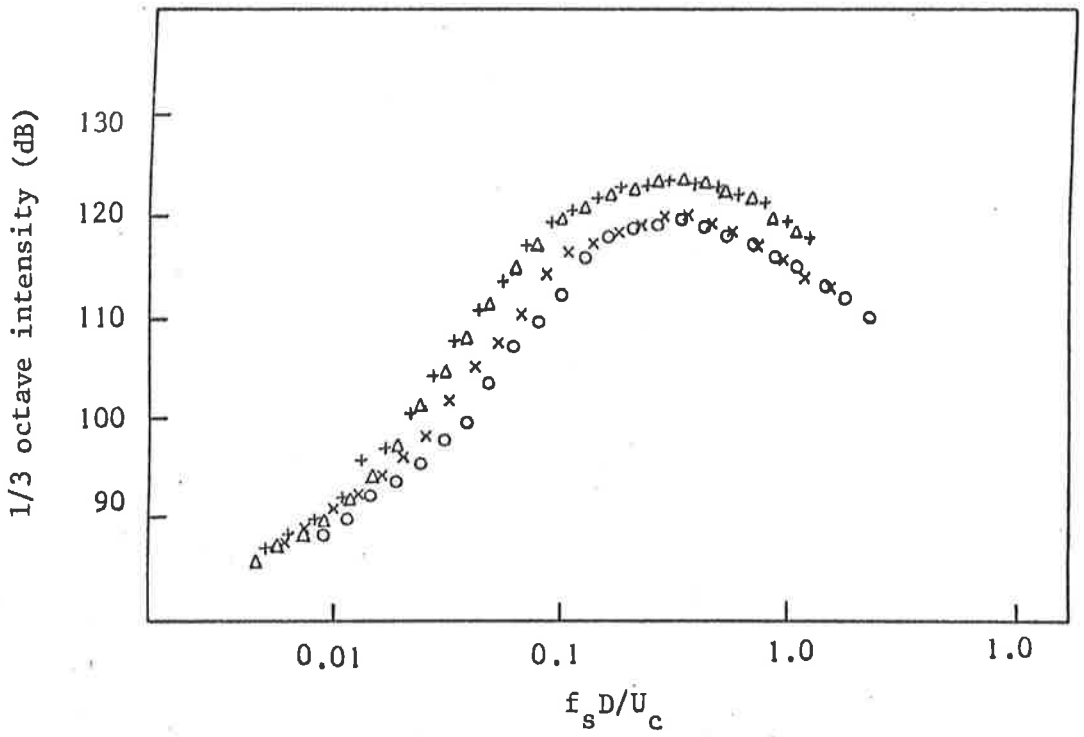

Fig. 4.12 Normalised one-third spectra for various jet densities at $\theta = 45^o$

(D) $U_J/a_o \simeq 2.0$; Δ, G4; +, G6; x, G7; o, G9

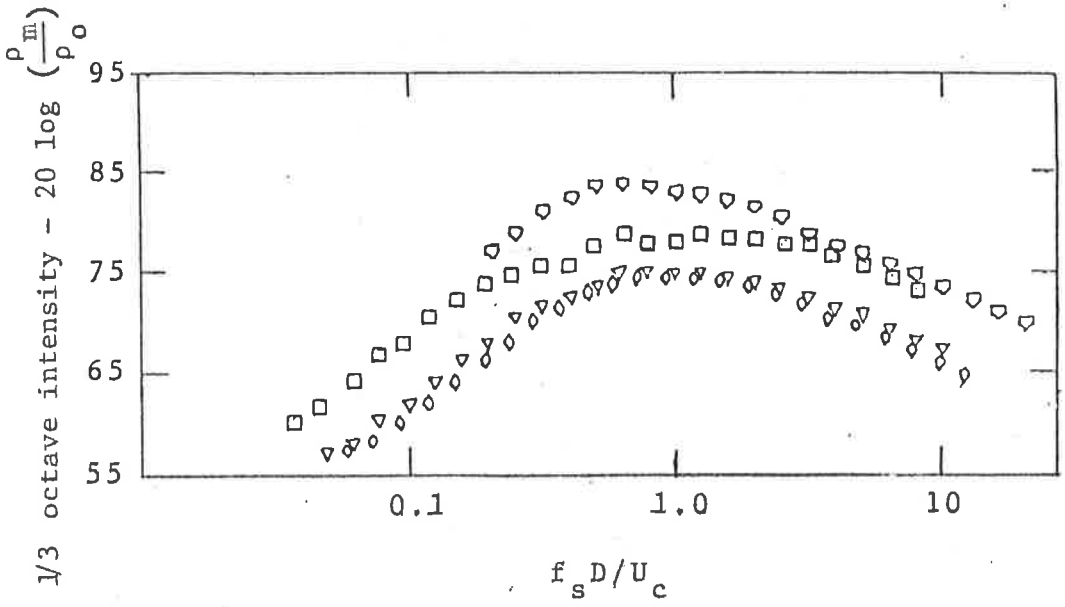

Fig. 4.13 Normalised spectra for various jet density at $\theta = 45^o$: $U_J/a_o \simeq 0.5$; □, B3; ▽, C2; ◇, D2; ▽, F2

octave intensities normalised by their respective source densities ρ_m/ρ_o as given in equation (4.6), the spectra peak at almost the same Strouhal number and the non-uniform density jets are observed to have higher intensities at all 1/3 octave bands.

The better spectral collapse using the frequency parameter Strouhal number ($f_s D/U_c$) is demonstrated by the variation of the peak Strouhal number $(f_s D/U_c)_p$ with jet velocity at $\theta = 90^o$, 45^o and 30^o. In Fig. 4.14, at $\theta = 90^o$ $(f_s D/U_c)_p$ varies between the value of 1.1 and 1.9 over a density range ρ_J/ρ_o of 0.2 to 4.0 and velocity range U_J/a_o of 0.2 to 2.4. This is a much smaller spread compared to the hot jet data where the Strouhal number based on the peak frequency, jet exit velocity and nozzle diameter, varies between 0.5 to 1.6 over a temperature range T_J/T_o of 0.5 to 3.5 and velocity range U_J/a_o of 0.4 to 2.55 as shown in Fig. 4.15. In the latter case, the parameter $f_s D/U_J$ appears to be temperature dependent while $f_s D/U_c$ in this study is weakly density dependent.

At smaller angles to the jet axis the decreasing peak Strouhal number with velocity is possibly due to the reduction in convective amplification of the high frequency sound as discussed in section 4.3.2. As in the constant density case, marked decrease in peak Strouhal number is observed when Mach waves are radiated as the local Mach number of the flow is supersonic.

4.4.2 COMPARISON WITH MORFEY'S PREDICTION SCHEME

Morfey's jet noise prediction scheme is based on a theoretical quadrupole/dipole source model in conjunction with the geometric radiation model. His source model represents the turbulence as a volume displacement distribution of quadrupole order for isothermal jets, and for hot jets the increase in intensity at low velocity, as a result of scattering of the turbulent pressure fluctuation within the

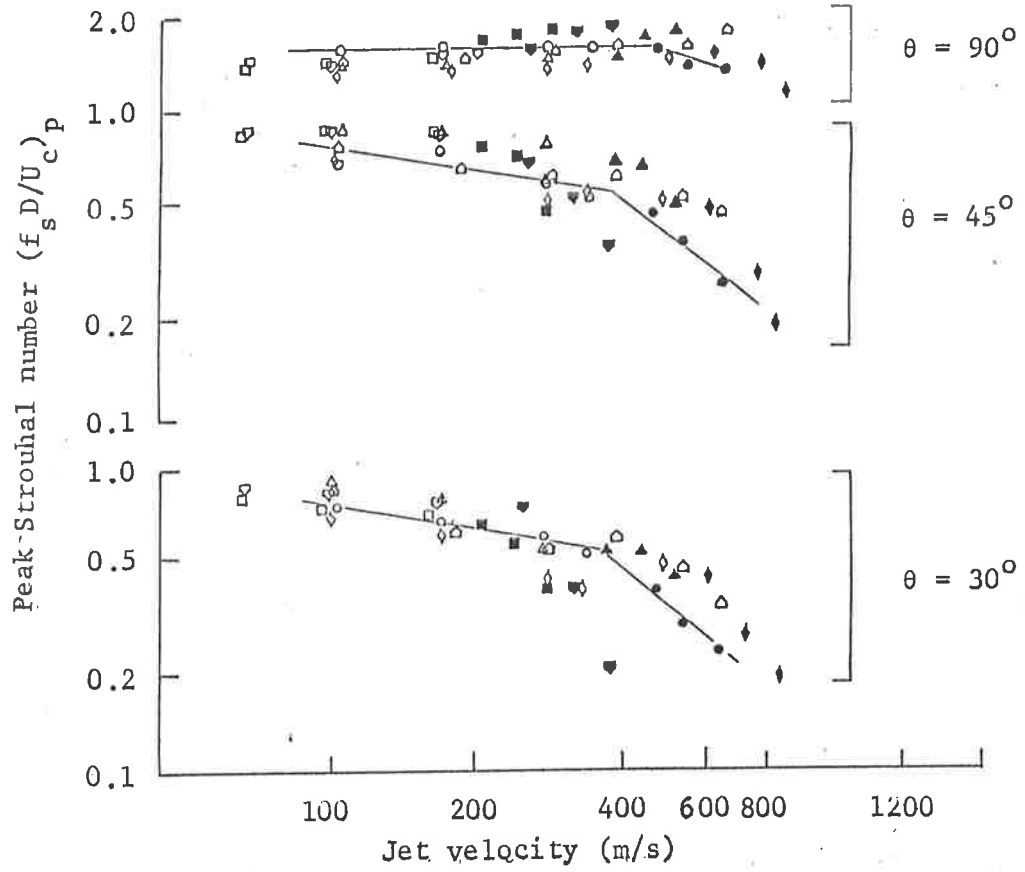

Fig. 4.14 Variation of peak Strouhal number with jet velocity at various angles of observation

(ρ_J/ρ_o : □, 4.0; ▽, 2.5; △, 1.5; ○, 1.0; ◇, 0.6; ⌂, 0.2)

open symbols - convergent nozzles
close symbols - convergent-divergent nozzles

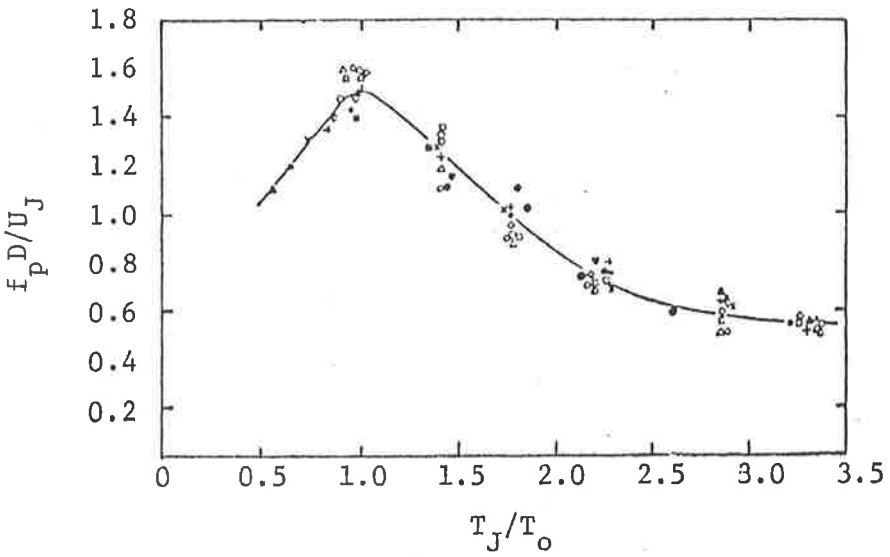

Fig. 4.15 Variation of peak frequency with jet velocity and temperature: θ = 90°
U_J/a_o: ○, 0.4; △, 0.5; □, 0.6 ◇, 0.7; ▽, 0.8 ; +, 0.9 ; ×, 1.16; ●, 1.33; ▲, 1.47 ; ■, 1.65; ◆, 1.80; ▼, 2.00; ✚, 2.30; ⬟, 2.55 .

[Reproduced from Tanna [D2] Figure 14.]

flow, is modelled as an additional source of a volume displacement distribution of dipole order. The jet noise prediction scheme is developed from the source master spectra, directivity factor and turbulence parameter obtained from the analysis of the acoustic data of Tanna et al (D2) on isothermal and hot jets.

Morfey's computer programme which can predict mixing noise for an ideally expanded air jet of varying velocity and temperature at angles and positions outside the cone of silence is modified to predict noise radiation from jets other than air. The modification is done in accordance to Morfey's suggestions (for detail see (C11)). The turbulence scaling parameters, which are temperature dependent in the original programme for hot jets, become density dependent as density is now the quantity which is influencing the spatial evolution of the flow turbulence.

From his assumption that the stagnation temperature profile is similar to the velocity profile and also that the mass fraction of the exhaust gas follows the same distribution as the stagnation temperature, the source temperature and hence the source density, the ratio of the specific gas constant and their downstream variations can be estimated. Using the perfect gas relationship the source/ambient speed of sound ratio (a_s/a_o) and the source/ambient density ratio (ρ_s/ρ_o) can be calculated.

Morfey's prediction scheme is valid for radiation angles greater than 30^o to the axis at all velocities and prediction inside the cone of silence is possible provided $U_J/a_o < 1.0$. This puts a limitation on the prediction capability at high velocity since the cone of silence increases with jet velocity. From his definition, $\cos \theta_c < a_o/(a_s + U_s)$ where θ_c is upper limit of the cone and a_s and U_s are the speed of sound in the source region and the source

convection speed respectively. An example from Morfey (C11) is that for $T_J/T_o = 3.0$ ($\rho_J/\rho_o = 0.33$) at $U_J/a_o = 1.7$, the cone of silence is 66^o. Therefore in this work the comparison between the predictions and the measured data is made mainly at $\theta = 90^o$, particularly at high velocities.

The velocity dependence of the overall intensity at $\theta = 90^o$ is shown in Fig. 4.16. At $\rho_J/\rho_o = 1.0$, the predicted levels are within 2 dB of the measured levels over the range of velocity considered with closer agreement at high velocity. For non-uniform density jets there is, in general, a tendency for the scheme to overpredict at low velocity. While the agreement is within 2 dB for flows where $U_J/a_o > 1.0$, discrepancies as high as 4 dB are observed in flows where $U_J/a_o < 1.0$.

The predictions of spectra at $\theta = 90^o$ and $\theta = 45^o$ are illustrated in Fig. 4.17 and Fig. 4.18, where the predicted spectra restricted to about sixteen one-third octave bands, are compared with measurements obtained at various velocities and densities. At $\theta = 90^o$ the agreement is remarkable for U_J/a_o of 1.0, 1.5 and 2.0 as shown in Fig. 4.17(B), Fig. 4.17(C) and Fig. 4.17(D) respectively. The predicted spectra are very close to the measured spectra with the discrepancies in the one-third octave intensities of less than 5 dB at the worst. for $U_J/a_o = 0.3$, the agreement is poorer particularly for the heavier jets where the scheme overpredicts by as much as 5 dB as in test point B2. At $\theta = 45^o$, as shown in Fig. 4.18, agreement is not as good on the whole. Again, overprediction is observed for dense jets at low velocities. At this angle, there are discontinuities observed in some of the predicted spectra (eg. Fig. 4.18(E) and Fig. 4.18(F)). This occurs when some of the one-third octave bands of the spectra are within the cone of silence and the rest of the bands are outside.

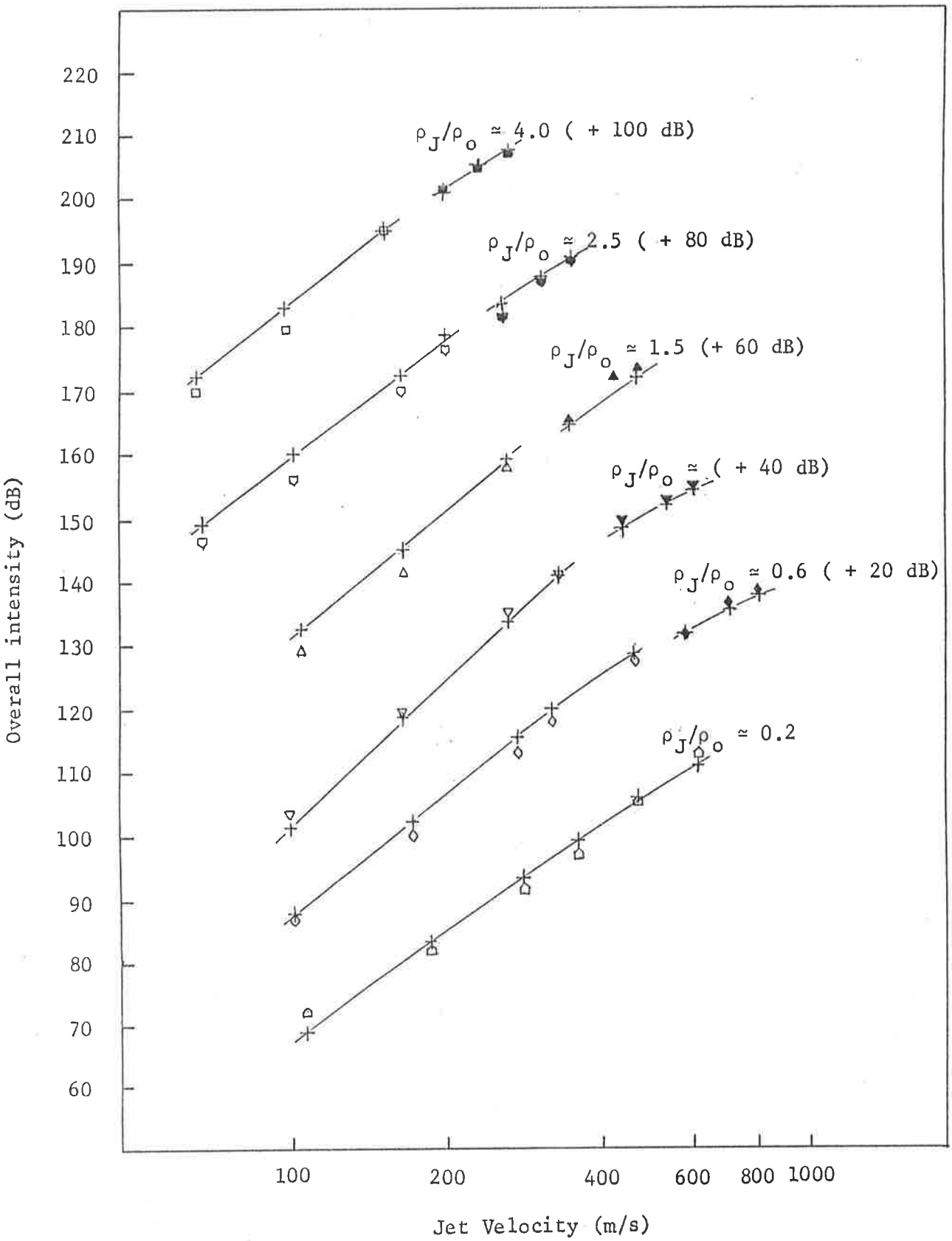

Fig. 4.16 Comparison between measured intensities and Morfey's prediction at $\theta = 90^o$

(measured data; □, ρ_J/ρ_o = 4.0, ▽, 2.5; △, 1.5; ▽, 1.0; ◇, 0.6; △, 0.2, +, Morfey's prediction)

(Close symbols for convergent-divergent nozzles and open symbols for convergent nozzles)

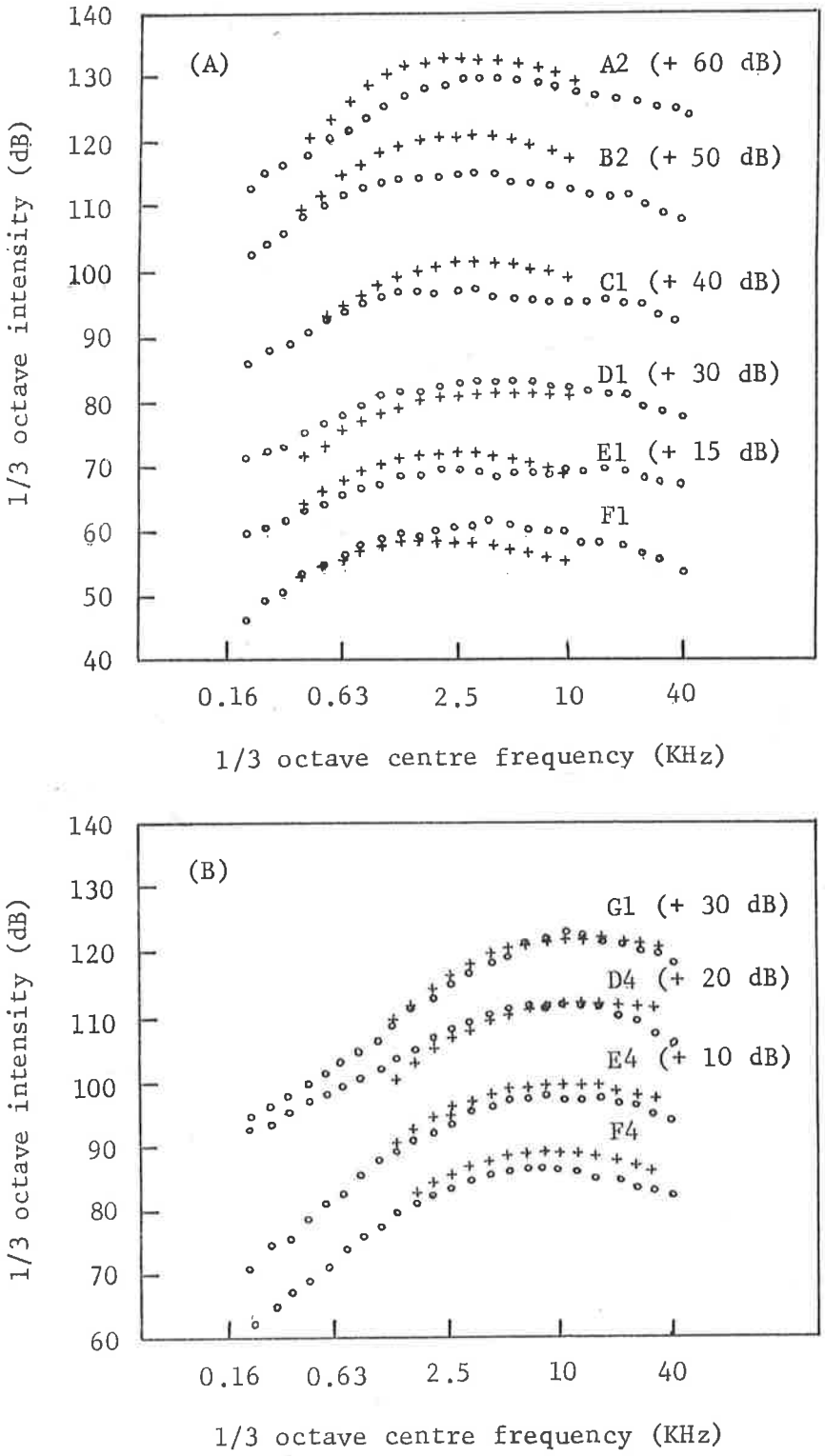

Fig. 4.17 Comparison between measured spectra and Morfey's prediction; $\theta = 90^{o}$

code : o, experiment; +, prediction

(A) A2; (U_J/a_o = 0.283, ρ_J/ρ_o = 3.833); B2, (0.303, 2.450); C1, (0.314, 1.464); D1, (0.296, 1.000); E1, (0.301, 0.594); F1, (0.316, 0.199)

(B) G1, (U_J/a_o = 1.055, ρ_J/ρ_o = 2.030); D4, (0.995, 1.001); E4, (0.995, 1.001); F4, (1.090, 0.100)

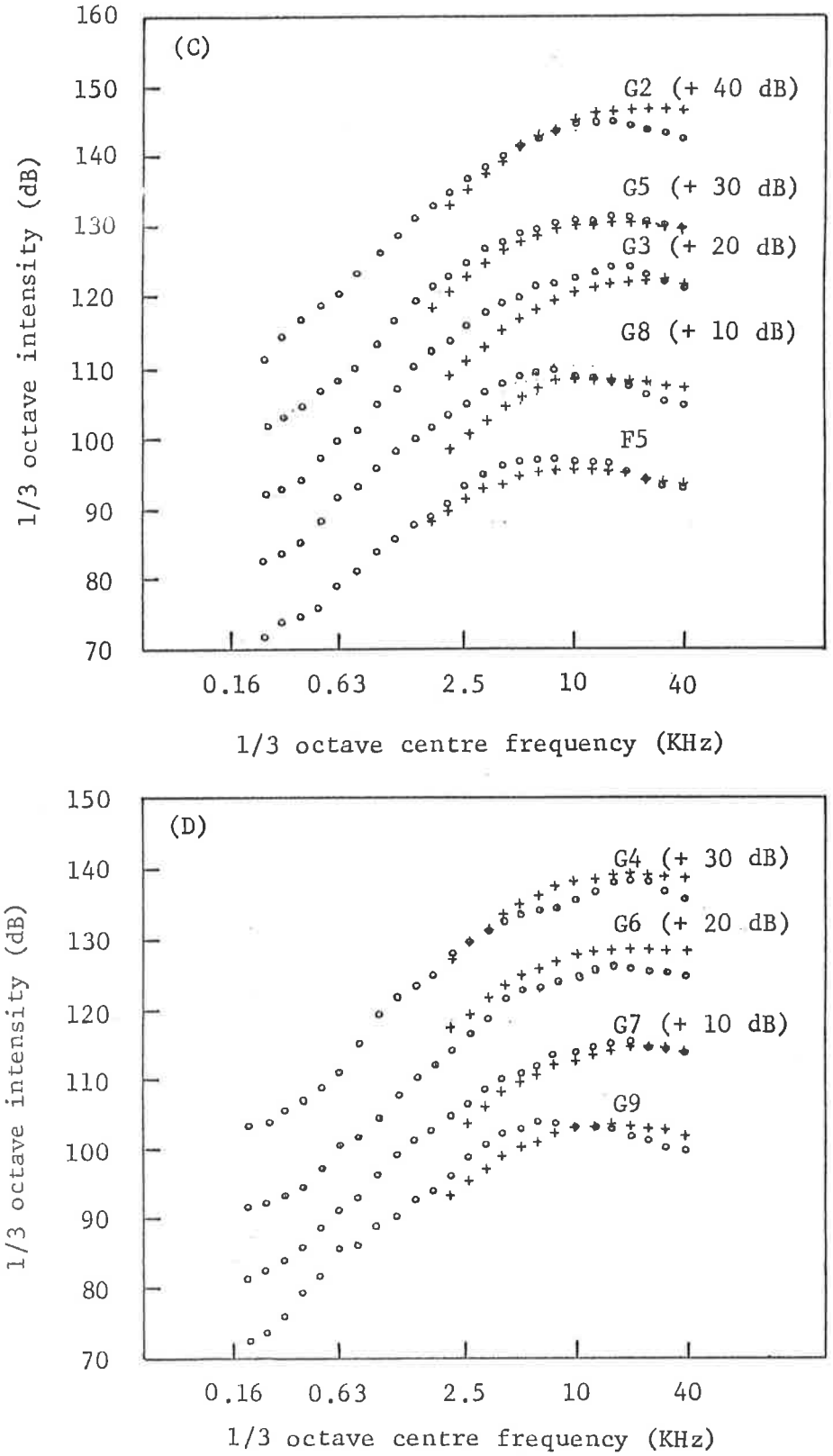

Fig. 4.17 Comparison between measured spectra and Morfey's prediction; $\theta = 90^{o}$

Code : o, experiment; +, prediction

(C) G2, (U_J/a_o = 1.525, ρ_J/ρ_o = 1.358); G3, (1.553, 0.758) G5, (1.553, 0.758); G8, (1.485, 0.491); F5, (1.411, 0.197)

(D) G4, (U_J/a_o = 1.957, ρ_J/ρ_o = 0.883); G6, (2.062, 0.637); G7, (2.011, 0.481); G9, (1.916, 0.299)

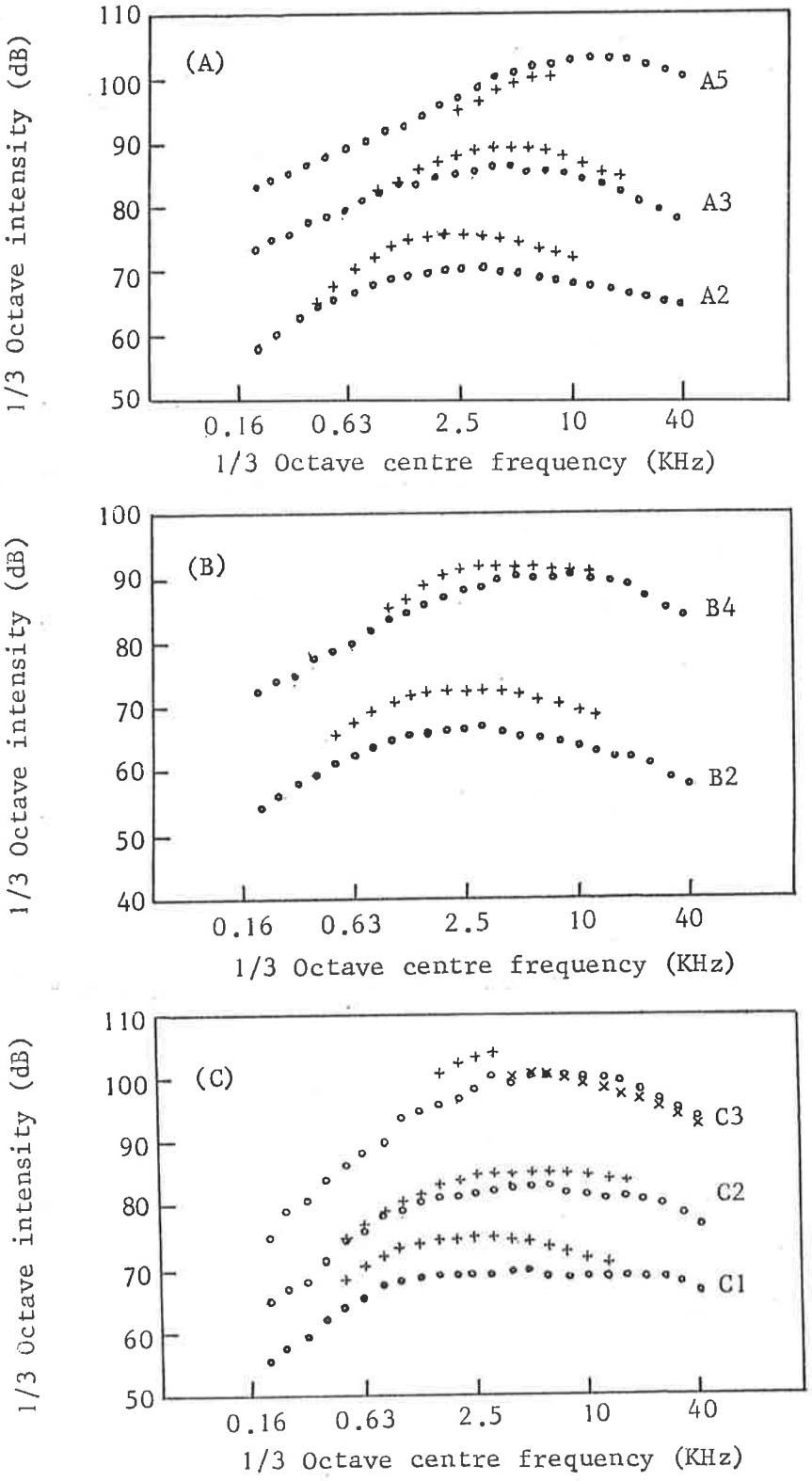

Fig. 4.18 Comparison between measured spectra and Morfey's prediction; $\theta = 45^{o}$

Code : o ,experiment; + ,prediction outside cone of silence; x ,prediction inside cone of silence

(A) A2 ,(U_J/a_o=0.283, ρ_J/ρ_o=3.883); A3 ,(0.453,4.003)
A5 ,(0.700,3.996)

(B) B2 ,(U_J/a_o=0.303, ρ_J/ρ_o=2.450); B4 ,(0.581,2.518)

(C) C1 ,(U_J/a_o=0.314, ρ_J/ρ_o=1.464); C2 ,(0.500,1.401)
C3 ,(0.791,1.499)

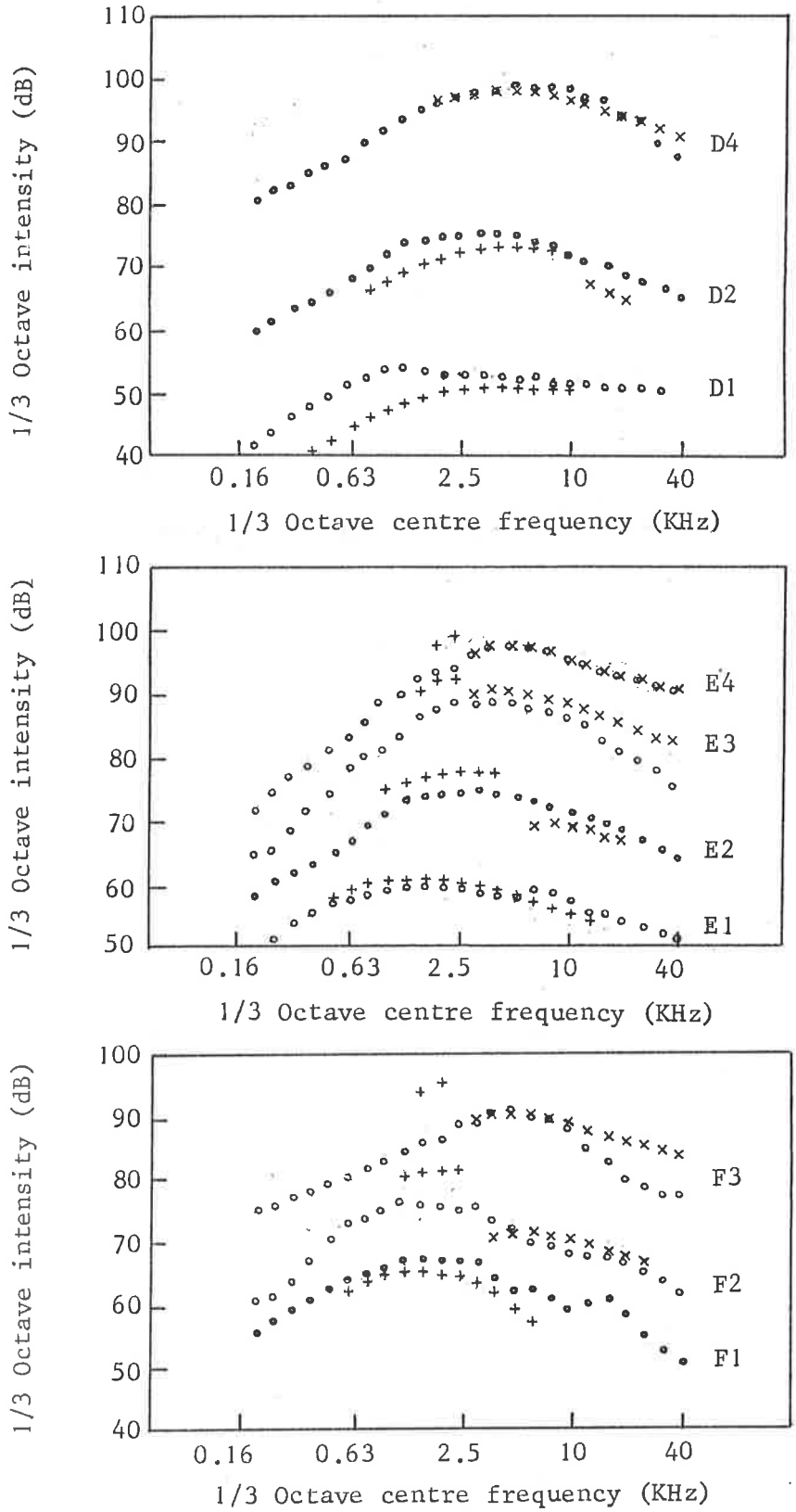

Fig. 4.18 Comparison between measured spectra and Morfey's prediction; $\theta = 45^{o}$

Code : o ,experiment; + ,prediction outside cone of silence; x ,prediction inside cone of silence

(D) D1 ,(U_J/a_o=0.296, ρ_J/ρ_o=1.000); D2 ,(0.490,0.994)
D4 ,(0.955,1.001)

(E) E1 ,(U_J/a_o=0.301, ρ_J/ρ_o=0.594); E2 ,(0.517,0.599)
E3 ,(0.826,0.595); E4 ,(0.979,0.595)

(F) F1 ,(U_J/a_o=0.316, ρ_J/ρ_o=0.199); F2 ,(0.549,0.199)
F3 ,(0.841,0.203)

In these cases, the predictions inside the cone of silence appear to agree with the measurements better, as illustrated in Fig. 4.18(E) and Fig. 4.18(F).

The good agreement between the measurments and the predictions over such a large range of density and velocity demonstrates the validity of the prediction scheme which assumes an additional noise source in non-uniform density jet whose intensity scales as $U_J^{6.0}$. The scheme, although devised/based on the hot jet data, is shown to be able to predict noise from jets whose working fluids are gases other than air when appropriate modifications, in accordance with Morfey's suggestions, are made in the computer programme.

4.5 The effects of nozzle geometry on the radiated noise

The bulk of jet noise studies over the years has concentrated on the noise from circular jets as this has been the jet engine exhaust configuration of principal interest. Recent jet noise suppression techniques have sought to modify the noise by altering the source intensity, location and spectrum. One method of such source modification is to alter the nozzle exit geometry. But none of the existing theories and models can confidently predict the effects of nozzle exit geometry on the noise radiated and the available experimental results on the noise from 2-D nozzles are fragmentary and contradictory. In this study the acoustic characteristics of turbulent air jets from 2-D nozzles are examined and compared with those of a round jet. As discussed earlier, the velocity dependence of jet noise varies from one experimental rig to another. As shown by Banerian [D10] when the turbulence level at the nozzle exit plane is increased the measured acoustic power increases, particularly at low Mach numbers. Since the jets in

the present experiments are produced by the same flow system through a range of carefully designed nozzles, the effects of exit geometry can be more reliably deduced.

In chapter 3, the similarity of the flow structures in the initial mixing region of a round jet and a 2-D jet has been discussed. For nozzles having the same exit area, the effective length of the potential core in a 2-D jet decreases with nozzle height H as shown in Fig. 4.19.

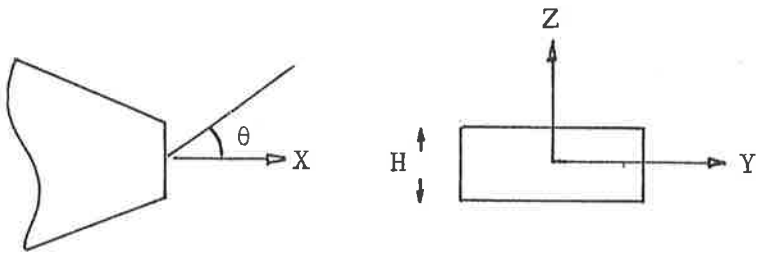

Fig. 4.19 Jet coordinate system

In this study only subsonic jets, $U_J/a_o < 1.0$, are considered and the acoustic radiation is measured on the principal planes of $\phi = 0^o$ and $\phi = 90^o$, at emission angle θ varying from 20^o to 90^o. The 2-D nozzles used have the same exit area of 6.5×10^{-4} m^2 but different aspect ratios of 1, 6 and 25.

The overall intensities of the 2-D jets at $\theta = 90^o$ on the principal planes of $\phi = 0^o$ and $\phi = 90^o$ are presented in Fig. 4.20 together with that of a circular nozzle of the same exit area. At a fixed velocity, the scatter in the overall intensity is within 1-2dB. While the intensities at the principal plane $\phi = 0^o$ are marginally lower than those measured in the round jet, the intensities at $\phi = 90^o$ are seen to be higher so that on any y-z

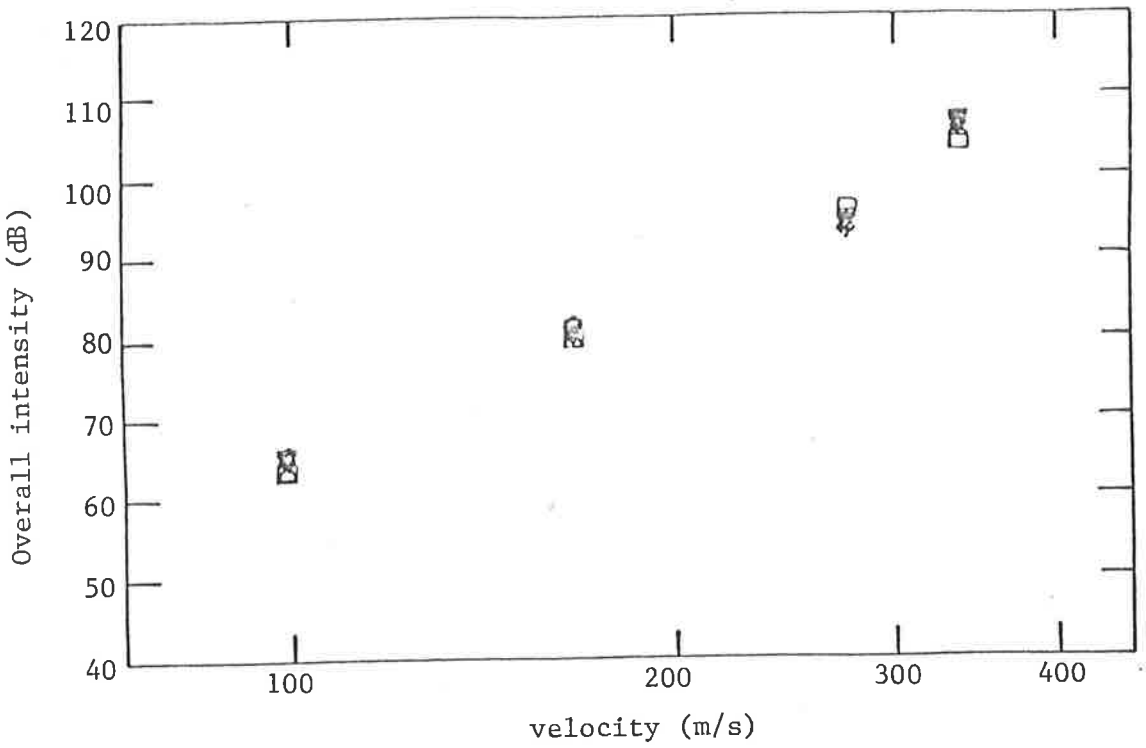

Fig. 4.20 Velocity dependence of the overall intensity at $\theta = 90^{o}$ (□, Round; Δ, square, ∇, aspect ratio 25:4; ◇, 25:1; open symbol, $\phi = 90^{o}$; closed symbol, $\phi = 0^{o}$)

plane the circumferential directivity assumes a characteristic 8 - lobe pattern. However, over the velocity range and for the range of nozzle aspect ratios considered, the largest differences between intensities on the two principal planes occurs for the highest aspect ratio jet where the difference is of the 3-4 dB. This suggests that in practical terms only minimal benefit could be gained by reorientating the major axis of a 2-D jet nozzle from horizontal during take-off to vertical after take-off, as suggested by some as a mean of reducing aircraft fly-over noise, though the effect of jet-mean flow interactions and jet-jet interactions can affect this conclusion.

The effect of nozzle exit geometry on the noise spectrum is illustrated in Fig. 4.21. The nozzle shape is shown to modify the energy content in the various frequency bands of the spectrum. The increase in aspect ratio shifts the sound energy towards higher frequencies. The frequency at which the peak occurs is seen to

increase with decreasing nozzle height or diameter regardless of the circumferential position ϕ.

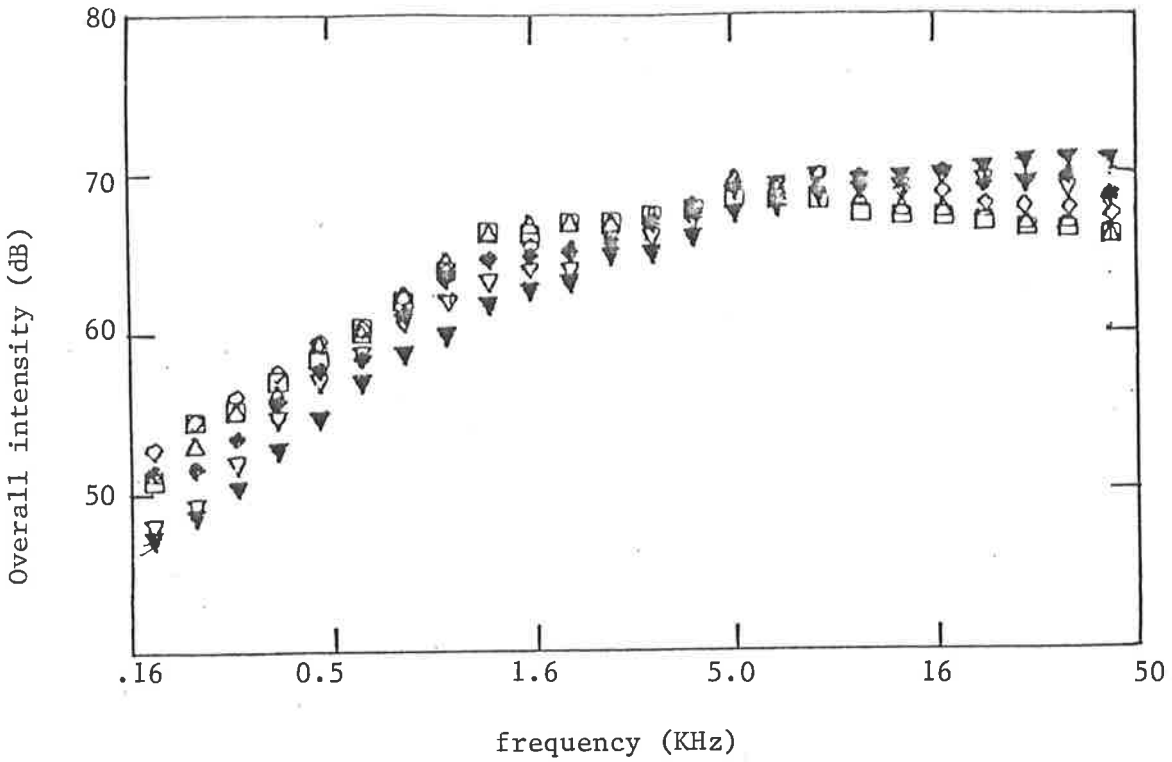

Fig. 4.21 Effect of nozzle exit geometry on the 1/3 octave spectra.
(For symbols description see Fig. 5.29)

The variation of the overall intensities with θ in each of the principal planes $\phi = 0^{o}$ and $\phi = 90^{o}$ at $U_J/a_o = 0.5$ is presented in Fig. 4.22. For a small aspect ratio jet, the directivity patterns are nearly identical to those of the axisymmetric jet. For nozzles of high aspect ratio (25:1), a significant reduction in intensity at angles close to the jet axis is observed relative to a round jet. As we shall see later the spectrum of a jet from a 2-D nozzle is biased towards the higher frequencies with the peaks scaling roughly with the nozzle height. Since the acoustic-mean-flow interaction is more significant for high frequency noise at small angles a higher reduction in intensity is expected for a jet from a high aspect ratio 2-D nozzle.

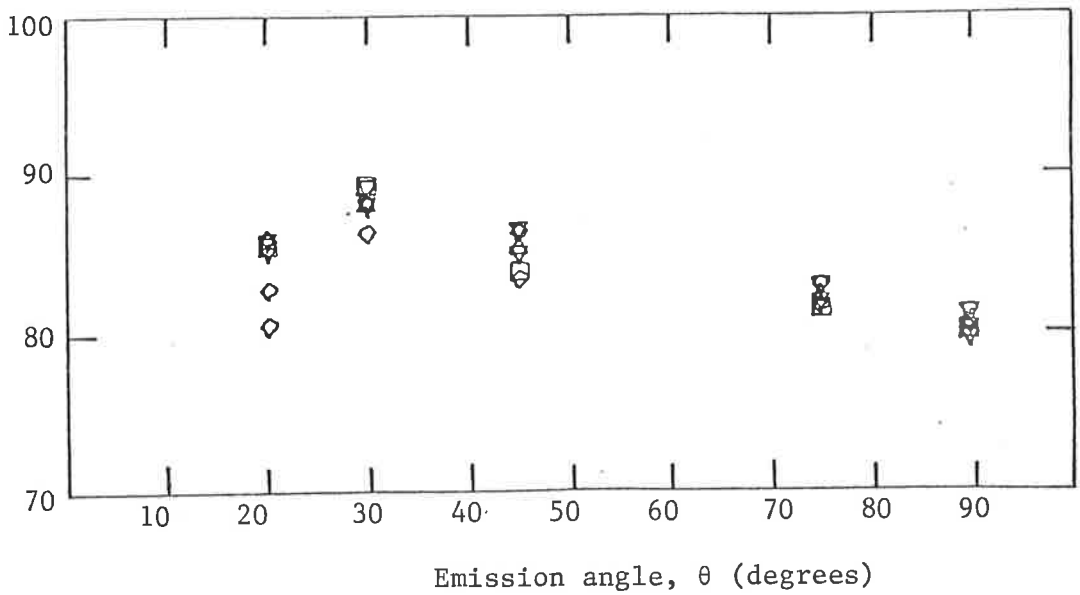

Fig. 4.22 Effects of nozzle exit geometry on the directivity pattern. (For symbol description see Fig. 5.24)

The conclusion based on these observations is that the flow structures are not greatly modified by the change of exit geometry from round to rectangular. The resulting noise radiated at subsonic flow shows that although the polar directivity exhibits the 8-lobe pattern, the difference in intensity between the principal planes is not significant. For 2-D jets, lower intensities at smaller angles are observed only if the aspect ratio is high. In the 1/3 octave spectra, the change in exit geometry merely redistributes the energy content in the 1/3 octave bands. On the whole the 2-D nozzles do not appear to offer real suppression for jet exhaust noise.

5.1.1 A PROPOSED SOURCE MODEL FOR NOISE GENERATION

As seen in Section 3.1.2, the pressure fluctuations in the entrainment region are dominated by the amalgamation processes, which seems to lend support to the suggestions of Laufer et. al (C1) and of Browand and Winant (A3) that the abrupt process of vortex amalgamation is a primary mechanism for jet noise generation. Laufer et. al have postulated an acceleration and deceleration of the structures in a round jet preceding pairing wherein the leading vortex ring expands and slows down while the succeeding vortex ring contracts and speeds up to overtake from the high speed side of the mixing layer. In the process the vortices spin around each other and finally amalgamate to form a larger vortex. This relatively rapid and large scale motion, they argue, must be an efficient process of noise production. However, they did not quantify the noise generation for such a model.

Powell (B10) and Stuber (C13) have shown in their analyses that a pair of vortices rotating about a fixed axis radiate sound whose intensity varies as $U_J^{8.0}$ or $U_J^{7.0}$ for two-dimensional vortices.

The flow field of a pair of opposing dipoles separated by a distance L_s is shown in Fig. 5.1. In the far field where the distance of observation R is large compared to L_s (i.e. $L_s/R << 1.0$) the dipole pair degenerates into a quadrupole.

Now consider two successive vortices convecting downstream at a speed U_c preceeding an amalgamation process as in Fig. 5.2. The fluid from the potential core is drawn into the mixing layer at the leading ends of the structures while ambient fluid is entrained at the trailing ends. The thick lines represent the boundaries of interfaces of the vortices and the arrows are indications of the streamlines of the irrotational fluids being entrained into the

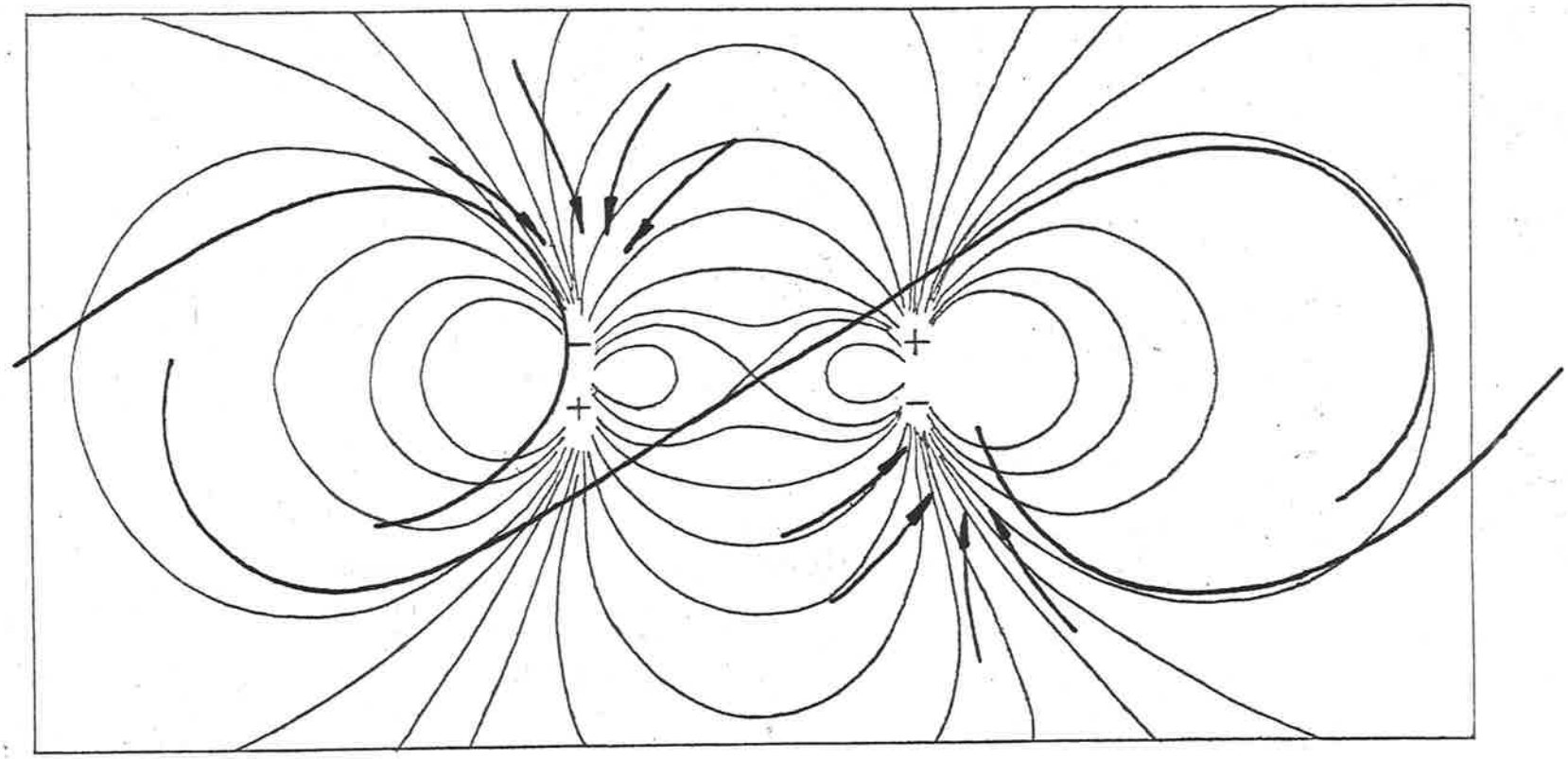

Fig 5.1 Streamline pattern of a dipole-pair
Fíg. 5.2 Schematic diagram of the flow in between two vortices.

mixing layer.

On entering into the core of the structure the fluid from either the potential core or the ambient region appears to converge to a point which locally looks like a portion of a flow resulting from a source and sink pair. By superimposing Fig. 5.2 on Fig. 5.1, it can be seen that although the flow fields are not exactly the same in the near field the main feature of the rotating flow is rather similar. Thus a model is proposed in which the strengths of the opposing dipole pair are approximated by the entrainment rates of the irrotational ambient fluids. With this rather simple, yet physically realistic model the observed density dependence of the radiated noise can be explained.

From the mixing layer model the entrainment rates of the ambient fluids $\bar{\lambda}_i$ ($= \frac{\bar{V}_{ei}}{U_J}$ where $\bar{V}_{ei}$ is the average entrainment velocity) in jet flow for different density ratios can be calculated from equation (7.10) which are tabled below.

ρ_J/ρ_o	$\bar{\lambda}_J/(\bar{\lambda}_J + \bar{\lambda}_o)$	$\bar{\lambda}_o/(\lambda_J + \bar{\lambda}_o)$	$\lvert\bar{\lambda}_o - \bar{\lambda}_J\rvert/(\lambda_J + \bar{\lambda}_o)$
0.2	0.725	0.275	0.450
0.6	0.576	0.424	0.152
1.0	0.5	0.5	0
1.5	0.439	0.561	0.122
4.0	0.303	0.697	0.394

Table 5.1 Variation of entrainment rate with jet density.

In a constant density jet the entrainment rates on each side of the shear layer are equal giving an exact cancellation of the dipole-pair which results in only quadrupole radiation. In the non-uniform density jet on the other hand, the entrainment rates are unequal as shown in Table 5.1, which lead to unequal dipole strengths. The

radiation is then not only from the quadrupole, but also from the uncancelled residue of the dipoles.

The dipole, whose strength varies as $|\overline{\lambda}_J - \overline{\lambda}_o|$, is stronger the more the jet density differs from ambient. Being a more efficient noise source than the quadrupole, it dominates the far field noise for non-uniform density subsonic jets, as observed experimentally.

This model is also in agreement with Lighthill's idea. The amalgamation process, which is responsible for the large entrainment (which is proportional to the dipole strength) is also found to be responsible for a significant part of the Reynolds stress production, as evident in the work of Browand and Weinman (A4). Their Reynolds stress measurement showed that the production was the highest in the intermediate stage of the amalgamation process. In the analysis of Brown and Roskho (A1), the Reynolds stress u'v' is estimated to scale with the entrainment rate, which according to Brown's (A2) conclusion is dependent on the velocity ratio across the mixing layer.

As observed in a frame of reference which is translating at the structure convection speed U_c, the sequences of the amalgamation process are shown in Fig. 5.3. In the process the vortices are seen to rotate about an axis between them. Upon amalgamation the dipole separation diminishes until the two structures eventually merge to form a single large vortex. In the far field where the distance of observation R is large compared to the dipole separation L_s, the dipole pair degenerates into a point quadrupole. In the stationary frame of reference an observer in the far field sees a quadrupole field which is translating and rotating so that there is no prefered orientation of the quadrupole.

In this proposed model the strength of each dipole is proportio-

nal to the entrainment rate of the irrotational fluid. In this

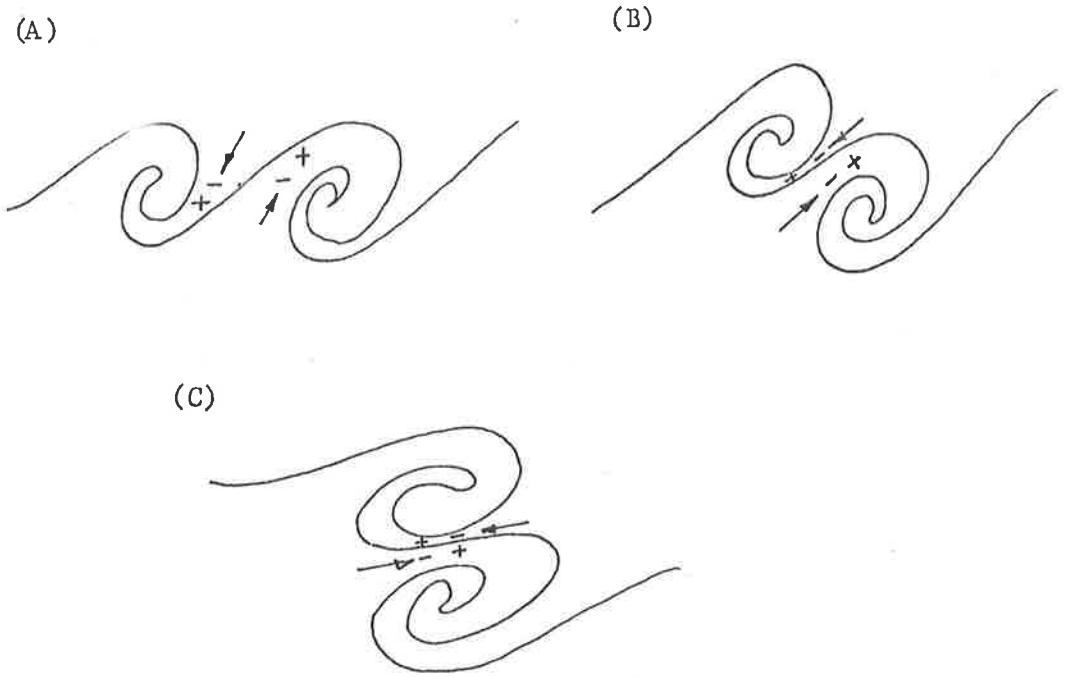

Fig. 5.3 Schematic diagrams of the amalgamation process.

case the sources, which are associated with the transient amalgamation events, grow and decay over a distance of the order of the shear layer thickness. The process occurs randomly in time and in space all along the jet mixing layer in a free unforced jet. A large structure pairs with another structure and does not appear to engage in another amalgamation until the first is completed. Each amalgamation can be treated as an independent event and these events are statistically uncorrelated. The far field is therefore the sum of all the individual sources. The growth and decay of the source function can be described mathematically as

$$T_{ij}(\underset{\sim}{y},\tau) \propto \rho U^2 \exp\left| -\frac{|\underset{\sim}{y}|^2}{\ell_c^{\,2}} - \frac{\tau^2 U_c^2}{\ell_c^{\,2}} \right| .$$

If this source function is used in Lighthill's inhomogeneous wave equation, it can be shown that the far field intensity is exactly

in accord with Lighthill's result.

The writer appreciates that this simple model is represented here with no formal mathematical derivation and the source strength is not quantified. Until the detail analysis has been done it can be used only as an aid to thinking by giving a physically realistic and experimentally compatible picture of the jet noise generation. In the absence of a better physical model it offers, in particular, an interpretation of the role of the dipole and quadrupole sources in non uniform density jets.

6. Summary and conclusions

The single exposure shadowgraphs/Schlieren pictures and high speed movies have provided direct evidence of the existence of large scale structures in the initial mixing region of a turbulent jet where a large proportion of jet noise is known to originate. In flow where the Reynolds number is lower than 4.0×10^4 these structures are seen as distinct vortices with smooth boundaries. They control the development of the mixing layer by the process of amalgamation whereby two large structures merge to form a larger one thus increasing their size and spacings of the structures. This process is accompanied by large entrainments of irrotational fluids from both the potential core and the ambient and is primarily responsible for the rapid broadening of the mixing layer.

Although masked by the fine scale turbulence at high flow speed, the structures are still recognisable visually at Reynolds number up to 2.3×10^5. At even higher speed, the existence of the structures is inferred from the near field pressure and velocity signals. From the simultaneous optical observation and near field point measurements of a low speed flow, periodic peaks and troughs in the velocity signal in the potential core are observed to be due to the induced velocity field of the passing large structure. In high speed flow while these peaks or 'spikes' in the signal appear to occur randomly in time the oscillatory nature of the autocorrelation function of the signal from a jet of Reynolds number 5.2×10^5 clearly demonstrates that hidden in the apparently chaotic flow in the shear layer of a fully turbulent jet is some large scale coherent motion. The mean period in the autocorrelation function is an indication of the spacing of these structures which are seen to increase linearly with distance downstream.

Jet density and Mach number are found to have profound influence on the convection speed of the structures and the spreading rate of the shear layer. Contrary to the widely accepted fact that the structure in the mixing layer of a jet has a speed roughly 0.63 - 0.67 times the jet exit velocity irrespective of jet density or temperature, the cross-correlation measurements show that a major effect of density is to change the convection speed of the flow structures. The measured values are found to vary with radial position as the structures are observed to be distorted, possibly by the high shear stress across the layer. As there appears to have no unique convection velocity, the mean of the values obtained in the potential core and the entrainment region is found to coincide with the value measured along the lip line which is the mean path of the vortex cores. Thus this value is taken as the mean convection speed (U_c) of the large structures. While for a constant density jet, U_c is 0.57 U_J up to the end of the potential core, it varies from 0.38 U_J to 0.72 U_J for jet density ratio (ρ_J/ρ_o) in the range of 0.17 to 4.0. Also for the same jet velocity, a lighter jet is found to have a higher visual growth rate $\Delta\delta_{vis}/\Delta x$. This higher growth rate is in fact a direct result of the slower convection speed of the large structures since the total entrainment is found to be constant for jets of the same velocity. This observation is in reasonable agreement with the mixing layer model of Brown (A2) where the total entrainment is strongly dependent on jet velocity while the relative entrainment of the irrotational fluids is strongly dependent on the density ratio.

On the velocity effect on jet noise, the overall intensity for a uniform density jet at $\theta = 90^o$ was found to obey the $U_J^{7.0}$ dependence rather than Lighthill's $U_J^{8.0}$. Deviations from the $U_J^{8.0}$ law have also been reported by many others (D1-D6) who have conducted

carefully designed jet noise experiments. In supersonic flows, a reduction in the noise intensities from the normal velocity dependence is a result of the compressibility effect which begins to affect the vortical development of the large structures, as evidenced by the significant thinning of the mixing layer. When the flow is supersonic locally, intense Mach waves are seen to radiate in the forward arc direction.

For non-uniform density jets, the velocity dependence of the overall intensity at $\theta = 90^{o}$ scales on a lower power of velocity which varies from $U_J^{5\cdot0}$ for $\rho_J/\rho_o = 0.2$ at low velocity to $U_J^{6\cdot5}$ for $\rho_J/\rho_o = 4.0$ in the range of velocity up to $U_J/a_o = 0.79$. The intensities when normalised by the respective source density ρ_m, calculated from Brown's two- dimensinal mixing layer model (A2), show that 'excess' noise is observed for all non-uniform density jets at low velocity region where $U_J/a_o < 0.6$. The intensities which scale as $U_J^{5\cdot0} - U_J^{6\cdot5}$ as opposed to $U_J^{7\cdot0}$ for uniform density case suggest that the source is likely to be dipole in character. This result lends support to Morfey's view that in a non-uniform density jet there are two sources; a quadrupole type from Reynolds stress which predominates at high velocity and its intensity scales as $U_J^{8\cdot0}$ and a dipole type from the density inhomogeneity which predominates at low velocity and its intensity scales as $U_J^{6\cdot0}$.

The other major effect of density on jet noise is associated with the variation of source convection speed with density. Correct convection speed, if assumed, enables more accurate Doppler shifting of the measured frequencies to source frequencies. It also allows more accurate predictions of the convective amplification of the noise in angles other than 90^{o}.

Realising the density dependenceof the flow convection speed, a more characteristic time for the life of the large eddies, particu-

larly in the later part of the potential core, would be scaled by D/U_c. A more appropriate frequency parameter for jet noise from the varying density jet is chosen to be $f_s D/U_c$.

The usefulness of $f_s D/U_c$ as a parameter is demonstrated by the much better collapse of the 1/3 octave spectra as against the normal $f_s D/U_J$ based on the jet velocity. At $\theta = 45^o$ the peak Strouhal number for the flow conditions in the range of $0.2 \leq \rho_J/\rho_o \leq 4.0$ and $0.3 \leq U_J/a_o \leq 2.4$ have a spread of $1.1 \leq (f_s D/U_c)_p \leq 1.9$ as compared to the hot jet result (Strouhal number based on U_J) where $0.5 \leq (f_s D/U_J)_p \leq 1.6$ over a smaller range of flow conditions (i.e. $0.4 \leq U_J/a_o \leq 2.55$ and $0.3 \leq \rho_J/\rho_o \leq 2.0$).

Compared with the published fragmentary result of noise from jets of varying composition of Lassiter and Hubbard (D9), the overall intensity at $\theta = 90^o$ is in good agreement except in the low density case where their result appears to be in error. The close agreement between the present results and the hot jet data of Tanna et. al. (D2) on the velocity and density dependence of the overall intensities and one-third octave spectra, suggests that the density change brought about by a change in compositions on one hand and a change in temperature on the other have similar effect on the noise radiated. It is therefore possible to make good estimation on hot jet noise in a laboratory by simulating the flow using gases of varying compositions.

The jet geometry offers little or no advantage on noise reduction in that the measured sound intensity and directivity for a 2-D jet (with aspect ratio of 25 : 1) are different from that of a axisymmetric jet of the same exit area by 1-2 dB. The circumferential directional distribution of the noise around a 2-D jet exhibits an 8 - lobe pattern with the highest intensity at the plane perpendicular to the nozzle width which is only 2-3 dB higher compared to that of the

round jet. The only significant difference however, the peaks of the spectra which are seen to scale with nozzle height or diameter. Thus for the spectrum of a 2-D jet the energy content is biased towards the higher frequencies relative to that of an axisymmetric jet.

The induced velocity and pressure fluctuation in the entrainment region of a jet are seen to be dominated by the amalgation processes of the large structures. Attempts to cross-correlate these signals with the acoustic far field is inconclusive as maximum correlation of 2-4% is obtained. This is not at all surprising since the near field is a point measurement and the acoustic far field is the integral effect of all the noise sources in the jet. However, when a ground plane is placed at one of the lips of a 2-D nozzle, significant correlations of more than 10% are obtained. From causality the time delay of the peak correlation indicates the noise source to be near the end of the ground plane and, since the near field signal is the induced velocity or pressure fluctuation due to the large structures, this result is interpreted as the interaction of the structures with the trailing edge of the ground plane, which produces coherent noise radiation. This experiment again demonstrates the important role of the large structures as they also govern trailing edge noise.

The abrupt amalgamation process of the large structures and its dominance of the near field pressure and velocity fluctuation is viewed as a noise source. An oversimplified but physically realistic model of jet noise generation has been proposed in which the noise source is modelled by a source-sink pair. Admittedly, the flow field of this dipole-pair is not exactly the same as the flow in an amalgamation process, the main features of the rotational flow are rather similar. This model, in which the dipole strength is proportional to the entrainment rate, can offer an explanation for the excess

noise problem. In a uniform density jet where the entrainments from either side of the mixing layer are the same, the dipoles cancel out exactly and they degenerate into a quadrupole. In non-uniform density jets unequal entrainments (hence unequal dipole strengths) lead to inexact cancellation and the result is that the far field noise appears to derive from a contribution of a dipole and a quadrupole.

References

(A) Near Field Flow Measurement

(A1) G.L. Brown and A. Roshko 1974 Journal of Fluid Mechanics 64, 775-816. On density and large structure in turbulent mixing layers.

(A2) G.L. Brown (1974) Fifth Australian Conference on hydraulic and fluid mechanics. The entrainment and large structure in turbulent mixing layers.

(A3) C.D. Winant and F.K. Browand (1974) J. Fluid Mechanics 63, 237-255. Vortex pairing : The mechanism for turbulent mixing layers growth at moderate Reynolds numbers.

(A4) F.K. Browand and P.D. Weiman (1975) Journal of Fluid Mechanics 70, Part 1. Large scales in developing mixing layers.

(A5) S.C. Crow and F.H. Champagne (1971) Journal of Fluid Mechanics 48, 547-591. Orderly structure in jet turbulence.

(A6) C.J. Lau and M.J. Fisher (1975) Journal of Fluid Mechanics 67, Part 2. The vortex street structure of turbulent jets.

(A7) C.J. Lau and M.J. Fisher and H.V. Fuchs (1972) Journal of Sound and Vibration 22, 379-406. The intrinsic structure of turbulent jets.

(A8) C.J. Lau, P.J. Morris and M.J. Fisher (1976) AIAA Paper 76 -348. Turbulence measurements in subsonic and supersonic jets using a laser velocimeter.

(A9) P.O.A.L. Davies, M.J. Fisher and M.J. Barratt (1963) Journal of Fluid Mechanics 15, 337-367. The characteristics of the turbulence in the mixing region of a round jet.

(A10) E. Mollo-Christensen (1967) Journal of Applied Mechanics. Jet noise and shear instablity seen from an experimental view point.

(A11) A.J. Yule (1978) Journal of Fluid Mechanics 89, 413-432. Large scale structure in the mixing layer of a round jet.

(A12) P.E. Dimotakis and G.L. Brown (1975). Large structure dynamics and entrainment in the mixing layer at high Reynolds number.

(A13) H.H. Bruun (1977) Journal of Fluid Mechanics 83, 641-671. A time-domain analysis of the large scale flow structure in a circular jet. Part 1. Moderate Reynolds numbers.

(A14) R.A. Petersen (1978) Journal of Fluid Mechanics 89, 469-495. Influence of wave dispersion on vortex pairing in a jet.

(A15) M.A. Kolpin (1963) Journal of Fluid Mechanics 18, 529-548. The flow in the mixing region of a jet.

(A16) N.W.M. Ko and P.O.A.L. Davies (1971) Journal of Fluid Mechanics 50, 49-78. The near field within the potential core of subsonic cold jets.

(A17) P. Morris and C.W.K. Tam (1971) AIAA Paper 77 -1351. Near and far field noise from large-scale instablities of axisymmetric jets.

(A18) P. Morris (1976) AIAA Paper 76-25. Turbulent measurements in subsonic and supersonic axisymmetric jet in a mixing stream.

(A19) P. Bradshaw, D.H. Ferris and F.R. Johnson (1964) Journal of Fluid Mechanics 19, 591-624. Turbulence in noise producing region of a circular jet.

(A20) J. Seiner (1974) Distribution of jet source strength intensity by mean of a correlation mechanism. PhD thesis, University of Pennsylvania.

(B) Aerodynamic Noise Theory

(B1) M.J. Lighthill (1952) Proc. Roy. Soc.(London),A211, 564-587. On sound generated aerodynamically. 1 - General Theory.

(B2) M.J. Lighthill (1954) Proc. Roy. Soc.(london), A222, 1-32. On sound generated aerodynamically. 2 - Turbulence as a source of sound.

(B3) J.E. Ffowcs Williams (1963) Phil. Trans. Roy. Soc.(London), A255, 469-503. The noise from turbulence convected at high speed.

(B4) G.M. Lilley (1972) United States Air Force Aero Propulsion Laboratory TR-72-53. The generation and radiation of supersonic jet noise; IV - Theory of turbulence generated jet noise,noise radiation from upstream sources and combustion noise.

(B5) D.G. Crighton (1975) Progress in Aerospace Sciences 16, 31-96. Basic principles of aerodynamic noise generation.

(B6) D.G. Crighton (1972) Journal of Fluid Mechanics 56, Part 4. The excess noise field of subsonic jet.

(B7) M.S. Howe (1975) Journal of Fluid Mechanics 71, Part 4. Contribution to the theory of aerodynamic sound with application to excess noise and theory of flute.

(B8) J.E. Ffowcs Williams and M.S. Howes (1975) Journal of Fluid Mechanics 70, Part 3. The generation of sound by density inhomogeneities in low Mach number flow.

(B9) G.M. Lilley AGARD OP-131. Noise mechanism on the noise from jets.

(B10) A. Powell (1964) Journal of Acoustical Society of America 36, pg 177-195. Theory of vortex sound.

(B11) W.C. Meecham Aerodynamic Noise Symposium. A fluid mechanic view of aerodynamic sound theory.

(C) Noise Source and Models

(C1) J. Laufer,R.E. Kaplan and W.T. Chu (1974) AGARD. On the generation of jet noise.

(C2) B.J. Tester and C.L. Morfey (1976) Journal of Sound and Vibration 46, 79-103. Development in jet noise modelling - theretical predictions and comparisons with measured data.

(C3) P.J. Morris (1974) AIAA Paper 74 - 1. A model for the structure of jet turbulence as a source of noise.

(C4) A.P. Dowling,Ffowcs Williams and M.E. Goldstein (1978) Phil. Trans. Soc.(London) A288, 321-349. Sound production in a moving stream.

(C5) J.E. Ffowcs Williams (1978) Journal of Fluid Mechanics 84, 673-694 . The noise from the large scale structure of a jet.

(C6) J.C. Hardin (1973) NASA - TDN - 7242. Analysis of noise produced by an orderly structure of turbulent jets.

(C7) K.A. Bishop,J.E. Ffowcs William and W. Smith (1971) Journal of Fluid Mechanics, 50, 21-23. On the noise sources of unsuppressed high speed jet.

(C8) R. Mani (1973) AGARD CP-131 (Noise Mechanism), 10-12. The issue of convective amplification in jet noise.

(C9) R. Mani (1974) Journal of Fluid Mechanics 64, 611-622. The jet density exponent issue for the noise of heated subsonic jets.

(C10) C.L. Morfey (1973) Journal of Sound and Vibration 31, 391-397. Amplification of aerodynamic noise by convected flow inhomogeneities.

(C11) C.L. Morfey and Szewcyzk (1977) ISVR Technical Report. Jet noise modelling by geometric ccoustics.

(C12) A.J. Kempton (1977) Journal of Fluid Mechanics 83, Part 3, 495-508. Acoustic scattering by density of gradients.

(C13) B. Stuber (1970) Acustica 23, 82. Schallabstrahlung and korpersenhallanregung durch wirbel.

(C14) W. Mohring (1978) Journal of Fluid Mechanics 55, Part 4, 685-691. On vortex sound at low Mach number.

(D) Noise Measurement

(D1) P.A. Lush (1971) Journal of Fluid Mechanics 46, 477-500. Measurements of subsonic jet noise and comparison with theory.

(D2) H.K. Tanna,P.D. Dean and M.J. Fisher (1975) Journal of Sound and Vibration 39, 429-460. The influence of temperature on shock free supersonic jet noise.

(D3) C.J. Moore (1977) Journal of fluid Mechanics 80, Part 2. The role of shear layer instablity waves in jet exhaust noise.

(D4) Lockheed-Georgia Co. AFAPL - tr - 76 - 65. The generation and radiation of supersonic jet exhaust noise.

(D5) H.K. Tanna and P.D. Dean (1975) AIAA Paper 75 - 480. An experimental study of shock free supersonic jet noise.

(D6) R.G. Hoch,J.P. Duponchel,B.J. Cocking and W.D. Bryce (1973) Journal of Sound and Vibration 28,649-668. Studies of the influence of density on jet noise.

(D7) P.A. Lush and M.J. Fisher (1973) AGARD CP - 131 (Noise Mechanism) Noise from hot jets.

(D8) M.J. Fisher,P.A. Lush and M. harper Bourke (1973) Journal of Sound and Vibration 28, 563-585. Jet noise radiation.

(D9) L.W. Lassiter and H.H. Hubbard (1952) NASA - Technical Note 2757. Experimental studiis of noise from subsonic jet in still air.

(D10) G. Banerian (1974) S.A.E. Air Transport Meeting. Jet noise suppression.

(D11) R. Mani (1976) Journal of Fluid Mechanics 73, 779-793. The influence of jet flow on jet noise; Part 2 - The noise of heated jets.

(D12) J.T.C. Liu (1974) Journal of Fluid Mechanics 62, 437-464. Developing large-scale wave-like eddies and the near jet noise field.

(D13) L.O. Merkine and J.C.L. Liu (1975) Journal of Fluid Mechanics 70 353-368. On the development of noise producing large-scale wave-like eddies in a plane turbulent jet.

(D14) C.K.W. Tam (1971) Journal of Fluid Mechanics 46, 757-768. Directional acoustic radiation from a supersonic jet generated by shear layer instabilities.

(D15) C.K.W. Tam (1975) Journal of Sound and Vibration 38, 51-79. Supersonic jet noise generated by large-scale disturbances.

(D16) D.K. Mclaughlin,G.L. Morrison and R.R. Troutt (1975) Journal of Fluid Mechanics Experiment on the instabilities waves in a supersonic jet and their acoustic radiation.

(D17) J.C. Yu and C.K.W. Tam (1978) AIAA Journal Vol. 16, No.10. Experimental investigation of trail edge noise mechanism.

(D18) H.V. Fuchs (1972) Journal of Sound and Vibration 23, 77-99. Space correlation of the fluctuating pressure in subsonic turbulent jets.

(D19) C.A. Kouts and J.C. Yu (1975) AIAA Journal Vol.13, No.8. Far noise field of two dimensional subsonic jet.

(D20) R.R. Armstrong,A. Michalke and H.V. Fuchs (1977) AIAA Journal Vol. 15, No.7. Coherent structures in jet turbulence and noise.

(D21) T.D. Scharton and P.H. White (1972) Journal of Acoustical Society of America Vol.52,No.1. Simple pressure source model of jet noise.

(D22) T.G. Siddon AGARD CP -131. Noise source diagnostics using casuality correlation.

(D23) H.K. Lee and H.S. Ribner Journal of Acoustical Society of America Vol. 52, No.5. Direct correlation of noise and flow of a jet.

(D24) W.C. Meecham and P.M. Hurdle AGARD CP - 131 Use of cross-correlation measurements to investigate noise generation region of a real jet engine and a model jet.

(D25) L. Hoglund and T.C. Siddon (1975) 90th Meeting of the Acoustical Society of America. The effect of probe noise on the cross-correlation in jet noise.

(E) General

(E1) A.S.W. Thomas (1977) PhD Thesis, Adelaide University.

(E2) G. Osborne (1978) Mechanical Engineering Department of the University of Adelaide. Labouratory techniques of hot wire and hot film probe construction and their calibration.

A P P E N D I X

Based on his measurement of entrainment and measurement of convection speed of the large scale structure, Brown (A2) proposed the following simple model to estimate the dependence of the density and velocity ratio on the convection speed of the large structure and the relative entrainment rates.

The mixing layer is modelled as an 'equivalent' temporal problem in which a Galilean transformation $X = U_c t$ is made, where U_c is the average convection velocity of the large structures. That is, the problem is reduced to a consideration of 2 half spaces separated by a plane XOZ with fluids of density ρ_1 above and ρ_2 below. The fluids are set in motion, the upper fluid with velocity u_1 in the positive x direction and the lower fluid with velocity u_2 in the opposite direction. By analogy with the spatial problem, as the vorticity in the initial vortex sheet separating the fluids diffuses and becomes unstable, turbulence develops and large scale structures would be formed (as observed in two-dimensional mixing layer). The velocities u_1 and u_2 can be chosen such that the vortices are on the average not translating (Since $X = U_c t$ where U_c is the convection velocity in the spatial problem). It is postulated in Brown's model

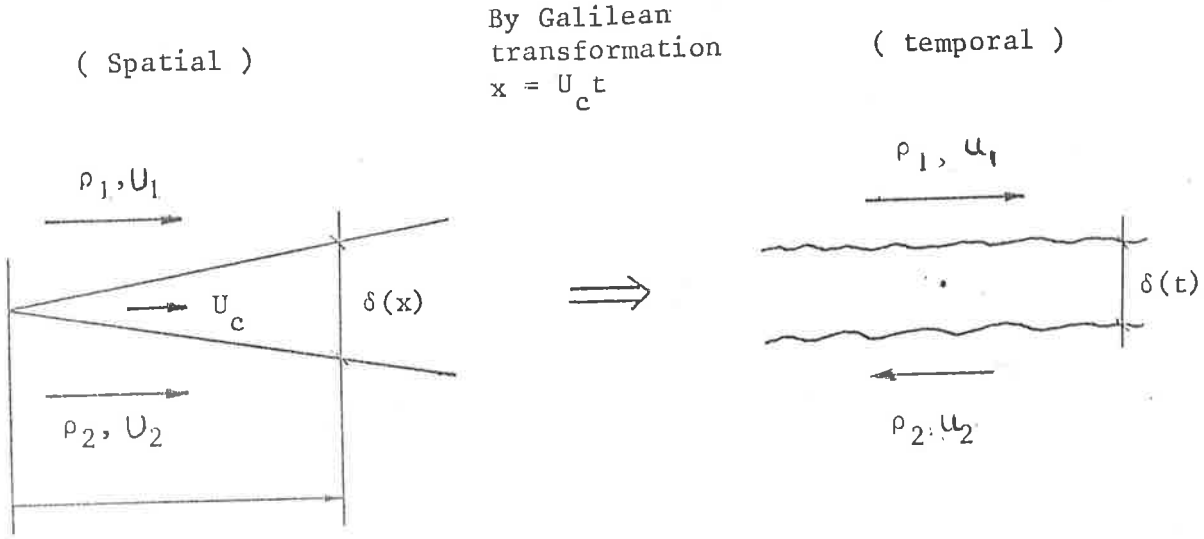

that this will require $u_1 = u_2$ in general but that u_2/u_1 will be a function of ρ_2/ρ_1 i.e. $u_2 = K(s)u_1$, where K(s) is a function of the density ratio $s = \rho_2/\rho_1$. By dimensional analysis for large values of the Reynolds number $\Delta U^2 t/\nu$, the growth rate of the mean thickness of the layer δ must scale only with ΔU i.e. $\delta \propto \Delta U$ (for $t >> \nu/\Delta U^2$) or $\delta = C(s)\ (u_1 + u_2)$ since it is dependent on the density ratio as evident in the experimental results. If an observer now moves with velocity U_c relative to the structures in the negative x direction, the velocities of the fluids relative to the observer are

$$U_1 = U_c + u_1 \quad , \tag{7.1}$$

$$U_2 = U_c - u_2 \quad . \tag{7.2}$$

Using the relationship that $u_2/u_1 = K(s)$ then equation (7.1) and (7.2) become

$$KU_1 = KU_c + Ku_1 \quad , \tag{7.3}$$

$$\text{or} \qquad U_2 = U_c - Ku_1 \quad . \tag{7.4}$$

It follows that

$$(1 + K)\ U_c = U_2 + KU_1$$

$$\text{and} \qquad \frac{U_c}{U_1} = \frac{K + r}{1 + K} \quad , \tag{7.5}$$

where $r = U_2/U_1$ By definition.

Now, the apparent spreading angle $\delta' = \frac{d\delta}{dx}$ he would observe is

$$\delta' = \frac{\dot{\delta}}{U_c} = \frac{C(s)(u_1 + u_2)}{U_c} = \frac{C(s)(U_1 - U_2)}{U_c} = \frac{C(s)(1 - r)U_1}{U_c} .$$

Using equation (7.5), $\delta' = \frac{C(s)(1 + K)(1 - r)}{(K + r)}$. (7.6)

If the same problem is analysed with the same u_1 and u_2 but with ρ_1 and ρ_2 interchanged, it can be shown that C remains unchanged i.e. $C(\frac{1}{s}) = C(s)$ but $K(\frac{1}{s}) = \frac{1}{K(s)}$.

In this model, by dimensional analysis, it follows that the entrainment velocities of the ambient fluids V_{e_1} and V_{e_2} scale with u_1 and u_2 i.e. $V_{e1} = C_1(s)u_1$, $V_{e_2} = C_2(s)u_2$. As a first approximation Brown assumed $C_1(s) = C_2(s)$ so that

$$\frac{V_{e_2}}{V_{e_1}} = \frac{u_2}{u_1} = K(s) , \quad (7.7)$$

for which it follows that the total entrainment

$$V_{e_1} + V_{e_2} = C_1(s)(u_1 + u_2) = C(s)(U_1 - U_2) , \quad (7.8)$$

or $\lambda_1 + \lambda_2 = C_1(s)(1 - r)$

where $\lambda_i = \frac{V_{ei}}{U_1}$.

The assumptions made in arriving at equation (7.7) are supported by the fact that the prediction in equation (7.7) is in direct agreement with conclusion (2) drawn from the entrainment measurement

(see chapter 1 page 3) while equation (7.8) is in agreement with conclusion (1).

In summary, the predictions of the model are that

$$\lambda_1 + \lambda_2 = 0.178\ (1 - r) \quad , \tag{7.9}$$

$$\frac{\lambda_1}{\lambda_2} = \frac{1}{K(s)} \tag{7.10}$$

and $$\delta' = 0.178\ \frac{(1 + K(s))\ (1 - r)}{K(s) + r} \quad . \tag{7.11}$$

By symmetry argument $U_c/U_1 = \frac{K + r}{1 + K}$; Brown deduced that $K(\frac{1}{s}) = \frac{1}{K(s)}$ which is satisfied if $K(s) \propto s^n$ and by comparison with experiment n was found to be approximately - 0.5 (intuitively this gives $U_2/U_1 = (\frac{\rho_1}{\rho_2})^{0.5}$ or $\rho_1 U_1^2 = \rho_2 U_2^2$).

The corresponding predictions of U_c/U_1 , were also found to agree quite closely with the measurements.

It must be pointed out that the constant 0.178 in equation (7.9) and equation (7.11) is obtained from the entrainment measurement. It is however dependent on the definition of the 'edge' of the shear layer which in Brown's measurement is taken at the point where the velocity is less than U_1 by 5% of the velocity difference and greater than U_2 by 5% of this difference.

By mass conservation, the average density in the layer ρ_m is estimated where

$$\rho_m \delta = \rho_1 V_{e_1} + \rho_2 V_{e_2}$$

and using equation (7.8), it becomes

$$\rho_m = \rho_1 \frac{\lambda_1}{(\lambda_1 + \lambda_2)} + \rho_2 \frac{\lambda_2}{(\lambda_1 + \lambda_2)} \quad . \tag{7.12}$$

Following the expression in (7.10), equation (7.12) can be expressed as

$$\frac{\rho_m}{\rho_2} = \frac{1}{1 + K(s)} \frac{1}{s} + \frac{K(s)}{1 + K(s)}$$

$$= \frac{1/s + K(s)}{1 + K(s)} \quad . \tag{7.13}$$